Traveling Wave Parametric Amplifiers and Other Nonlinear Kinetic Inductance Devices

Thesis by
Nikita Sergeevich Klimovich

In Partial Fulfillment of the Requirements for the
Degree of
Doctor of Philosophy

CALIFORNIA INSTITUTE OF TECHNOLOGY
Pasadena, California

2022
Defended May 19, 2022

Nikita Sergeevich Klimovich
ORCID: 0000-0002-5401-8260

ACKNOWLEDGEMENTS

During the past six years, I have been blessed with the opportunity to meet and work with many people that have left a profound impact on this work and my life as a whole. First and foremost, I would like to express my deepest thanks to the research advisors that provided me with the opportunity to work on this research. It would be impossible to list all the ways in which Dr. Peter Day's mentorship and guidance was instrumental to the completion of this thesis. I am deeply grateful for everything you have done to help me throughout my stay at JPL, making my time there a genuinely wonderful experience. My research advisor, Prof. Jonas Zmuidzinas has also been providing the opportunity, freedom, and academic support necessary for this research to take place. I am very thankful for the discussions, impromptu lessons, and encouragement you have given me throughout my time in your group.

I also cannot express enough gratitude to Dr. Byeong Ho Eom whose meticulous laboratory management, extensive training, and daily support and assistance were absolutely invaluable to all of the results presented here. None of the devices presented in this thesis would have been possible without the fabrication efforts of Dr. Henry "Rick" Leduc, who went above and beyond to ensure we had working amplifiers. I would also like to thank Dr. Omid Noroozian and Dr. Sunil Golwala for their encouragement and support throughout the earlier and latter parts of my graduate school journey.

My time at Caltech has also given me the opportunity to work with some amazing postdocs. Dr. Ritoban Basu Thakur has not only been a pleasure to work with but also a phenomenal mentor and role model through his scientific creativity, leadership, and professional support. On top of his enormous contributions to many of the projects described here, I am extremely grateful to Dr. Shibo Shu for helping create an incredibly fun and productive laboratory work environment. While our interactions have been relatively brief, I would like to extend a special thank you to Dr. Karthik Ramanathan for opening my eyes to new possibilities through the dark matter search project.

Aside from my academic colleagues, my graduate school experience was enriched by a wonderful circle of friends who are too numerous to fully credit. I would like to extend an especial thank you to Jane Panangaden for her astounding friendship, constant support, and inspirational activism. Additionally, I am very grateful to

Celeste Labedz, who has been a consistent source of joy throughout our friendship over the past six years. I would also like to thank Arian Jadbabaie for his contagious enthusiasm about physics, who along with Red Lhota and Aaron Markowitz made my time in graduate school a much more fun experience. In addition to the friendships I made in Pasadena, these past few years have been substantially improved by the continued interactions with Mia Miyagi, James Dix, Arthur Lee, and many other friends, particularly during quarantine.

Most importantly, I would like to express my deepest gratitude to my family, David Percer and Elena Klimovich, for their unconditional love, support, and encouragement. My mother especially has had a substantial influence on this academic journey through her parenting and sacrifices which have helped shape my perspectives, attitude, and behavior in every aspect of life. Above all else, I would like to dedicate this thesis to my incredible wife, Inha Cho. I cannot adequately put into words how much our relationship has improved my life. Your presence has been so transformative that I cannot imagine completing this work without your love and support.

ABSTRACT

The microwave frequency range is home to a large amount of cosmologically crucial signals including the cosmic microwave background, emission from high redshift galaxies, and spectral absorption from interstellar dust. In addition to this wealth of scientifically interesting signals, various cutting-edge detector technologies such as microwave kinetic inductance detectors also operate at those frequencies. Both of these areas would greatly benefit from improved readout electronics, which would ideally include broadband, high gain, and low noise amplification. These conditions are generally quite difficult to achieve simultaneously, and have driven the development of a large number of innovative technological solutions. Recently, superconducting traveling wave parametric amplifiers have emerged as a promising candidate for simultaneously meeting the amplification requirements in the microwave regime.

In this thesis, we present further developments of traveling wave parametric amplifiers and other devices based on the nonlinear kinetic inductance of NbTiN transmission lines. The design techniques used for dispersion engineering and impedance matching are very robust, allowing for straightforward alterations to produce amplifiers with bandwidths centered at vastly different frequencies. The majority of our designs focus on the low frequency region from 2 to 12 GHz, where we demonstrate broadband amplifiers with 20 to 30 dB gain, quantum-limited noise, and minimal losses enabling vacuum noise squeezing. The excellent gain and noise performance of one such amplifier is further demonstrated by its use in the readout of a hidden photon dark matter search that sets new limits on the allowable kinetic mixing coupling. One such device was also operated in an up-conversion mode to demonstrate nearly perfect photon conversion efficiency of a narrowband signal near 1.75 GHz to a 12.55 GHz output. At higher frequencies, similar devices are shown to produce gain across over three octaves of bandwidth extending up to 34 GHz and a parametric amplifier operating in the W band. Utilizing the change in phase velocity in our transmission lines with applied current, we build and test a Fourier transform interferometer. We further present a smaller, optimized design that could someday enable the construction of a single-wafer kilopixel array of spectrometers for spatially resolved measurements of the spectral distortions in the cosmic microwave background.

PUBLISHED CONTENT AND CONTRIBUTIONS

[1] Shibo Shu et al. “Nonlinearity and wide-band parametric amplification in a (Nb,Ti)N microstrip transmission line.” In: *Physical Review Research* 3.2 (June 2021). DOI: 10.1103/physrevresearch.3.023184. URL: https://doi.org/10.1103%2Fphysrevresearch.3.023184.

N. Klimovich performed the laboratory measurements, helped analyze the data, and wrote portions of the manuscript.

[2] Ritoban Basu Thakur et al. “Superconducting On-chip Fourier Transform Spectrometer.” In: *Journal of Low Temperature Physics* 200.5-6 (June 2020), pp. 342–352. DOI: 10.1007/s10909-020-02490-7. URL: https://doi.org/10.1007%2Fs10909-020-02490-7.

N. Klimovich participated in the conception of the project, performed the laboratory measurements, helped analyze the data, and wrote portions of the manuscript.

TABLE OF CONTENTS

Chapter 1

INTRODUCTION

1.1 Scientific Motivation

The microwave and sub-millimeter frequency range from 1 to 1000 GHz is home to some of the most significant astronomical signals for our understanding of the universe. Notably, the vast majority of the power in the Cosmic Microwave Background (CMB), the oldest measurable radiation in the universe dating from the epoch of recombination, is contained within this frequency band and is the basis for much of the standard cosmological model.[1]

Understanding the formation of the earliest galaxies shortly after the Big Bang is also crucial for our understanding of the cosmology of the early universe. Spectroscopic observations of the onset of star formation operate at GHz frequencies due to the high cosmological redshift from such distant sources.[2] In addition to these early universe signals, spectroscopic measurements at microwave frequencies are used to shed light on the kinematics of galactic nuclei,[3] the dynamics of star formation,[4] formation of protoplanetary disks,[5] stellar evolution,[6] test strong-field general relativity,[7] and the atmospheric dynamics of Saturn's moons,[8] among countless other astronomical phenomena. Such measurements are often performed using radio interferometers such as the Atacama Large Millimeter/submillimeter Array (ALMA) which allow for detection of such weak astronomical signals by a large collection area coupled with amplification from low-noise cryogenic receivers.

Below 100 GHz, transistor amplifiers are typically used,[9] while above 100 GHz the receivers typically employ a superconductor-insulator-superconductor (SIS) tunnel junction mixer as the first stage. Although SIS receivers in principle can reach the theoretical standard quantum limit for sensitivity,[10, 11] even the most sensitive of these receivers typically operate at noise temperatures over four times above this limit.[12, 13] The same is true for transistor amplifiers. Additionally, the output bandwidth of SIS mixers is limited to around 10-20 GHz.[14, 15, 16] Development of newer technologies with better noise performance and wider instantaneous bandwidths could substantially enhance the scientific productivity of instruments such as ALMA and are a key target for the upcoming decade.[17]

Outside of radio interferometers, the number of pixels in the focal plane arrays for

many single-dish imaging experiments has been steadily increasing over the past few decades.[18] The need for highly sensitive detector technologies that could be easily integrated into such large arrays spurred the creation of microwave kinetic inductance detectors (MKIDs).[19] In the past two decades, the development of MKID technologies has grown exponentially due to their potential for improved measurement sensitivity for a wide variety of frequencies, telescopes, and astronomical targets. [20, 21, 22, 23, 24, 25]

An MKID is a photon measurement technology based on measuring the pair-breaking in superconducting resonators.[26] Photons with an energy above the superconducting bandgap $h\nu > 2\Delta$ are absorbed, resulting in the breaking of Cooper pairs and changing the quasiparticle density. The resulting shift of the kinetic inductance and microwave loss are small, but can be detected by the change in the frequency and quality factor of the resonator.[27] If the energy of the photon is sufficiently large,[28] a single absorption event will result in the breaking of multiple Cooper pairs depending on the energy of the incident photon. Thus, the magnitude of the frequency shift of the resonator can be used to determine the energy of the incident light.[24]

The resolution provided by this spectral response is generally limited not only by the MKID responsivity and two-level-system noise of the resonator's capacitance but also by the amplifier noise in the readout system.[29] While low-noise high-electron-mobility transistor (HEMT) amplifiers are commonly used,[24] the resolution could be further improved by employing amplifiers with near quantum-limited noise,[30] motivating the development of high-gain, low-noise amplifier technology.

The bandwidth of these amplifiers is also crucially important to MKID arrays with a large number of pixels. Hundreds of MKID detectors in a focal plane array could be read out using a single coaxial channel by employing frequency multiplexing for the central frequency of each pixel's resonator.[31] The finite resonator width and fabrication considerations limit the resonator spacing to the order of a MHz,[32] so the bandwidth of the readout amplifiers inversely correlates with the number of channels requires to read out the array.

1.2 Parametric Amplifiers

The equivalent noise temperature of a system of amplifiers connected in cascade with gains $G_1, G_2, ...G_n$ and noise temperatures $T_1, T_2, ...T_n$ is given by the Friis

equation [33]

$$T_{\text{sys}} = T_1 + \frac{T_2}{G_1} + \frac{T_2}{G_1 G_2} + \frac{T_3}{G_1 G_2 G_3} + \ldots + \frac{T_N}{G_1 G_2 G_3 \ldots G_n}. \tag{1.1}$$

For amplifiers with appreciable gain and low noise performance, this noise is dominated by that of the first amplifier in the series, T_1. As a result, the development of increasingly low-noise amplifiers has been at the forefront of enabling new levels of sensitivity in a variety of microwave frequency experiments.

The concept of exploiting the nonlinear reactance of a material to form a parametric amplifier dates back to the early 1900s [34] when it was noted that such a response could be used to transfer power from an applied pump to an incident signal.[35] The early versions of these devices used in radio astronomy were semiconductor-diode based devices,[36] which suffered from fairly limited noise performance.[37] In the 1980s, the invention of Galium arsenide field-effect transistor (GaAs FET) amplifiers [38] and their comparatively excellent noise performance[39] began to replace parametric amplifiers as readout technology.

In parallel to this development, the concept of HEMT amplifiers was introduced in 1979 and resulted in commercially available devices a decade later.[40] By that time, HEMTs routinely outperformed their counterpart cryogenic GaAs FET devices in noise performance.[41] They have subsequently become a dominant choice for first-stage amplification in many experiments due to their excellent gain, large bandwidth, and low noise figures on the order of a few Kelvin.[42] However, because HEMTs are based on inherently dissipative semiconductor materials, their noise level remains significantly above the theoretical quantum limit for added noise.[43]

The continued development of parametric amplifiers would ultimately result in devices operating at this quantum limit[44] but only after many decades of overcoming various practical challenges.[45] Because early parametric amplifiers relied on a single diode as the source of the nonlinearity, they were very narrow-band devices. In the late 1950s, there was a significant resurgence of work on parametric amplification due to the proposal of potentially wide-band traveling wave devices based on the nonlinear reactance of microwave transmission lines.[46] But in the following years, circuit manifestations of this concept met with little success for a number of reasons: due to dispersion it was difficult to achieve the required phase-matching in nonlinear transmission lines based on lumped components such as diodes, while in superconducting transmission lines, the required degree of nonlinearity could not be achieved before the onset of dissipative processes. It was also shown that the

conditions necessary for parametric amplification in a dispersionless traveling wave transmission line, which a uniform superconducting line approximates at frequency well below the gap frequency, would result in the formation of shock waves which will severely limit the amplifier performance.[47] The following years were marked by the first proposal [48] and experimental realization [49] of a superconducting microwave parametric amplifier built using a narrow band resonator. It was quickly noted that similar devices based on the nonlinearity of the Josephson current across a barrier could result in significantly improved performance.[50] This resulted in a large interest in further development of Josephson parametric amplifiers,[51] leading to substantial improvements to their performance and commercialization in the following decades.[52] The band- width of such devices remained fundamentally limited by the circuit scheme which relied on a resonant cavity [53] to provide sufficient interaction length with the nonlinear element.[54]

While wide band microwave parametric amplifiers remained a challenge, progress was made in the area of optics, for example with the development of optical parametric amplifiers based on the Kerr nonlinearity in an optical fiber.[55] Work in that area elucidated the need for phase matching to promote nonlinear processes in traveling wave geometries, and sophisticated phase matching techniques were demonstrated.

In 2012, there was a major breakthrough in the development of microwave traveling wave parametric amplifiers by the use of superconducting materials with high normal state resistivity, such as NbTiN, where it was shown for the first time that the kinetic inductance could provide sufficient reactive nonlinearity little nonlinear dissipation.[56] Shock wave formation was suppressed, and phase matching was promoted, through the use of periodic loading of the transmission line. This thesis presents the subsequent development of these traveling wave parametric amplifiers along with other devices based on the nonlinear kinetic inductance of similar transmission lines.

Improvements in fabrication techniques ultimately allowed for the construction of Josephson-base devices with hundreds or more Josephson junctions in series, enabling the production of broadband traveling wave Josephson parametric amplifiers in 2015.[57] These devices have already demonstrated near quantum-limited sensitivity and are seeing use as readout amplifiers for superconducting qubits, but they appear to be limited in both dynamic range and operating frequency relative to the kinetic inductance based devices discussed here.

Chapter 2

THEORY

2.1 Nonlinear Inductance

An electrical current passing through a cross-sectional area, A, is defined by the number of charges passing through that cross-section per unit time. Expressed in terms of the charge carrier density, n, and the average drift velocity, v_d, the current is given by [58]

$$I = nQAv_d. \tag{2.1}$$

Because the current is comprised of charge carriers with a mass and velocity, there is a kinetic energy associated with their motion. We can use this kinetic energy to define an inductance per unit length, $\mathcal{L}_k$

$$n\left(\frac{1}{2}mv_d^2\right)A = \frac{1}{2}\mathcal{L}_k I^2. \tag{2.2}$$

For resistive materials, this drift velocity will typically be relatively small as the scattering interactions that result in resistance limit the time scale over which the charge carriers might accelerate under the electric field driving the current. The kinetic inductance in these materials can thus frequently be neglected, unless one considers currents with frequencies comparable to the mean scattering frequency.

In superconductors, on the other hand, the drift velocity can be orders of magnitude larger than resistive materials, meaning the kinetic inductance can be quite large.[59] Alternatively, because the scattering frequency for Cooper pairs in a superconductor is zero, the kinetic inductance is an important aspect of the electrodynamic response of a superconductor at any nonzero frequency. This remains true up to the superconducting gap frequency $2\Delta/h$, above which the superconductor behaves a normal ohmic metal. Here, Δ is the superconducting gap parameter, which denotes the energy per electron to break a Cooper pair.

Taking the appropriate mass ($2m_e$) and charge ($2e$) for Cooper pairs, the kinetic inductance per unit length in a superconductor is thus

$$\mathcal{L}_k = \frac{m_e}{2n_s e^2 A}. \tag{2.3}$$

The Cooper pair density, however, is not a constant, but rather a function of temperature, $n_s(T)$, or superconducting coherence length, $n_s(\xi)$. Utilizing the complex

conductivity from Mattis-Bardeen theory, one can calculate the kinetic inductance per unit length of a thin superconducting wire as [60]

$$\mathcal{L}_k = \frac{R_{sq}h}{2w\pi^2\Delta}\tanh^{-1}\frac{\Delta}{2k_BT} \tag{2.4}$$

where R_{sq} is the normal state sheet resistance, Δ is the superconducting gap, and w is the width of the transmission line.

This kinetic inductance has a highly nontrivial relationship on the applied current, as has been demonstrated with mathematical rigor by other sources.[61] For our purposes, it suffices to approximate this current dependence by the Taylor expansion

$$\mathcal{L}(I) \approx \mathcal{L}_0\left(1 + \left(\frac{I}{I_*}\right)^2 + \left(\frac{I}{I'_*}\right)^4 + ...\right) \tag{2.5}$$

where I_*, I'_*, and so on set the scale of the nonlinearity. Note that this series expansion has excluded all odd terms as time reversal symmetry demands they be zero. An alternate derivation using the microscopic theory of nonequilibrium superconductivity [62] shows a similar effect for oscillating radio-frequency currents.

2.2 Coupled Mode Equations

Consider the wave equation for the current in a transmission line with inductance and capacitance per unit length $\mathcal{L}$ and C in one dimension:

$$\frac{\partial^2 I}{\partial z^2} - \frac{\partial}{\partial t}\left[\mathcal{L}C\frac{\partial I}{\partial t}\right] = 0. \tag{2.6}$$

If the inductance and capacitance are independent of the applied current, the solutions to the differential equation will take the form of travelling waves with some amplitude. The full expression for the current can be decomposed into a sum over all frequencies of forward and backward propagating waves with various amplitudes

$$I = \frac{1}{2}\left(\sum_n I_n(z)e^{i(k_nz-\omega_nt)} + I_n^*(z)e^{-i(k_nz-\omega_nt)}\right). \tag{2.7}$$

Under the above assumptions of constant inductance, the amplitudes $I_n(z)$ will be constant, and the oscillations at each frequency form a linearly independent basis for the solutions. However, neither will be the case for a transmission line with a nonlinear inductance per unit length of

$$\mathcal{L}(I) = \mathcal{L}_0\left(1 + \left(\frac{I}{I_*}\right)^2\right) \tag{2.8}$$

as described in the previous section. It is simple to see that the presence of the $I^2(\partial I/\partial t)$ term will result in four-wave frequency mixing of the form $\omega_a = \omega_b + \omega_c + \omega_d$ from its equality to $\partial^2 I/\partial z^2$. Thus, the solutions of the wave equation for the component of $I(z)$ at any particular frequency, $I_n(z)$, will depend on the amplitudes of the waves at all other frequencies.

In the following sections we will derive the coupled mode equations resulting from the wave equation when the only non-zero terms in equation (2.7) are at the pump, signal, idler, and DC frequencies: $\omega_p, \omega_s, \omega_i$, and 0. This approach closely follows the method used by previous works on this topic [56, 63] but is reproduced here to provide additional commentary on the derivation. We will then use this result to justify why the contributions to the signal from other frequencies will be negligible.

Four-Wave-Mixing

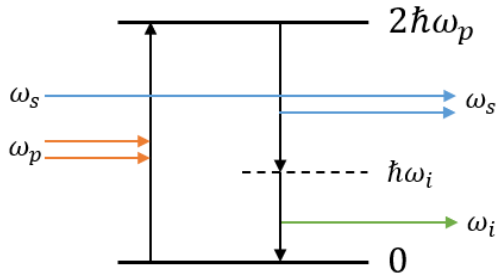

Figure 2.1: The degenerate four-wave-mixing parametric amplification process.

In this section, we are interested in four-wave-mixing processes where two pump photons provide the energy for the stimulated emission of a signal and corresponding idler tone. In particular, we will calculate the resulting gain for the degenerate case where both pump photons share the same frequency, ω_p, as depicted in Figure 2.1.

For conciseness in the following calculation, we define the notation

$$\mu = i(k_\mu z - \omega_\mu t) \tag{2.9}$$

and denote ω_s, ω_i, and ω_p as the signal, idler, and pump wavelengths that obey the energy-conservation relation

$$2\omega_p = \omega_s + \omega_i. \tag{2.10}$$

With these definitions, we can rewrite the expression in equation (2.7) as

$$\begin{aligned} I &= \frac{1}{2}\left(\sum_{n=p,s,i} I_n e^n + I_n^* e^{-n}\right) \\ &= \frac{1}{2}\left(I_p e^p + I_p^* e^{-p} + I_s e^s + I_s^* e^{-s} + I_i e^i + I_i^* e^{-i}\right). \end{aligned} \tag{2.11}$$

We are interested in finding an expression for the change in the amplitudes of each of these components with respect to their position along the transmission line, z. This can be obtained by substituting the above expression into the wave equation and solving

$$\frac{1}{\mathcal{L}_0 C}\frac{\partial^2 I}{\partial z^2} = \frac{\partial^2 I}{\partial t^2} + \frac{1}{I_*^2}\frac{\partial}{\partial t}\left[I^2\frac{\partial I}{\partial t}\right]. \tag{2.12}$$

Consider the left-hand-side of the wave equation above:

$$\begin{aligned} \frac{\partial^2 I}{\partial z^2} &= \frac{1}{2}\frac{\partial}{\partial z}\left(\sum_{n=p,s,i} ik_n I_n e^n + \frac{\partial I_n}{\partial z}e^n - ik_n I_n^* e^{-n} + \frac{\partial I_n^*}{\partial z}e^{-n}\right) \\ &= \frac{1}{2}\sum_{n=p,s,i}\left(-k_n^2 I_n e^n + 2ik_n\frac{\partial I_n}{\partial z}e^n + \frac{\partial^2 I_n}{\partial z^2}e^n\right) \\ &\quad + \frac{1}{2}\sum_{n=p,s,i}\left(-k_n^2 I_n^* e^{-n} - 2ik_n\frac{\partial I_n^*}{\partial z}e^{-n} + \frac{\partial^2 I_n^*}{\partial z^2}e^{-n}\right). \end{aligned} \tag{2.13}$$

In a parametric amplifier, we can reasonably make the slow-varying-amplitude approximation

$$\left|\frac{\partial^2 I_n}{\partial z^2}\right| \ll \left|k_n\frac{\partial I_n}{\partial z}\right| \tag{2.14}$$

that the rate of change in the amplitude is nearly constant over the span of a single wavelength. This leaves only

$$\frac{\partial^2 I}{\partial z^2} = \frac{-k_n^2}{2}\sum_{n=p,s,i}\left(I_n e^n + I_n^* e^{-n}\right) + ik_n\sum_{n=p,s,i}\left(\frac{\partial I_n}{\partial z}e^n - \frac{\partial I_n^*}{\partial z}e^{-n}\right). \tag{2.15}$$

We can then write an equation for $\partial I_n/\partial z$ by setting it equal to all other terms resulting from the wave equation that oscillate with the same frequency given by e^n. We can see one such term in the preceding sum, but let us now consider the expression $I^2(\partial I/\partial t)$.

Calculating

$$\begin{aligned} \frac{\partial I}{\partial t} = \frac{i}{2}\Big(&\omega_p I_p^* e^{-p} + \omega_s I_s^* e^{-s} + \omega_i I_i^* e^{-i} \\ &-\omega_p I_p e^p - \omega_s I_s e^s - \omega_i I_i e^i\Big) \end{aligned} \tag{2.16}$$

and

$$\frac{\partial^2 I}{\partial t^2} = -\frac{1}{2}\left(\omega_p^2 I_p^* e^{-p} + \omega_s^2 I_s^* e^{-s} + \omega_i^2 I_i^* e^{-i} + \omega_p^2 I_p e^{p} + \omega_s^2 I_s e^{s} + \omega_i^2 I_i e^{i}\right) \tag{2.17}$$

and

$$\begin{aligned} I^2 = \frac{1}{4}\Big(& I_p^2 e^{2p} + I_p^{*2} e^{-2p} + I_s^2 e^{2s} + I_s^{*2} e^{-2s} + I_i^2 e^{2i} + I_i^{*2} e^{-2i} \ldots \\ & + 2|I_p|^2 + 2|I_s|^2 + 2|I_i|^2 \ldots \\ & + 2I_p I_s e^{p+s} + 2I_p I_s^* e^{p-s} + 2I_p I_i e^{p+i} + 2I_p I_i^* e^{p-i} \ldots \\ & + 2I_p^* I_s e^{-p+s} + 2I_p^* I_s^* e^{-p-s} + 2I_p^* I_i e^{-p+i} + 2I_p^* I_i^* e^{-p-i} \ldots \\ & + 2I_s I_i e^{s+i} + 2I_s I_i^* e^{s-i} + 2I_s^* I_i e^{-s+i} + 2I_s^* I_i^* e^{-s-i}\Big) \end{aligned} \tag{2.18}$$

shows that $I^2(\partial I/\partial t)$ will produce terms with a number of frequency components.

First, let us consider all the terms that are oscillating at the pump frequency (contain only e^p as the exponent). Multiplying I^2 by $(\partial I/\partial t)$ can only add or subtract one p, s, or j from each exponent, so we only care about terms in I^2 that are one such an operation away from having an e^p term. The only such terms in the above expression for I^2 are

$$\begin{aligned} I^2 = \frac{1}{4}\Big(& 2I_s I_i e^{s+i} + 2I_p^* I_i e^{-p+i} + 2I_p^* I_s e^{-p+s} \\ & + I_p^2 e^{2p} + 2|I_p|^2 + 2|I_s|^2 + 2|I_i|^2 \\ & + 2I_p I_s e^{p+s} + 2I_p I_s^* e^{p-s} + 2I_p I_i e^{p+i} + 2I_p I_i^* e^{p-i}\Big) \end{aligned} \tag{2.19}$$

where the three non-trivial terms result from equation (2.10). Multiplying this by $(\partial I/\partial t)$ and once again keeping only the relevant terms, we obtain

$$\begin{aligned} I^2\frac{\partial I}{\partial t} = \frac{i}{8}\Big[& \left(\omega_p - \omega_s - \omega_i\right) 2I_p^* I_s I_i e^{s+i-p} \\ & + \omega_p\left(|I_p|^2 + 2|I_s|^2 + 2|I_i|^2\right) I_p e^{p}\Big] \end{aligned} \tag{2.20}$$

and once again apply equation (2.10) to obtain

$$I^2\frac{\partial I}{\partial t} = \frac{-i\omega_p}{8}\left[2I_p^* I_s I_i e^{s+i-p} + \left(|I_p|^2 + 2|I_s|^2 + 2|I_i|^2\right) I_p e^{p}\right] \tag{2.21}$$

and

$$\frac{\partial}{\partial t}\left(I^2\frac{\partial I}{\partial t}\right) = \frac{-\omega_p^2}{8}\left[2I_p^* I_s I_i e^{s+i-p} + \left(|I_p|^2 + 2|I_s|^2 + 2|I_i|^2\right) I_p e^{p}\right]. \tag{2.22}$$

Combining (2.22) with the e^p terms of equations (2.15) and (2.17) into (2.12) gives

$$\frac{\partial I_p}{\partial z} = \frac{ik_p}{8I_*^2}\left[2I_p^* I_s I_i e^{s+i-2p} + \left(|I_p|^2 + 2|I_s|^2 + 2|I_i|^2\right) I_p\right] \tag{2.23}$$

using the standard relations

$$\begin{aligned} k_p &= \frac{\omega_p}{v_{\text{ph}}} \\ v_{\text{ph}} &= \frac{1}{\sqrt{\mathcal{L}_0 C}}. \end{aligned} \tag{2.24}$$

Similarly, we can repeat the above procedure for terms with the same time dependence as e^s and e^i to obtain

$$\begin{aligned} \frac{\partial I_p}{\partial z} &= \frac{ik_p}{8I_*^2}\left[2I_p^* I_s I_i e^{s+i-2p} + \left(|I_p|^2 + 2|I_s|^2 + 2|I_i|^2\right) I_p\right] \\ \frac{\partial I_s}{\partial z} &= \frac{ik_s}{8I_*^2}\left[I_p^2 I_i^* e^{2p-i-s} + \left(|I_s|^2 + 2|I_p|^2 + 2|I_i|^2\right) I_s\right] \\ \frac{\partial I_i}{\partial z} &= \frac{ik_i}{8I_*^2}\left[I_p^2 I_s^* e^{2p-i-s} + \left(|I_i|^2 + 2|I_p|^2 + 2|I_i|^2\right) I_i\right]. \end{aligned} \tag{2.25}$$

The quantity e^{s+i-2p} has no time dependence

$$e^{s+i-2p} = e^{i(k_s+k_i-2k_p)z} \tag{2.26}$$

and sets the low-power propagation mismatch

$$\Delta\beta = k_s + k_i - 2k_p. \tag{2.27}$$

The coupled-mode equations above do not have an analytical solution, but they can be solved numerically for co-propagating waves to model the performance of the parametric amplifier in simulations.

While this is the preferred method of calculation in practice, it is insightful to calculate the gains

$$G_s = \frac{|I_s(L)|^2}{|I_s(0)|^2} \qquad \text{and} \qquad G_i = \frac{|I_i(L)|^2}{|I_i(0)|^2} \tag{2.28}$$

under some reasonable assumptions. In the undepleted pump approximation where the pump amplitude is taken to be constant ($I_p(z) = I_p(0)$), we are left with

$$\begin{aligned} \frac{\partial I_p}{\partial z} &= \frac{ik_p|I_p|^2}{8I_*^2}\left[I_p\right] \\ \frac{\partial I_s}{\partial z} &= \frac{ik_s}{8I_*^2}\left[I_p^2 I_i^* e^{-i\Delta\beta z} + \left(|I_s|^2 + 2|I_p|^2 + 2|I_i|^2\right) I_s\right] \\ \frac{\partial I_i}{\partial z} &= \frac{ik_i}{8I_*^2}\left[I_p^2 I_s^* e^{-i\Delta\beta z} + \left(|I_i|^2 + 2|I_p|^2 + 2|I_i|^2\right) I_i\right] \end{aligned} \tag{2.29}$$

where the term

$$\Delta\phi_p = \frac{k_p |I_p|^2}{8 I_*^2} \tag{2.30}$$

is the pump self-phase-modulation. Under the further assumptions that

- we are operating near the center of the gain bandwidth where $\omega_s \approx \omega_i \approx \omega_p$,
- I_s, I_i are small (resulting in no self-phase-modulation),
- the initial conditions of an arbitrary $I_s(0)$ and $I_i(0) = 0$.

these equations have known solutions for the signal power gain, G_s, and idler conversion efficiency, G_i, of

$$\begin{aligned} G_s &= \frac{|I_s(L)|^2}{|I_s(0)|^2} = 1 + \left(\frac{\Delta\phi_p}{g} \sinh gL\right)^2 \\ G_i &= G_s - 1 \end{aligned} \tag{2.31}$$

where

$$g = \sqrt{(\Delta\phi_p)^2 - \left(\frac{\kappa}{2}\right)^2} \tag{2.32}$$

$$\kappa = \Delta\beta + 2\Delta\phi_p \tag{2.33}$$

Because the equations (2.25) are symmetric for the signal and idler, the gain for a signal at any frequency must be identical to the gain of a 'signal' at the corresponding idler frequency. The unity offset between the signal power gain and idler conversion efficiency is simply a restatement of the definition of the four-wave-mixing process. While both the signal and idler amplification contributes to additional signal photons, only the input signal photon (and not idler) contributes to the output power (as can be seen clearly in Figure 2.1).

In the case of no dispersion, $\Delta\beta = 0$ and $g = 0$, the gain scales quadratically with the length of the device and pump power, $|I_p|^2$.

$$\lim_{g \to 0} (G_s) = 1 + \left(\frac{k_p |I_p|^2 L}{8 I_*^2}\right)^2 . \tag{2.34}$$

To maximize the gain, we need to maximize the gain parameter, g, which occurs when $\kappa = 0$ and results in exponential gain.

$$\begin{aligned} G_s(\kappa = 0) &\approx \frac{1}{4} e^{\Delta\phi_p L} \\ G_s &= \frac{1}{4} \exp\left(\frac{k_p |I_p|^2 L}{8 I_*^2}\right). \end{aligned} \tag{2.35}$$

The condition for reaching the optimal exponential gain,

$$\Delta\beta = k_s + k_i - 2k_p = -2\Delta\phi_p = -\frac{k_p|I_p|^2}{4I_*^2} \tag{2.36}$$

occurs when the pump self-phase-modulation perfectly compensates for the dispersion mismatch between the signal, idler, and pump tones. This phase-matching criterion will be investigated in greater detail in the subsequent section.

Three-Wave-Mixing

Another useful operating condition for a parametric amplifier is the three-wave-mixing amplification process where one pump photon provides the energy for the stimulated emission of a signal and idler photon with the energy, as seen in Figure 2.2. The coupled-mode equations governing the gain of a parametric amplifier operated

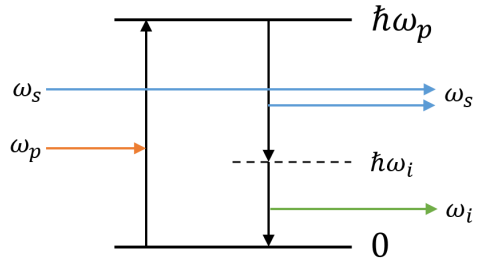

Figure 2.2: The three-wave-mixing parametric amplification process.

in this mode can be derived in a nearly identical manner to the previous section while instead using the energy-conservation equation

$$\omega_p = \omega_s + \omega_i. \tag{2.37}$$

Note, however, that the $I^2(\partial I/\partial t)$ term always results in the mixing of three inputs to produce a fourth output tone, so it is impossible to satisfy the above relation using only the signal, idler, and pump frequencies. Because the inductance is an even function with respect to current, no type of second order nonlinear process (such as second harmonic generation, sum/difference frequency generation, or parametric amplification) can occur. This limitation is analogous to the second order susceptibility being zero for centrosymmetric materials in nonlinear optics, where the polarization will be an even function with respect to the applied electric field.

We can easily break this symmetry in a transmission line by applying a DC current, changing the expression for inductance to

$$\mathcal{L}(I) \approx \mathcal{L}_0 \left(1 + \frac{I^2 + 2I_{DC}I + I_{DC}^2}{I_*^2 + I_{DC}^2}\right) \tag{2.38}$$

where the $2I_{DC}I$ term now allows for the three-wave-mixing amplification process. It is convenient to define

$$I_\dagger^2 = I_*^2 + I_{DC}^2 \tag{2.39}$$

and take the approximation $(I_{DC}/I_\dagger)^2 \ll 1$ giving an inductance

$$\mathcal{L}(I) \approx \mathcal{L}_0 \left(1 + \frac{2I_{DC}I}{I_\dagger^2} + \frac{I^2}{I_\dagger^2}\right). \tag{2.40}$$

We now aim to solve the equation

$$\frac{1}{\mathcal{L}_0 C}\frac{\partial^2 I}{\partial z^2} = \frac{\partial^2 I}{\partial t^2} + \frac{1}{I_\dagger^2}\frac{\partial}{\partial t}\left[(2I_{DC}I + I^2)\frac{\partial I}{\partial t}\right]. \tag{2.41}$$

Following a nearly identical procedure to the previous section, we arrive at

$$\begin{aligned}
\frac{\partial I_p}{\partial z} &= \frac{ik_p}{8I_\dagger^2}\left[2I_{DC}I_s I_i e^{s+i-p} + \left(|I_p|^2 + 2|I_s|^2 + 2|I_i|^2\right) I_p\right] \\
\frac{\partial I_s}{\partial z} &= \frac{ik_s}{8I_\dagger^2}\left[2I_{DC}I_p I_i^* e^{p-i-s} + \left(|I_s|^2 + 2|I_p|^2 + 2|I_i|^2\right) I_s\right] \\
\frac{\partial I_i}{\partial z} &= \frac{ik_i}{8I_\dagger^2}\left[2I_{DC}I_p I_s^* e^{p-i-s} + \left(|I_i|^2 + 2|I_p|^2 + 2|I_i|^2\right) I_i\right]
\end{aligned} \tag{2.42}$$

which ultimately gives us the optimal gain of

$$\begin{aligned}
G_s &= \frac{1}{4}e^{2\Delta\phi_p L} \\
\Delta\phi_p &= \frac{k_p|I_p|^2}{8I_\dagger^2}
\end{aligned} \tag{2.43}$$

when the the optimal phase matching criterion is met.[63]

$$\Delta\beta = k_s + k_i - k_p = -\Delta\phi_p = -\frac{k_p|I_p|^2}{8I_\dagger^2} \tag{2.44}$$

These are nearly identical in form to the four-wave-mixing results in equations (2.35) and (2.36) up to a few constants.

Other Nonlinear Processes

Throughout this chapter, we have derived coupled-mode-equations for both the four-wave-mixing and three-wave-mixing parametric amplification processes while ignoring any other processes that might occur. Mathematically, this was accomplished by only summing over the subset of frequencies composing the RF current

$$I = \frac{1}{2}\left(\sum_n I_n(z)e^{i(k_n z-\omega_n t)} + I_n^*(z)e^{-i(k_n z-\omega_n t)}\right) \tag{2.45}$$

that conform to the energy conservation condition ($2\omega_p = \omega_s+\omega_i$) or ($\omega_p = \omega_s+\omega_i$) for the particular process. Substituting this contracted sum into the wave equation has resulted in three coupled-mode equations that can be solved for the change in amplitudes of the various signals as they travel along the device.

For a more complete model of the parametric amplifier, this sum should be performed over every frequency that could be generated by an energetically allowed combination of signal, pump, and corresponding idler tones ($2\omega_s + \omega_p$, $3\omega_p$, $\omega_p - \omega_i + \omega_s$, etc.) and also for any frequencies that could be formed by iterating this process and arbitrary number of times.

Plugging such a sum of I over N frequencies into the wave equation will result in N coupled-mode equations of the form

$$\frac{\partial I_n}{\partial z} = \text{3WM processes} + \text{4WM processes} \tag{2.46}$$

where [64]

$$\begin{aligned}\text{3WM processes} = \frac{ik_n I_{\text{DC}}}{4I_\dagger^2} &\sum_{\substack{p,q\in\mathbb{N}_0 \\ \sum_j p_j+\sum_j q_j=2}} \frac{e^{ik_n z}}{p_1!...p_m!q_1!...q_m!} \\ &\times \delta\left(\sum_j p_j\omega_j - \sum_j q_j\omega_j - \omega_n\right) \\ &\times \prod_{1\le j\le N}\left(I_j e^{-ik_n z}\right)^{p_j} \prod_{1\le j\le N}\left(I_j^* e^{ik_n z}\right)^{q_j}\end{aligned} \tag{2.47}$$

$$\begin{aligned}\text{4WM processes} = \frac{ik_n}{4I_\dagger^2} &\sum_{\substack{p,q\in\mathbb{N}_0 \\ \sum_j p_j+\sum_j q_j=3}} \frac{e^{ik_n z}}{p_1!...p_m!q_1!...q_m!} \\ &\times \delta\left(\sum_j p_j\omega_j - \sum_j q_j\omega_j - \omega_n\right) \\ &\times \prod_{1\le j\le N}\left(I_j e^{-ik_n z}\right)^{p_j} \prod_{1\le j\le N}\left(I_j^* e^{ik_n z}\right)^{q_j}.\end{aligned} \tag{2.48}$$

The variables p_j and q_j are natural numbers (including zero) counting the number of photons absorbed or emitted at frequency ω_j corresponding to the particular process and the expression inside the Kronecker delta ensures energy conservation for producing an output wave at ω_n. The amplitudes and phases of these waves are multiplied by the two products, given the necessary counting coefficient, and then summed over all combinations of p and q with the proper number of photons for a three or four-wave mixing process.

The set of equations one needs to solve to accurately model the device can be greatly reduced in many applications. Using a parametric amplifier as an example, the pump must have sufficient power in order to provide the energy necessary to simultaneously produce a large amount of gain for all input frequencies, meaning $|I_p| \gg |I_s|$. Since the rate of change in the amplitude of any frequency, $\partial I_n/\partial z$ is proportional to the amplitudes of the waves involved in that process, we can safely ignore any processes that do not include at least one I_p as their effect will be relatively negligible. Other approaches, for instance utilizing Floquet-Block equations,[65] can also be used to perform similar calculations of parametric amplifier performance.

Furthermore, the efficiency of each process will be related to the corresponding phase-matching criterion

$$\Delta\beta = \left(\sum_j p_j k_j - \sum_j q_j k_j - k_n\right) = -\frac{\left(p_p - q_p\right) k_p |I_p|^{|p_p - q_p|}}{8 I_\dagger^2} \tag{2.49}$$

in a similar manner to the previously approximated four-wave-mixing and three-wave-mixing gains. Any process where this phase matching criterion is met will result in exponential growth for the output power I_n, and any process for which $\Delta\beta$ is far from optimal will be equally inefficient.

2.3 Phase Matching

In the previous section, we saw that the gain of a parametric amplifier heavily depends on the dispersion of the pump, signal, and idler tones. Optimal gain is achieved when the dispersion criterion for the process is met, while decreasing to negligible values for signal and idler frequencies with a significant offset from that $\Delta\beta$.

A quantitative calculation of this effect is shown in Figure 2.3 for an arbitrary frequency with varying degrees of dispersion, $\Delta\beta$. As we can see from the plot, the ultimate bandwidth of our parametric amplifier will be determined by the range of frequencies over which the dispersion relation stays close to the optimal value.

For an idealized transmission line with no dispersion, $\Delta\beta = 0$, the parametric amplifier will see some amount of gain. The resulting gain curve for such a device is shown in Figure 2.4 for an arbitrary pump frequency ω_p. Even with such a simple model, we already see a bandwidth outside which the device sees a limited amount of gain.

Unlike the result in Figure 2.3, the bandwidth in Figure 2.4 is determined by the wavenumbers of the signal and idler, k_s and k_i. In the coupled mode equations 2.25, we see that the rate of change of the amplitude of these tones is linearly proportional to this wavenumber, or inversely proportional to the wavelength. We can think of this as setting the length scale for the corresponding signal/idler combinations, which results in different levels of gain when compared to the fixed physical dimension of the device.

A real transmission line will have some degree of natural dispersion. $\Delta\beta$ is a linear combination of the wavenumbers, k_s, k_i, and k_p, which in turn are calculated from the frequency and phase velocity

$$k_\mu = \frac{\omega_\mu}{v_{\text{ph}}}. \tag{2.50}$$

The phase velocity, in turn, is a function of the inductance per unit length.

$$v_{\text{ph}} = \frac{1}{\sqrt{\mathcal{L}C}} \tag{2.51}$$

And, in the case of a superconductor, the surface inductance is a function of the London penetration depth

$$\mathcal{L} = \mu_0 \lambda \coth \frac{t}{\lambda} \tag{2.52}$$

where λ is the penetration depth of the microstrip with thickness t. This penetration depth is given by [66]

$$\lambda = \frac{1}{\sqrt{\mu_0 \omega \sigma_2}} \tag{2.53}$$

where σ_2 is the imaginary part of the complex conductivity $\sigma = \sigma_1 - i\sigma_2$ and can be calculated from Mattis-Bardeen theory by solving

$$\frac{\sigma_2}{\sigma_N} = \frac{1}{\hbar\omega} \int_{\Delta-\hbar\omega}^{\Delta} \left(1 - \frac{2}{e^{(E+\hbar\omega)/kT} + 1}\right) \frac{E^2 + \Delta^2 + E\hbar_\omega}{\sqrt{\Delta^2 - E^2}\sqrt{(E+\hbar\omega)^2 - \Delta^2}} dE \tag{2.54}$$

where σ_N is the bulk normal state resistivity (the sheet resistance times thickness, $\sigma_N = R_s t$).[67] Thus, because λ has a complicated relation on frequency, the

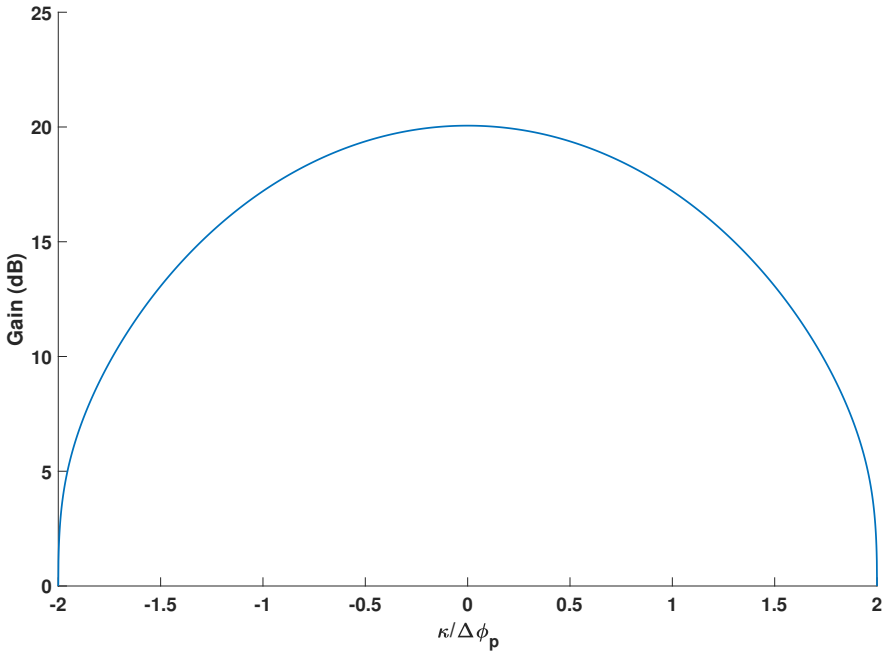

Figure 2.3: A plot of the four-wave-mixing gain with respect to the parameter $\kappa = \Delta\beta + 2\Delta\phi_p$ normalized by $\Delta\phi_p$.

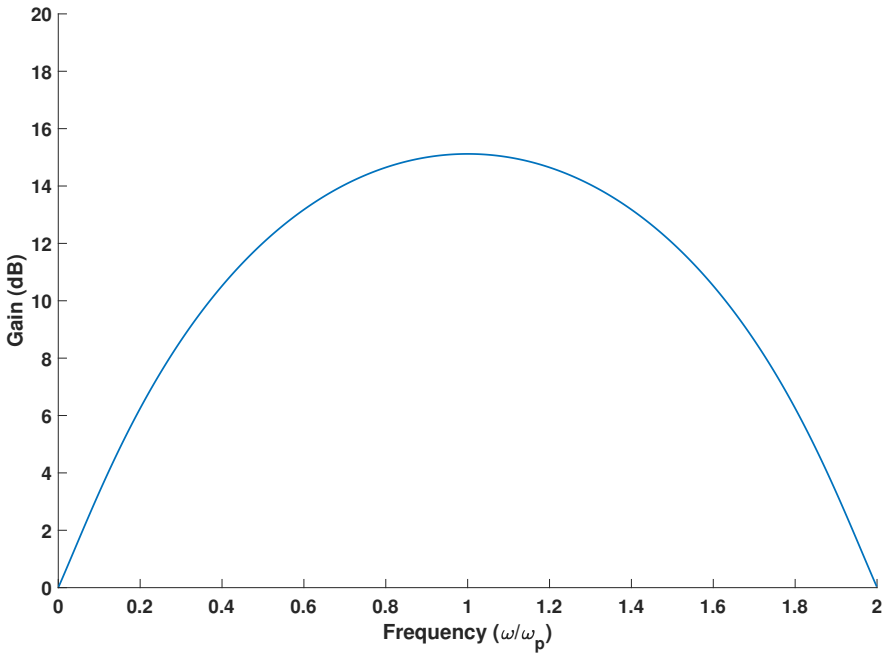

Figure 2.4: Four-wave-mixing gain for an idealized parametric amplifier with $\Delta\beta = 0$ and an arbitrarily chosen pump frequency and power.

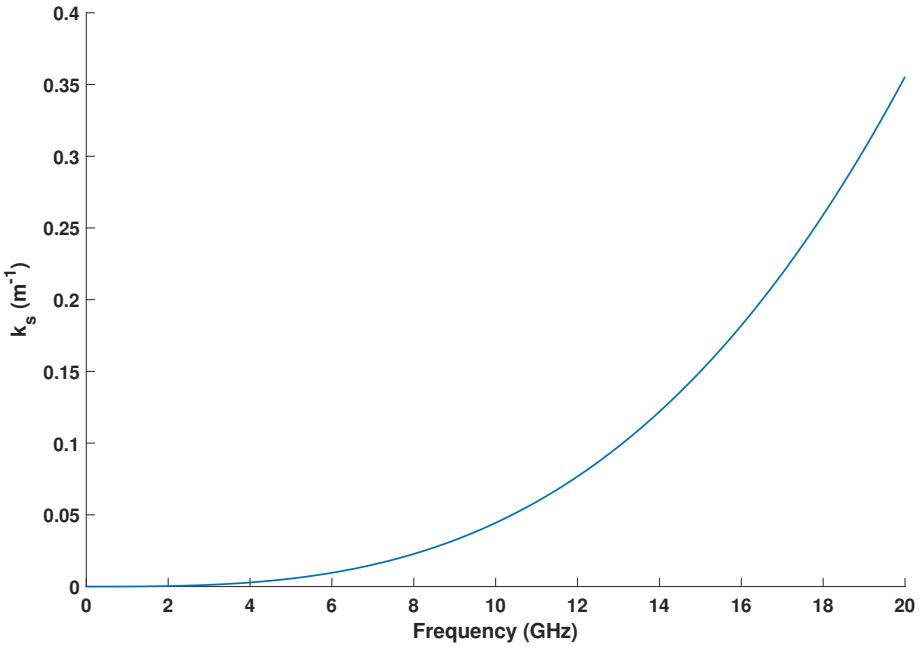

Figure 2.5: The dispersion of a 250 nm by 35 nm NbTiN microstrip with a 400 nm amorphous Silicon dielectric ($\epsilon_r = 11.5$) with the linear component removed.

resulting dispersion curve for the device (and conversely $\Delta\beta$) will likewise have a non-trivial frequency dependence.

In Figure 2.5, we show the nonlinear[1] components of the dispersion curve for a 250 nm wide, 35 nm thick NbTiN microstrip based on the above calculations. We have chosen to plot only the nonlinear component of the dispersion because the linear component will perfectly cancel in the calculation of $\Delta\beta$ due to energy conservation (see equation 2.10). The trend we see mirrors the typical dispersion curve we see in optical materials near visible wavelengths.[68]

Instead of examining the dispersion directly, we could choose a pump frequency and consider how the quantity $\Delta\beta$ will change across frequencies. Doing this for the data in Figure 2.5 and $\omega_p = 2\pi * 10\text{GHz}$ results in the phase matching condition shown in Figure 2.6. The result shows that the phase matching condition due to the inherent dispersion in a microstrip is not ideal for parametric amplification as $\Delta\beta$ ranges from 0 near the pump frequency to a positive value (while the condition for

[1]Note that "nonlinear" here refers to the deviation of k vs ω from a straight line; not to be confused with the previous usage of "nonlinear" with the kinetic inductance variation with applied current.

optimal gain is a negative value as given in equation 2.36).

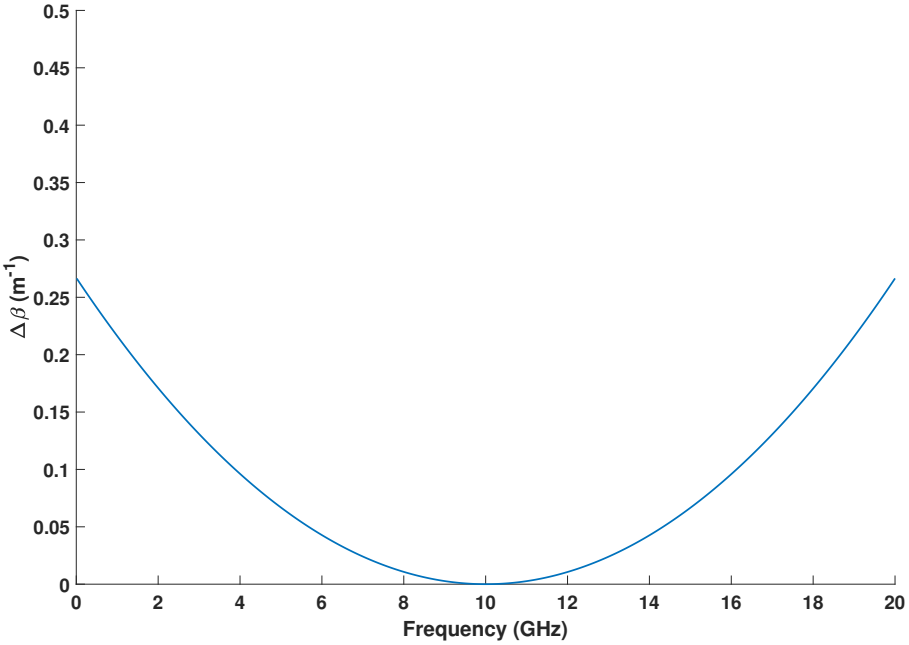

Figure 2.6: The phase matching condition $\Delta\beta$ for a four-wave-mixing process in a transmission line with dispersion as given in Figure 2.5.

We can compensate for these effects by introducing a band gap near the pump frequency through periodically modulating the inductance or capacitance of the transmission line.[69] In our parametric amplifiers, this is done as a two-step process.

First, we introduce long capacitive 'fingers' periodically protruding from the transmission line every $\Delta L = 750$ nm. The primary purpose of these fingers is to obtain 50Ω impedance matching by greatly increasing the capacitance of the transmission line while maintaining the large inductance (see section 3.1 for details). In addition, the periodic modulation creates a photonic band gap at frequency ν_{ebg} [70]

$$\nu_{\mathrm{pbg}} = \frac{v_{\mathrm{ph}}}{2\Delta L}. \tag{2.55}$$

This corresponds to a frequency of slightly above 1 THz in our devices, which is far removed from the operating frequencies of a few GHz. However, each of these capacitive fingers will also act as a quarter-wave resonator, introducing a reflective electronic band gap at

$$\nu_{\mathrm{ebg}} = \frac{4v_{\mathrm{ph}}}{L_f} \tag{2.56}$$

where L_f is the finger length. This parameter is tuned for optimal dispersion (see section 3.2 for further details), but typically results in a band gap at frequencies of a few 100 GHz. Because there are on the order of 10^5 such quarter wave resonators along the transmission line, this results in an enormous effect on the dispersion far below these frequencies.

In Figure 2.7, we see the effect of the dispersion at low frequencies for two capacitive finger lengths corresponding to band gaps near 200 and 400 GHz compared to the unloaded case. It is easy to see that the introduction of these structures introduces a great amount of nonlinear dispersion to the amplifier, the scale of which can be easily controlled by modifying the length of the fingers. For explicit details on this calculation, see section 3.1.

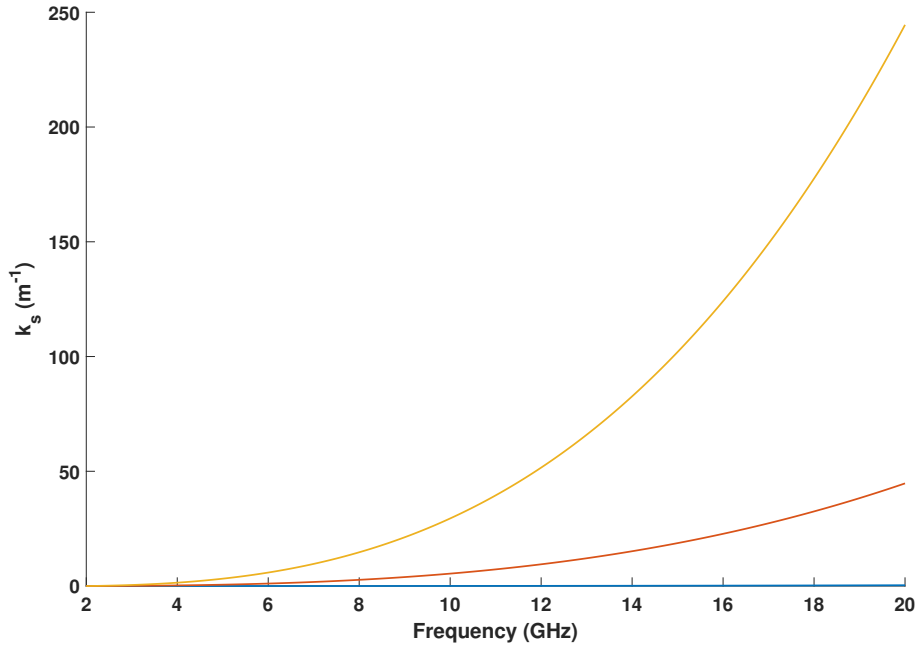

Figure 2.7: The nonlinear components of the dispersion for a 250 nm by 35 nm NbTiN transmission line that is periodically loaded with capacitive fingers of the same material and dimensions. The fingers are spaced on both sides of the transmission line every 750 nm apart, and have lengths of 0μm (blue), 7μm (red), and 14μm (yellow). The blue curve is the limit of no fingers and is identical to that in Figure 2.5.

We can further modify these dispersion curves by applying a second periodic modulation to the length of these capacitive fingers, thereby changing the capacitance. This process will introduce a second band gap according to equation 2.55 that we

will tune to appear near the desired pump frequency. In Figure 2.8, we show the result of introducing such a band gap just above the intended four-wave-mixing pump frequency of 10 GHz. The overall shape of the dispersion curve at frequencies far from the band gap remains roughly unchanged (so k_s and k_i remain largely identical), while the dispersion near it allows us to choose a pump frequency to greatly raise or lower k_p by placing it right beneath or above the band gap.

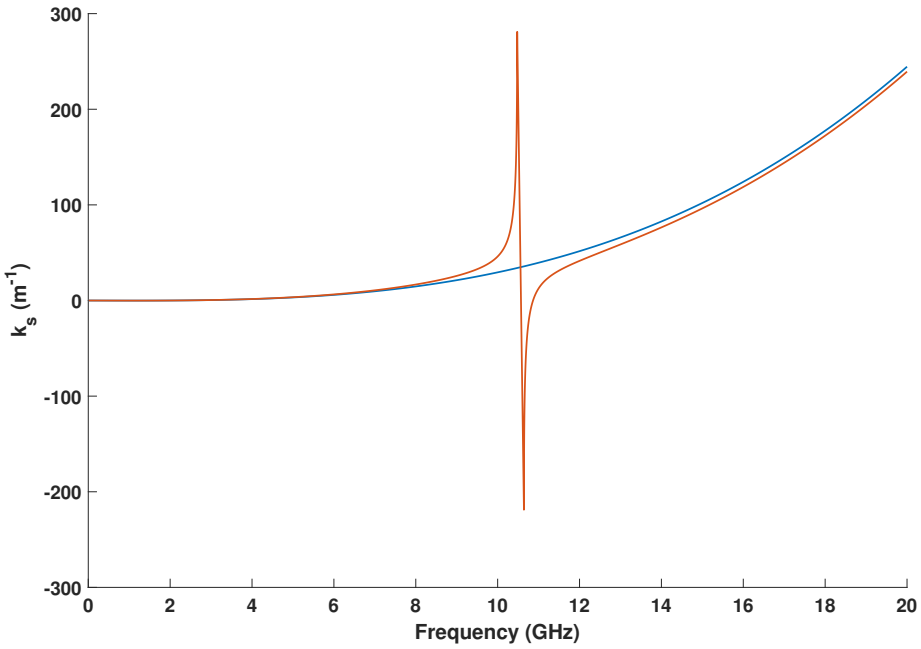

Figure 2.8: The nonlinear components of the dispersion of a superconducting transmission line with (red) and without (blue) a secondary band gap. Both cases correspond to a transmission line with an identical design to the yellow curve in Figure 2.7, where the secondary band gap is produced by modulating the length of the capacitive fingers with a sine wave of 0.45μm amplitude and 97.5nm spatial frequency.

The resulting dispersion criteria for the curve in Figure 2.8 and a 10 GHz pump is shown in Figure 2.9. The introduction of the band gap allows for a range of frequencies to approach the necessary dispersion relation for optimal gain, whereas no frequencies with $\Delta\beta < 0$ existed prior.

The gain curve for these theoretical devices is then calculated by solving the coupled mode equations for the four-wave mixing process derived in the previous section. The results, plotted in Figure 2.10, show a significant overall increase in the maximum gain and bandwidth. This increase comes at the cost of negligible transmission

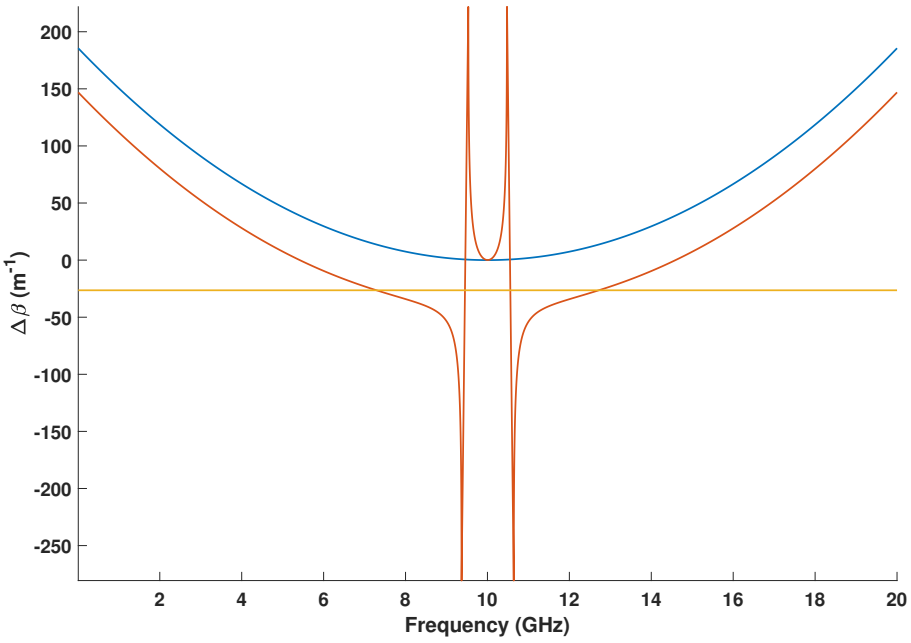

Figure 2.9: The dispersion criterion for a four-wave-mixing process with a 10 GHz pump for the design illustrated in Figure 2.8. The red and blue curves again correspond to the transmission lines with and without the secondary band gap produced by modulating the capacitive fingers. The yellow curve corresponds to an estimate of the optimal phase matching condition based on experimentally measured devices with similar designs.

at the band gap frequency and subsequently minimal gain at the corresponding idler tones due to the symmetries of equations 2.25.

2.4 Quantum Limit for Added Noise

In this section, we will re-derive the quantum mechanical limits on the noise performance of a parametric amplifier. The methodology used in this derivation roughly follows the formalism and methodology used by Carlton Caves in his seminal paper on the topic.[43] This result is crucial enough that we recreate it here with some alterations, applying insights about the particular operation of parametric amplifiers specifically to modify and simplify the calculations. In doing so, we hope to provide commentary that yields more physical insight into the source of the quantum limit and situations where we might expect that limit to be exceeded.

Consider an arbitrary device that takes the bosonic modes of the input photon field, $\mathcal{I}$, and produces an output photon field, $\mathcal{O}$, after some sort of interaction. Each mode

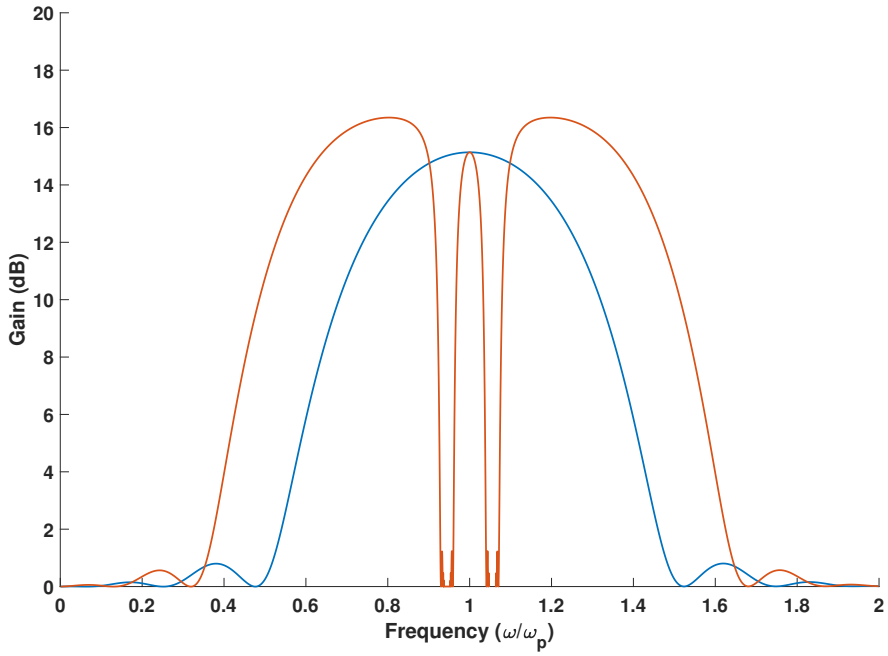

Figure 2.10: The expected gain for the four-wave-mixing process with a 10 GHz pump for the design illustrated in Figure 2.8. The dip in the gain curve just above and below the pump frequency result from the band gap structure.

within this fields has corresponding creation an annihilation operators of $a_\alpha^\dagger, a_\alpha$ for $\mathcal{I}$ and $b_\alpha^\dagger, b_\alpha$ for $\mathcal{O}$ where the subscript α is a label denoting the particular mode with frequency ω_α.

Parametric amplifiers, when operated far below the saturation power, are linear amplifiers in that their gain is independent on signal power. This statement is equivalent to the condition that the operators for the output field are a linear combination of the input field operators [43]

$$b_\alpha = \sum_\beta \left(\mathcal{P}_{\alpha\beta} a_\beta + \mathcal{C}_{\alpha\beta} a_\beta^\dagger \right) + \mathcal{F}_\alpha \tag{2.57}$$

where $\mathcal{P}$, $\mathcal{C}$, and $\mathcal{F}$ are operators containing the internal workings of the amplifier. The operators $\mathcal{F}_\alpha$ determine the amplifiers response independent of the input signal and are thus generally associated with the added noise. The operators $\mathcal{P}$ and $\mathcal{Q}$ contain all the information about the amplifier's response to an input signal, and encode information about the gain. Further assuming that the fluctuations in these operators are minimal during optimal amplifier performance (ie. the pump is in the limit where it is behaving classically), we can redefine these operators in terms of

their expectation values [43]

$$\begin{aligned} \mathcal{P}_{\alpha\beta} &\equiv \langle \mathcal{P}_{\alpha\beta} \rangle \\ \mathcal{P}^*_{\alpha\beta}\mathcal{P}_{\alpha\beta} &= 1 \end{aligned} \tag{2.58}$$

(and similarly for C). This additional assumption ensures that all the internal operators commute with each other and a_β and $a^\dagger_\beta$.

The commutation relation for the output field operators,

$$\left[b_\alpha, b^\dagger_\beta\right] = \delta_{\alpha\beta} \tag{2.59}$$

creates a corollary unitary condition for the amplifier's internal operators

$$\begin{aligned} \left[b_\alpha, b^\dagger_\beta\right] &= b_\alpha b^\dagger_\beta - b^\dagger_\beta b_\alpha \\ \delta_{\alpha\beta} &= \left[\sum_\mu \left(\mathcal{P}_{\alpha\mu}a_\mu + C_{\alpha\mu}a^\dagger_\mu\right) + \mathcal{F}_\alpha\right]\left[\sum_\nu \left(\mathcal{P}^*_{\beta\nu}a^\dagger_\nu + C^*_{\beta\nu}a_\nu\right) + \mathcal{F}^\dagger_\beta\right] \\ &\quad - \left[\sum_\nu \left(\mathcal{P}^*_{\beta\nu}a^\dagger_\nu + C^*_{\beta\nu}a_\nu\right) + \mathcal{F}^\dagger_\beta\right]\left[\sum_\mu \left(\mathcal{P}_{\alpha\mu}a_\mu + C_{\alpha\mu}a^\dagger_\mu\right) + \mathcal{F}_\alpha\right] \end{aligned} \tag{2.60}$$

where we have chosen to preserve the numbering convention for the second two sums without loss of generality. Because $\mathcal{F}$ commutes with $\mathcal{P}$, C, and a, [43] we can simplify the above expression to

$$\begin{aligned} \delta_{\alpha\beta} &= \left[\sum_\mu \left(\mathcal{P}_{\alpha\mu}a_\mu + C_{\alpha\mu}a^\dagger_\mu\right)\right]\left[\sum_\nu \left(\mathcal{P}^*_{\beta\nu}a^\dagger_\nu + C^*_{\beta\nu}a_\nu\right)\right] \\ &\quad - \left[\sum_\nu \left(\mathcal{P}^*_{\beta\nu}a^\dagger_\nu + C^*_{\beta\nu}a_\nu\right)\right]\left[\sum_\mu \left(\mathcal{P}_{\alpha\mu}a_\mu + C_{\alpha\mu}a^\dagger_\mu\right)\right] + \left[\mathcal{F}_\alpha, \mathcal{F}^\dagger_\beta\right]. \end{aligned} \tag{2.61}$$

Combining the rest of the sums, we are left with

$$\begin{aligned} \delta_{\alpha\beta} &= \sum_{\mu,\nu}\left(\mathcal{P}_{\alpha\mu}\mathcal{P}^*_{\beta\nu} - C_{\alpha\mu}C^*_{\beta\nu}\right)\left[a_\mu, a^\dagger_\nu\right] \\ &\quad + \sum_{\mu,\nu}\left(\mathcal{P}_{\alpha\mu}C^*_{\beta\nu} - \mathcal{P}^*_{\beta\nu}C_{\alpha\mu}\right)\left[a_\mu, a_\nu\right] + \left[\mathcal{F}_\alpha, \mathcal{F}^\dagger_\beta\right] \end{aligned} \tag{2.62}$$

which, by the commutation relations $\left[a_\mu, a_\nu\right] = 0$ and $\left[a_\mu, a^\dagger_\nu\right] = \delta_{\mu\nu}$, leaves simply

$$\delta_{\alpha\beta} = \sum_\mu \left(\mathcal{P}_{\alpha\mu}\mathcal{P}^*_{\beta\mu} - C_{\alpha\mu}C^*_{\beta\mu}\right) + \left[\mathcal{F}_\alpha, \mathcal{F}^\dagger_\beta\right]. \tag{2.63}$$

To proceed further, it is helpful to consider the physical meaning of the terms in the above equations. The operators a_α and b_α correspond to some particular frequency

mode (with ω_α or ν_α) of the input and output field. In the ideal case where the only relevant frequency mixing process is the chosen three-wave-mixing or four-wave-mixing gain, only the inputs at the signal (ν_s) and idler (ν_i) frequencies will contribute to the amplifier output signal. As a result, we can transform the sum over $\mu \in \mathcal{I}$ to simply $\mu = s, i$.

For a truly complete model of the amplifier, one should also consider the input at the pump tone (ν_p), in which case the operators $\mathcal{P}$ and C would encode the full range of three-tone interactions one could derive from the wave-equation. In neglecting the pump frequency as we sum over the amplifier inputs, we have effectively defined an operating state for the amplifier where the input and output fields at ν_p have some constant value (I_p), and the operators $\mathcal{P}(I_p)$ and $C(I_p)$ now encode any two-tone interactions for that particular choice of pump. The explicit dependence on I_p is omitted in subsequent calculations, and it is implied that the particular values of $\mathcal{P}$ and C will necessarily change for different amplifier operating conditions. In preserving the linearity of the above relations by taking the input and output pump field to be constant, this definition is corollary to operating the amplifier in the no pump depletion limit.

Considering only the relevant frequencies, the initial expression for the operator corresponding to the output field at the signal frequency

$$\begin{aligned} b_s &= \sum_{\beta=s,i} \left(\mathcal{P}_{s\beta} a_\beta + C_{s\beta} a_\beta^\dagger \right) + \mathcal{F}_s \\ b_s &= \mathcal{P}_{ss} a_s + C_{ss} a_s^\dagger + \mathcal{P}_{si} a_i + C_{si} a_i^\dagger + \mathcal{F}_s \end{aligned} \tag{2.64}$$

or the equivalent

$$b_s^\dagger = \mathcal{P}_{ss}^* a_s^\dagger + C_{ss}^* a_s + \mathcal{P}_{si}^* a_i^\dagger + C_{si}^* a_i + \mathcal{F}_s^\dagger. \tag{2.65}$$

This can be simplified further by considering the amplifier's effect on the phase of the input and output signals. A parametric amplifier is (usually) a phase-insensitive amplifier, meaning the amplifier does not preferentially amplify an input signal based on its phase.

Stated more explicitly, one can decompose the operators for the input and output fields into their real and imaginary parts

$$\begin{aligned} a_s &= I_s + iQ_s \\ a_i &= I_i + iQ_i \\ b_s &= I_b + iQ_b. \end{aligned} \tag{2.66}$$

Note that the transformation

$$\tilde{b} = be^{-i\theta} \tag{2.67}$$

preserves all the commutation relations required in the derivation, so we may freely choose coordinates for the output such that $\mathcal{P}$ and C are both real without loss of generality.[43] Doing so and solving for the operator b in terms of the quadrature inputs of a_s and a_i yields

$$b_s = \mathcal{P}_{ss}\left(I_s + iQ_s\right) + C_{ss}\left(I_s - iQ_s\right) + \mathcal{P}_{si}\left(I_i + iQ_i\right) + C_{si}\left(I_i - iQ_i\right) + \mathcal{F}_s \tag{2.68}$$

or, alternatively

$$\begin{aligned} I_b &= \left(\mathcal{P}_{ss} + C_{ss}\right) I_s + \left(\mathcal{P}_{si} + C_{si}\right) I_i + \mathrm{Re}[\mathcal{F}_s] \\ Q_b &= \left(\mathcal{P}_{ss} - C_{ss}\right) Q_s + \left(\mathcal{P}_{si} - C_{si}\right) Q_i + \mathrm{Im}[\mathcal{F}_s]. \end{aligned} \tag{2.69}$$

The gain for each quadrature is equal to the square of the amplitude of each quadrature, neglecting the zero-input offset $\mathcal{F}$. For an arbitrary input, we can see that the amplifier only equally amplifies both quadratures if and only if both

$$\begin{aligned} \left(\mathcal{P}_{ss} + C_{ss}\right)^2 &= \left(\mathcal{P}_{ss} - C_{ss}\right)^2 \\ \left(\mathcal{P}_{si} + C_{si}\right)^2 &= \left(\mathcal{P}_{si} - C_{si}\right)^2. \end{aligned} \tag{2.70}$$

These conditions can be satisfied by either

$$\begin{aligned} &\left(\mathcal{P}_{ss} = 0\right) \text{ or } \left(C_{ss} = 0\right) \\ &\left(\mathcal{P}_{si} = 0\right) \text{ or } \left(C_{si} = 0\right). \end{aligned} \tag{2.71}$$

The first case, when $\mathcal{P}_{\alpha\beta} = 0$ corresponds to phase-preserving amplification, where a phase shift of ϕ in the input corresponds to a phase shift of ϕ in the output. The second case, when $C_{\alpha\beta} = 0$ corresponds to phase-conjugating amplification, where a phase shift of ϕ in the input corresponds to a phase shift of $-\phi$ in the output.[43]

A parametric amplifier simultaneously undergoes both modes of operation, depending on which frequencies are considered the input and output. When the "signal" of the output is the same frequency as the signal of the input, it operates in the phase-preserving mode. When the "signal" of the output is defined to be the idler tone relative to the input (operating the amplifier also as a frequency translator), the phase relation between the input and output is that of a phase-conjugating amplifier. In other words, for a parametric amplifier, we have

$$\begin{aligned} C_{ss} &= 0 \\ \mathcal{P}_{si} &= 0 \end{aligned} \tag{2.72}$$

meaning

$$b_s = \mathcal{P}_{ss} a_s + C_{si} a_i^\dagger + \mathcal{F}_s. \tag{2.73}$$

Following this argument, the physical intuition of the operators in the above expression is much more apparent. At a chosen signal frequency and operating condition for the pump, $\mathcal{P}_{ss}$ encodes the amplifier's response to inputs of the same frequency, C_{si} encodes the amplifier's response to inputs at the corresponding idler frequency, and $\mathcal{F}_s$ encodes all other processes that produce an excess output independent of the amplifier input (ex. thermal emission from loss and pump phase noise).

An ideal parametric amplifier should not contribute excess noise on its own solely from the operating condition, so in calculating the limits on output noise, we take $\mathcal{F}_s = 0$. In these conditions the expectation value of the output field counting operator, $\langle b_s^\dagger b_s \rangle$, is thus

$$\begin{aligned} \langle b_s^\dagger b_s \rangle &= \langle \left(\mathcal{P}_{ss}^* a_s^\dagger + C_{si}^* a_i \right) \left(\mathcal{P}_{ss} a_s + C_{si} a_i^\dagger \right) \rangle \\ \langle b_s^\dagger b_s \rangle &= \langle \left(|\mathcal{P}_{ss}|^2 a_s^\dagger a_s + |C_{si}|^2 a_i a_i^\dagger + \mathcal{P}_{ss}^* C_{si} a_s^\dagger a_i^\dagger + \mathcal{P}_{ss} C_{si}^* a_i a_s \right) \rangle. \end{aligned} \tag{2.74}$$

Using the canonical relations for creation and annihilation operators,

$$\begin{aligned} \langle a_\alpha^\dagger a_\beta \rangle &= 0 \qquad (\beta \neq \alpha) \\ \langle a_\alpha^\dagger a_\beta^\dagger \rangle &= 0 \end{aligned} \tag{2.75}$$

the expression for $\langle b_s^\dagger b_s \rangle$ readily simplifies to

$$\begin{aligned} \langle b_s^\dagger b_s \rangle &= |\mathcal{P}_{ss}|^2 \langle a_s^\dagger a_s \rangle + |C_{si}|^2 \langle a_i a_i^\dagger \rangle \\ \langle b_s^\dagger b_s \rangle &= |\mathcal{P}_{ss}|^2 \langle a_s^\dagger a_s \rangle + |C_{si}|^2 \left(\langle a_i^\dagger a_i \rangle + 1 \right). \end{aligned} \tag{2.76}$$

Recalling our original criterion for these quantities (2.63), and applying the simplifications derived above (2.72), we obtain the equation

$$\begin{aligned} \delta_{\alpha\beta} &= \sum_\mu \left(\mathcal{P}_{\alpha\mu} \mathcal{P}_{\beta\mu}^* - C_{\alpha\mu} C_{\beta\mu}^* \right) + \left[\mathcal{F}_\alpha, \mathcal{F}_\beta^\dagger \right] \\ 1 &= |\mathcal{P}_{ss}|^2 - |C_{si}|^2 + \left[\mathcal{F}_s, \mathcal{F}_s^\dagger \right] \end{aligned} \tag{2.77}$$

Recognizing these parameters as the signal and idler gains in terms of quanta

$$\begin{aligned} G_s &\equiv |\mathcal{P}_{ss}|^2 \\ G_i &\equiv |C_{si}|^2 \end{aligned} \tag{2.78}$$

yields the striking result

$$G_s - G_i = 1 + \left[\mathcal{F}_s^\dagger, \mathcal{F}_s \right]. \tag{2.79}$$

Thus, if the difference between the signal and idler gains is exactly one, the assumption above of $\mathcal{F} = 0$ is valid and the amplifier can operate in the ideal limit. If it is not unity, then there must be some excess noise injected beyond the quantum limit. At the limit, we can define

$$G_i = G_s - 1 \tag{2.80}$$

for an expected output signal quanta of

$$\begin{aligned} \langle b_s^\dagger b_s \rangle &= G_s \langle a_s^\dagger a_s \rangle + (G_s - 1)\left(\langle a_i^\dagger a_i \rangle + 1\right) \\ n_{\text{out}}(\nu_s) &= G_s n_{\text{in}}(\nu_s) + (G_s - 1)(n_{\text{in}}(\nu_i) + 1). \end{aligned} \tag{2.81}$$

However, the output from the parametric amplifier as measured by an E-field detector will not measure $\langle b_s^\dagger b_s \rangle$ but rather the operator for the output electric field, $(b_s^\dagger + b_S)/\sqrt{2}$. Thus, the output noise we measure will be given by the variance of

$$|\Delta b_s|^2 \equiv \left\langle (b_s - \langle b_s \rangle)^2 \right\rangle \tag{2.82}$$

and the complex conjugate. Solving for this yields

$$\begin{aligned} |\Delta b_s|^2 &\equiv \left\langle \left(\mathcal{P}_{ss} a_s + C_{si} a_i^\dagger - \langle \mathcal{P}_{ss} a_s + C_{si} a_i^\dagger \rangle \right)^2 \right\rangle \\ &= \left\langle \left(\mathcal{P}_{ss}(a_s - \langle a_s \rangle) + C_{si}(a_i^\dagger - \langle a_i^\dagger \rangle) \rangle \right)^2 \right\rangle \\ &= \left\langle \left(\mathcal{P}_{ss} \Delta a_s + C_{si} \Delta a_i^\dagger \right)^2 \right\rangle \\ &= \mathcal{P}_{ss}^2 |\Delta a_s|^2 + C_{si}^2 |\Delta a_i^\dagger|^2 + \mathcal{P}_{ss} C_{si} \langle \Delta a_s \Delta a_i^\dagger \rangle \end{aligned} \tag{2.83}$$

and a similar expression for $|\Delta b_s^\dagger|^2$. It is easy to show that $\langle \Delta a_s \Delta a_i^\dagger \rangle = 0$ by standard commutation rules. Thus, the variance of the output E-field is

$$\frac{1}{2}\left(|\Delta b_s^\dagger|^2 + |\Delta b_s|^2 \right) = |\mathcal{P}_{ss}|^2 \left(\frac{|\Delta a_s^\dagger|^2 + |\Delta a_s|^2}{2} \right) + |C_{si}|^2 \left(\frac{|\Delta a_i^\dagger|^2 + |\Delta a_i|^2}{2} \right). \tag{2.84}$$

The value of these individual variances is well known as the noise temperature expressed in units of quanta,[71]

$$|\Delta a_\mu|^2 = |\Delta a_\mu^\dagger|^2 = \frac{1}{2} \coth\left(\frac{h\nu_\mu}{2kT} \right) \tag{2.85}$$

which obeys the expected relation

$$|\Delta a_\mu|^2 \geq \frac{1}{2} \left| \langle [a_\mu, a_\mu^\dagger] \rangle \right|^2 = \frac{1}{2}. \tag{2.86}$$

Their sums are thus simply the noise in units of quanta at the signal and idler frequencies. Meaning, the output noise simplifies to

$$N_{\text{out}}(s) = G_s N_{\text{in}}(s) + G_i N_{\text{in}}(i). \tag{2.87}$$

We can further separate the output noise into components stemming from the input noise at the measurement frequency ($N_{\text{in}}(s)$) and added noise referred to the amplifier input (A):

$$N_{\text{out}}(s) = G_s(N_{\text{in}}(s) + A). \tag{2.88}$$

Solving for this added noise, and once again using the expression $G_s = G_i + 1$, we obtain the final expression

$$\begin{aligned} A &= \left(1 - \frac{1}{G_s}\right) N_{\text{in}}(i) \\ A &\geq \frac{1}{2}\left(1 - \frac{1}{G_s}\right) \end{aligned} \tag{2.89}$$

in agreement with the well-known half-quantum limit given infinite gain.[43] Note that the physical source of this added noise stems directly from the amplifier input noise at the idler frequencies.[72] The half-quantum limit corresponds to the half-quantum zero-point fluctuations of the input field, and any excess input idler noise will linearly degrade the noise performance of the amplifier.

Note that the total noise at the output in the high-gain limit in equation 2.88 is never smaller than one quantum when referred to the input of the amplifier, corresponding to the statement in equation 2.81. One could argue that the half-quantum from the vacuum is unavoidable (it is the zero-point fluctuation), and that it should not be included in the discussion of the amplifier noise. Yet, if one had an ideal photon detector and did not use an amplifier, so that $G_s = 1$, equation 2.81 would have $n_o ut = n_i n$, i.e., the "+1" from the second term would not enter. In other words, an ideal photon detector is not limited by the zero-point fluctuations.

Chapter 3

DESIGN

Recall from the wave equation 2.6 and the calculation that followed that the nonlinearity in the inductance created the frequency-mixing terms necessary for parametric amplification. For an amplifier with a given physical length, a larger inductance results in a smaller phase velocity, thereby increasing the gain due to the longer effective electrical length. Similarly, the scale of the nonlinearity in the inductance set by the inverse of I_*^2 directly correlates with the spatial derivative of the pump, signal, and idler amplitudes. To maximize the gain of our devices, we must thus naturally look for materials with a large inductance and strong nonlinearity.

In travelling-wave devices, the kinetic inductance of the transmission line is the source of this nonlinearity, meaning the kinetic inductance fraction α (sometimes referred to as the kinetic inductance ratio) should ideally be maximized.

$$\alpha = \frac{L_k}{L_g + L_k} \tag{3.1}$$

This criterion leads naturally to the choice of a microstrip geometry, where α can regularly approach unity for materials with high normal-state resistance, ρ_n, compared with the typically lower values easily obtainable for coplanar waveguide geometries.[29]

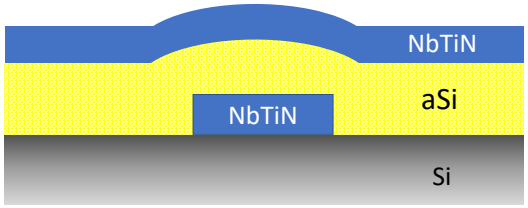

Figure 3.1: The sideways cross-section of our parametric amplifier designs on top of a Silicon substrate. We use an inverted microstrip geometry where the ground plane and dielectric (amorphous Silicon – aSi) are above the central conductor.

The choice of a microstrip geometry is also partially motivated by fabrication and yield considerations. A typical strategy for increasing the capacitance of a coplanar waveguide is to extend interdigitated capacitor fingers, which results in a significantly larger perimeter of the central transmission line near the ground layer. As a result, the

iterations following our original coplanar waveguide design [56] frequently suffered from low yield (occasionally as low as a few percent) due to shorts to ground, particularly for devices with physical lengths of several centimeters. After moving to a microstrip geometry where the ground is separated both by a greater distance and a dielectric, the yield increased substantially with extremely infrequent shorts to ground.

This transition also comes with a cost. Because the ground plane and central conductor are no longer coplanar, an additional layer is needed in the fabrication process. Furthermore, the introduction of a dielectric creates a new avenue of loss through the presence of two-level-system systems.[64] The term two-level systems refers to defects in amorphous solids whose internal motions can lead to dissipation (or loss). The presence of such defects was hypothesized in 1972 in order to explain the low-temperature thermal properties of these materials,[73, 74] and then later connected to a variety of other properties including dielectric loss.[75]

The dielectric loss caused by two-level systems in deposited amorphous thin films used in superconducting circuits was described in 2005 [76] and later found to be relevant even without amorphous films due to a two-level system layer at the surface.[77] In order to minimize these effects,[78] we use an amorphous Silicon dielectric, which introduces a loss tangent that is reliably on the order of 10^{-5}.[79]

The fractional change in the kinetic inductance should be roughly given by the ratio of the energy contained in the inductance

$$E_{\text{ind}} = \frac{1}{2} L_k I^2 \tag{3.2}$$

to the pairing energy of the Cooper pairs

$$E_p = 2N_0 \Delta_0^2 V \tag{3.3}$$

where N_0 is the density of states at the Fermi level, and Δ_0 is the zero-temperature superconducting band gap.[56] The result

$$\frac{\delta L_k}{L_k} = \frac{I^2}{I_*^2} = \kappa_* \frac{L_k I^2}{E_p} \tag{3.4}$$

expressed in terms of fundamental material parameters for a thin film transmission line with width, w, and thickness, t, is [64]

$$I_* = wt\kappa_* \sqrt{\frac{N_0 \Delta^2}{\mu_0 \lambda_L^2}} \tag{3.5}$$

where the scaling factor $\kappa_* = 1.37$ from Usadel Theory.[80][81] It is apparent from the scaling of the above equation that we are particularly interested in materials with large band gaps or, equivalently, high T_c. NbTiN is an excellent choice for both of these parameters, due to it's high normal state resistance and $T_c \approx 14.5$K.

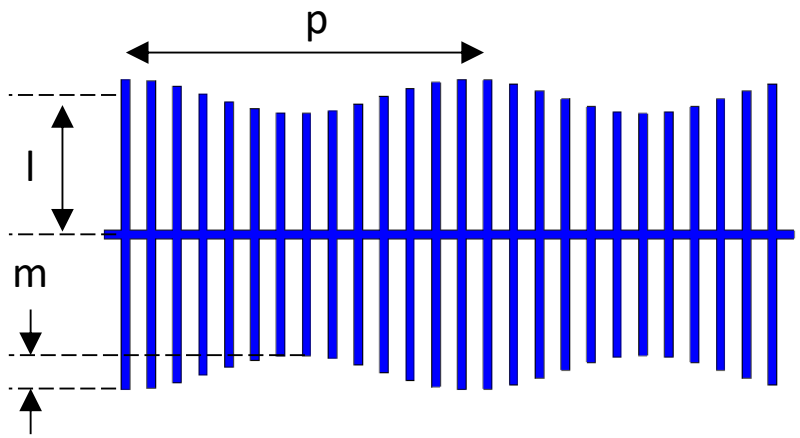

Figure 3.2: A top view of a short section of our microstrip transmission line. Capacitive fingers of average length l are sinusoidally modulated by a wave of amplitude $m/2$ and spatial periodicity p to tune the dispersion.

In maximizing the inductance, it is also necessary to provide a significant amount of capacitance to obtain 50Ω impedance matching ($Z = \sqrt{L/C}$). The dielectric thickness required to do so is too thin to reliably fabricate, so we accomplish this by introducing extra capacitive fingers similar to the interdigitated capacitive fingers of coplanar designs.[63] The length of these capacitive fingers is then further modulated to tune the dispersion of these device (see Figure 3.2). The calculations for determining both of these criteria and calculating the expected gain are presented in the subsequent sections.

Our main focus over the past few years has been towards the development of three-wave-mixing devices, largely motivated by the physical readout systems necessary for post-amplification. The typical pump power we provide for our amplifiers is on the order of -30 dBm, which far exceeds the 1 dB saturation point of most HEMT amplifiers. This power can be removed in one of two methods: injecting a cancellation tone prior to the HEMT that is tuned in amplitude and phase to destructively interfere with the pump [56] or by separating the pump and signal using a diplexer.

In our experience, using a cancellation tone adds significant complications to parametric amplifier operation as any adjustments to the pump amplitude or frequency

(or simply drifts in the system) require sensitive re-tuning of the amplitude and phase of the cancellation tone. Using a diplexer, on the other hand, introduces sizeable reflections through the parametric amplifier at the cross-over frequency between the high-pass and low-pass ports. These reflections can significantly degrade the performance of the parametric amplifier if they occur at frequencies where there is gain, as discussed in more detail in section 4.2. A three-wave-mixing setup is ideal for this as the pump frequency is higher than the entire gain band and is separated by the band gap, creating a convenient location for the diplexer cross-over.

3.1 Impedance Matching

We begin by calculating the impedance of the microstrip line without any capacitive fingers, Z, along with the effective dielectric constant, ϵ_{eff}. We can then calculate the inductance and capacitance per unit length from these quantities via the phase velocity

$$v_{\text{ph}} = \frac{c}{\sqrt{\epsilon_{\text{eff}}}} \tag{3.6}$$

and the standard relations

$$\mathcal{L} = \frac{Z}{v_{\text{ph}}} \qquad\qquad C = \frac{1}{Z v_{\text{ph}}}. \tag{3.7}$$

To a first approximation, we calculate these quantities using the numerical method outlined by Hammerstad and Jensen, whose relevant results are summarized below.[82] Start with an initial estimate of the impedance

$$Z_{01}(u) = \frac{n_0}{2\pi} \ln\left(\frac{f(u)}{u} + \sqrt{1 + \left(\frac{2}{u}\right)^2} \right) \tag{3.8}$$

where n_0 is the wave impedance of the medium, u is the aspect ratio of the microstrip, $u = w/h$ (width normalized by the dielectric thickness), and

$$f(u) = 6 + (2\pi - 6) \exp\left[-\left(\frac{30.666}{u}\right)^{0.7528} \right]. \tag{3.9}$$

The first estimate of the effective dielectric constant is then

$$\begin{aligned} \epsilon_{\text{e}}(u) &= \frac{\epsilon_r + 1}{2} + \frac{\epsilon_r - 1}{2} \left(1 + \frac{10}{u}\right)^{-ab} \\ a &= 1 + \frac{1}{49} \ln\left(\frac{u^4 + (u/52)^2}{u^4 + 0.432} \right) + \frac{1}{18.7} \ln\left(1 + \left(\frac{u}{18.1}\right)^3 \right) \\ b &= 0.564 \left(\frac{\epsilon_r - 0.9}{\epsilon_r + 3} \right)^{0.053}. \end{aligned} \tag{3.10}$$

For microstrips with non-zero thickness, t, it is useful to define modified effective aspect ratios of

$$\begin{aligned} u_1 &= \frac{w}{h} + \frac{t}{\pi h} \ln\left(1 + \frac{4eh}{t \coth^2 \sqrt{6.517u}}\right) \\ u_r &= \frac{w}{h} + \frac{1}{2}\left(1 + \frac{1}{\cosh\sqrt{\epsilon_r - 1}}\right)\left(\frac{w}{h} - u_1\right) \end{aligned} \tag{3.11}$$

which can then be used to modify the above expressions [82][83]

$$Z_0(u) = \frac{Z_{01}(u_r)}{\epsilon_{\mathrm{e}}} \tag{3.12}$$

$$\epsilon_{\mathrm{eff}} = \epsilon_{\mathrm{e}}(u_r)\left(\frac{Z_{01}(u_1)}{Z_{01}(u_r)}\right)^2. \tag{3.13}$$

Because the microstrip transmission is not limited to the purely TEM mode, the effective dielectric constant and impedance will vary with frequency as [82][84]

$$\epsilon_{\mathrm{eff}}(f) = \epsilon_r - \frac{\epsilon_r - \epsilon_{\mathrm{eff}}(0)}{1 + \frac{\pi}{12}\frac{\epsilon_r - 1}{\epsilon_{\mathrm{eff}}(0)}\sqrt{\frac{2\pi Z_0}{n_0}}\frac{f^2}{f_c^2}} \tag{3.14}$$

$$Z(f) = Z_0\sqrt{\frac{\epsilon_{\mathrm{eff}}(0)}{\epsilon_{\mathrm{eff}}(f)}}\left(\frac{\epsilon_{\mathrm{eff}}(f) - 1}{\epsilon_{\mathrm{eff}}(0) - 1}\right) \tag{3.15}$$

where f_c is the first-order approximation of the microstrip cutoff frequency

$$f_c = \frac{Z_0}{2\mu_0 h}. \tag{3.16}$$

Using the relations in (3.6) and (3.7), we then obtain the first estimate of the inductance and capacitance per unit length, $\mathcal{L}_0$ and C_0. The inductance is then adjusted by taking into account the surface inductance of the superconductor

$$\mathcal{L}_{\mathrm{conductor}} = \mu_0 \lambda \coth\frac{t}{\lambda} \tag{3.17}$$

with magnetic penetration depth λ. Applying a DC current or pump will change this inductance in accordance with equation 2.5. Thus, in order to improve impedance matching during the operating condition, one should adjust this value of inductance for the central conductor based on the expected bias and drive level.

The surface inductance of the ground plane is

$$\mathcal{L}_{\mathrm{ground\ plane}} = \mu_0 \lambda_g \coth\frac{t_g}{\lambda_g} \tag{3.18}$$

with thickness t_g and magnetic penetration depth λ_g. These are then combined for the final estimate of inductance

$$\mathcal{L} = \mathcal{L}_0 + \frac{\mathcal{L}_{\text{conductor}}}{w} + \frac{\mathcal{L}_{\text{ground plane}}}{w_{\text{eff}}} \tag{3.19}$$

where w is the width of the microstrip, and w_{eff} is an estimate of the with of the current flow in the ground plan, taken to be the maximum between w and the Pearl Length, which sets the two-dimensional screening length corollary to the one-dimensional London penetration depth.[85]

$$w_{\text{eff}} = \max\left[w, \frac{\lambda_g^2}{t_g}\right]. \tag{3.20}$$

The magnetic penetration depth λ is calculated using [66]

$$\lambda = \frac{1}{\sqrt{\mu_0 \omega \sigma_2}} \tag{3.21}$$

where σ_2 is the imaginary part of the complex conductivity $\sigma = \sigma_1 - i\sigma_2$ and can be calculated from the Mattis-Bardeen theory [67] by evaluating

$$\frac{\sigma_2}{\sigma_N} = \frac{1}{\hbar\omega}\int_{\Delta-\hbar\omega}^{\Delta}\left(1 - \frac{2}{e^{(E+\hbar\omega)/kT}+1}\right)\frac{E^2+\Delta^2+E\hbar_\omega}{\sqrt{\Delta^2-E^2}\sqrt{(E+\hbar\omega)^2-\Delta^2}}dE \tag{3.22}$$

where σ_N is the bulk normal state resistivity (the sheet resistance times thickness, $\sigma_N = R_s t$).

With the inductance, capacitance, and phase velocity of the microstrip without capacitive fingers at hand, it is relatively straightforward to numerically simulate the overall transmission of the device with capacitive fingers included by using the formalism of ABCD matrices. We start by considering a small section of such a device as shown in Figure 3.3. In all of our designs, the width of the capacitive fingers is identical to that of the central microstrip as the two parameters of length and spacing alone give sufficient degrees of freedom for impedance matching and dispersion engineering. The simplest unit cell can be defined by the central microstrip section with length $D_f/2$ leading to the center of each finger, the finger itself, and the remaining $D_f/2$ of the central microstrip to the start of the subsequent cell. Defining

$$\beta = \frac{2\pi\omega}{v_{\text{ph}}}, \tag{3.23}$$

the ABCD matrix for the transmission of a signal for the central transmission line (TRL) portion of the unit cell is [86]

$$\hat{A}_{\text{TRL}} = \begin{bmatrix} \cos\left(\frac{\delta_x D_f}{2}\beta\right) & iZ\sin\left(\frac{\delta_x D_f}{2}\beta\right) \\ \frac{i}{Z}\sin\left(\frac{\delta_x D_f}{2}\beta\right) & \cos\left(\frac{\delta_x D_f}{2}\beta\right) \end{bmatrix}. \tag{3.24}$$

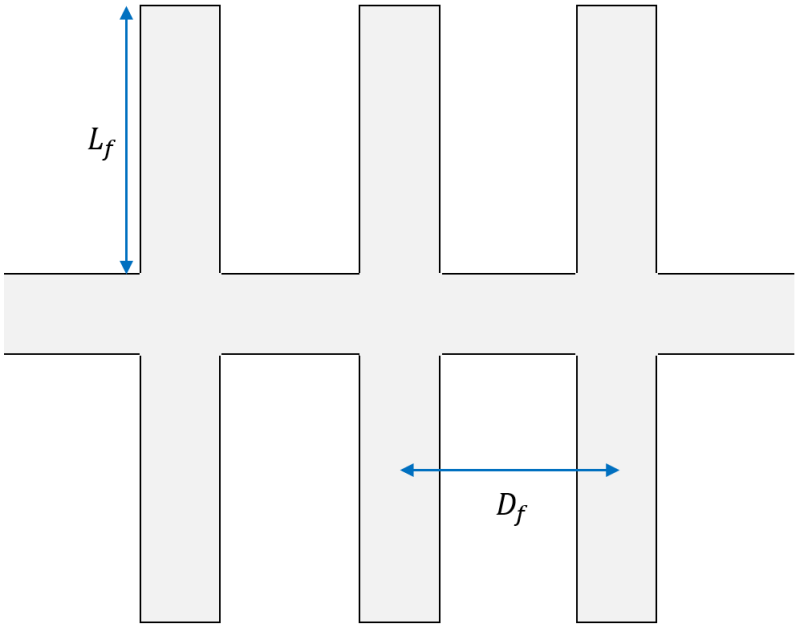

Figure 3.3: Three unit cells of a parametric amplifier with capacitive fingers of length L_f periodically placed along the central microstrip D_f distance apart.

Here, δ_x is an empirically derived fudge factor to compensate for the widening effect of the capacitive fingers on the inductance of the central microstip line calculated above. If the finger spacing is much larger than microstrip width, $D_f \gg w$, then $\delta_x \approx 1$. For our typical designs, where $D_f = 3w$, we find that $\delta_x = 0.8$.

The ABCD matrix corresponding to the effect of the capacitive fingers is [86]

$$\hat{A}_{\text{FIN}} = \begin{bmatrix} 1 & 0 \\ \frac{2i}{Z}\tan(L_f\beta) & 1 \end{bmatrix} \tag{3.25}$$

where the factor of 2 results from having two capacitive fingers. Finally, the combined ABCD matrix for each cell is simply the cascade of these elements.

$$\hat{A}_{\text{CELL}} = \hat{A}_{\text{TRL}}\hat{A}_{\text{FIN}}\hat{A}_{\text{TRL}} \tag{3.26}$$

The ABCD matrix for the amplifier as a whole is similarly the product of the ABCD matrices of each of the N cells comprising the device

$$\hat{A} = \hat{A}_{\text{CELL}}(1)\hat{A}_{\text{CELL}}(2)...\hat{A}_{\text{CELL}}(N-1)\hat{A}_{\text{CELL}}(N) \tag{3.27}$$

where $\hat{A}_{\text{CELL}}(n)$ denotes the ABCD matrix corresponding to the nth unit cell in the device. We can then calculate the propagation constant

$$\gamma = \cosh^{-1}\left(\frac{\hat{A}(1,1) + \hat{A}(2,2)}{2}\right) \tag{3.28}$$

which encodes the change in the complex amplitude of an incident signal at some distance relative to the start of the device.

$$e^{-\gamma x} = \frac{I(x)}{I(0)}. \tag{3.29}$$

Note that because the inductance and capacitance per unit length has frequency dependence, the $\hat{A}$ matrices and γ are also frequency-dependent. Separating $\gamma = \alpha + i\beta$ into its real and imaginary components, we recognize them as the attenuation and phase constants for a propagating wave. Since the inverse cosh function in the complex plane will only return complex values from 0 to π in calculating γ, it is necessary to unwrap β by performing a cumulative sum over successive frequencies

$$k_n = k(\nu(n)) = \frac{1}{D_f}\left(\beta(\nu_0) + \sum_{n=1}^{N} |\beta(n\delta_\nu) - \beta((n-1)\delta_\nu)|\right) \tag{3.30}$$

where the change in β is summed over successive frequency steps in the simulation. We can then extract the resulting phase velocity for the whole transmission line by

$$v_{\text{ph}} = \frac{\omega}{k}. \tag{3.31}$$

The capacitance per unit length is well approximated by the sum of the contributions from the areas spanned by the transmission line and the capacitive fingers.

$$C = C_0\left(\frac{2L_f + D_f}{D_f}\right) \tag{3.32}$$

Note that the geometric effect of joining the capacitive fingers to the main microstrip transmission line will modify the boundary conditions on the fringe fields and thereby nontrivially affect the capacitance. Thus, the above expression loses accuracy when the length to width ratio of the capacitive fingers is on the order of unity.

The final impedance of the device is then simply

$$Z_f = \frac{1}{v_{\text{ph}}C}. \tag{3.33}$$

For a given microstrip material with magnetic penetration depth (λ), width (w), thickness (t), and choice of dielectric (ϵ_r), we can numerically calculate the impedance Z_f for capacitive finger length (L_f), spacing (D_f), and dielectric thickness (h). There is a degeneracy in these results, resulting in infinitely many possible combinations of these parameters to obtain the desired 50 Ω impedance. Of these parameters, the dielectric thickness has the least impact on the dispersion of the device, so it is the parameter that is ultimately tuned for impedance matching (although fabrication limitations may require a minimum L_f for 50Ω impedance to be attainable).

3.2 Dispersion Engineering

This degeneracy of possible designs is somewhat lifted when considering the optimal dispersion. Early in the investigation of the possibility of travelling-wave parametric amplifiers, Landauer discovered that a dispersionless line will result in the formation of shock fronts that would significantly hamper any potential gain.[87] A transmission line with a sinusoidally varying current distribution, $I(z)$, the nonlinearity of the kinetic inductance will create similar variations in the propagation velocity $v_{\mathrm{ph}} = 1/\sqrt{LC}$. In essence, this effect causes the null at $I(z) = 0$ to propagate faster than the peaks at $I(z) = I_{\mathrm{max}}$, resulting in the formation of a shock wave.

An alternative explanation relies on the formation of the third harmonic, with the fifth, seventh, and subsequent harmonics to follow thereafter. The amplitude of these harmonics grows with propagation distance and their coherent combination forms a shock wave that eventually breaks down the superconducting state. One of the key insights that allowed for the creation of the original travelling wave parametric amplifiers was introducing a band gap at the third harmonic frequency, thereby preventing the formation of shock waves and allowing for parametric amplification.[56]

Alternatively, it is possible to accomplish the same effect by introducing significant dispersion to the line to minimize the formation of these harmonics. As shown in section 2.3, the length of the capacitive fingers greatly determines the natural dispersion curve of the device with shorter fingers resulting in a stronger deviation from linear dispersion. Sufficiently short capacitive fingers could move the phase-matching criterion for the particular processes far from the optimum, reducing the efficiently of the process significantly below the dispersionless case studied by Landauer.[87] Unlike the method of using a band gap specifically placed at the desired harmonic,[88] modifying the device dispersion in this way has a greater effect on other parametric processes.

Introducing a strong natural dispersion to the line has the added benefit of suppressing other nonlinear processes occurring at higher frequencies. Any such processes will draw power from the pump and result in some degree of pump depletion if the phase matching condition means they occur with high efficiency.[89] For a three-wave-mixing amplifier, sum frequency generation and four-wave-mixing gain are particularly detrimental to the device performance. Four-wave-mixing gain introduces additional conversion mechanisms to the signal frequency, thereby introducing additional sources of added noise.[63] As shown in section 2.4, the physical source of the added noise in the parametric amplifier is input noise at the idler

frequency. The presence of the four-wave-mixing process couples the signal noise to an a second idler frequency, potentially degrading the device noise performance. Sum frequency generation, on the other hand, upconverts signal photons to $\omega_p + \omega_s$ or $2\omega_p + \omega_s$ (through the three-wave-mixing and four-wave-mixing processes), effectively reducing amplifier gain.

This method of suppressing harmonics comes with a cost. As shown in the previous chapter, exponential gain only occurs when the optimal phase matching criterion

$$\Delta\beta = k_s + k_i - k_p = -\frac{k_p |I_p|^2}{8 I_\dagger^2} \tag{3.34}$$

is met for three-wave-mixing amplification process. We have previously shown that the introduction of a band gap near ω_p can be used to freely modify k_p while only producing a minimal effect on k_s and k_i. If $\Delta\beta$ is tuned to an optimal value for some frequency, it will remain near that value only for frequencies with similar $k_s + k_i$. The trivial way to accomplish this is to minimize dispersion as any nonlinearity will cause this sum to increase relative to the value at ω_p. For $\Delta\beta$ to stay at or near this optimal value across the largest possible bandwidth, $k_s + k_i$ should be close to constant in frequency, implying linear dispersion.

We thus simultaneously want a near dispersionless microstrip below the pump frequency for broadband parametric amplification, strong dispersion above it to suppress other parametric processes, and a tunable dispersion at the pump frequency for optimal phase matching. The methodology for accomplishing this was discussed in detail in section 2.3, while the numerical method for the calculations was laid out in section 3.1.

For devices operating at higher frequencies, it is also possible to introduce multiple band gaps. It is possible to do this by simply modulating the length of the capacitive fingers by the linear combination of two sinusoidal functions with different spatial frequencies, but the effect also naturally occurs in our method, even with a single intended band gap. Although the modulation in the capacitive finger length is sinusoidal, the sinusoid is only spatially sampled at the positions of the fingers, resulting in harmonics. In Figure 3.4, we can see the decaying amplitude of the second, third, and fourth harmonics from the large band gap placed below 50 GHz.

One could in principle use the harmonic of the band gap to tune the dispersion near the pump frequency, corresponding to placing the pump near 95 GHz in Figure 3.4 for four-wave-mixing gain. In this configuration, the large negative curvature from

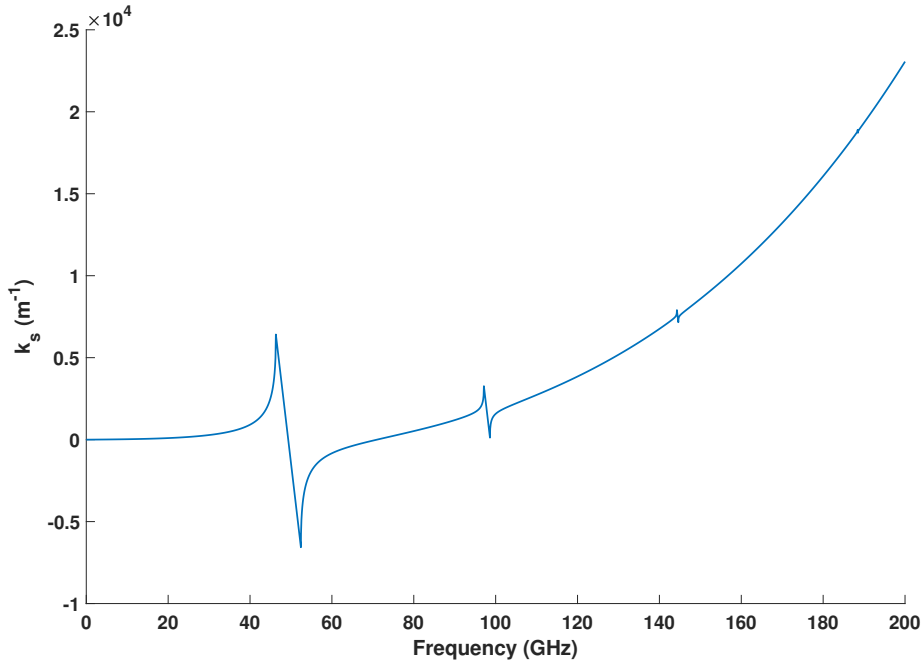

Figure 3.4: The nonlinear component of the dispersion for a 320 by 35 nm NbTiN microstrip transmission line with a 50 nm thick dielectric. The capacitive fingers (same dimensions, spaced 750 nm apart) have an average length of 2.85μm that is periodically modulated by an amplitude of 0.8μm with a period of 15.75μm to introduce a band gap near 49 GHz.

the wide low-frequency band gap beneath the gain band below the pump frequency compensates for the natural dispersion of the idler frequencies above it. In Figure 3.5, one can see that k_s+k_i is much flatter than in the single band gap case particularly at frequencies far away from the pump. With proper tuning, such a method might be used to significantly broaden the gain bandwidth of high frequency parametric amplifiers.

3.3 Gain Optimization

In section 3.1, we calculated $k(\omega)$ in the process of working out the impedance of the microstrip line. With the addition of the calculation of I_* from equation 3.5, we now have everything necessary to solve the coupled mode equations for the expected parametric amplifier gain of our design.

Typically, we will be aiming for gain across a certain bandwidth of frequencies, which in the three-wave-mixing case is centered at $\omega_p/2$, so we will have a fixed pump frequency for the design. Prior to doing the computationally expensive gain

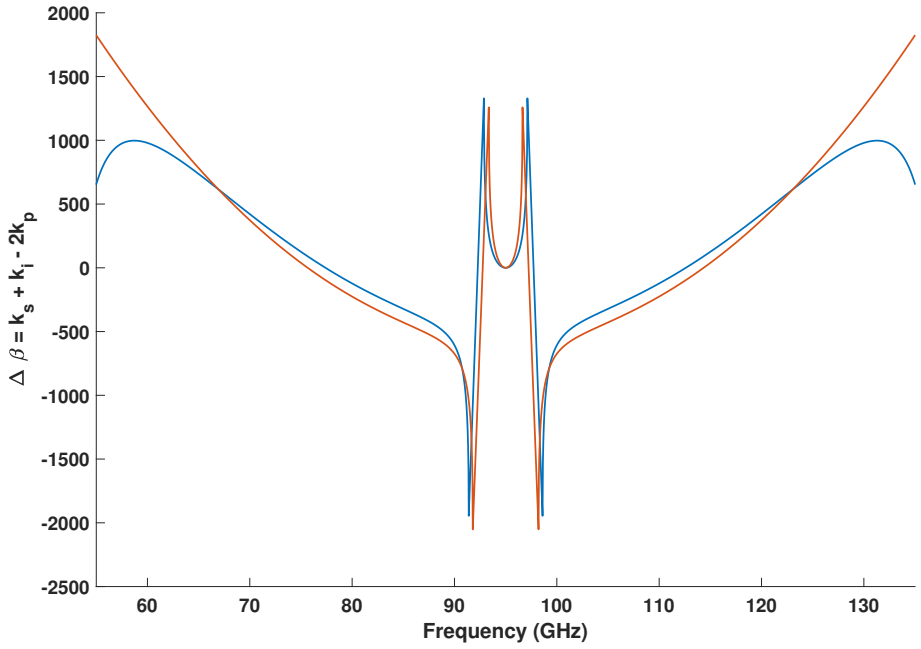

Figure 3.5: The dispersion criterion for a four-wave-mixing parametric amplifier with a 95 GHz pump. The blue curve corresponds to the device in Figure 3.4 while the red curve is an identical design without the large band gap at lower frequencies.

calculation that follows, it is best to tune the free parameters of capacitive finger length, modulation, and modulation amplitude such that $\Delta\beta$ from equation 3.34 is optimized for the center of the gain band. Furthermore, it is worth checking that the phase matching condition for unwanted processes like harmonic generation is $\gg 0$.

One we have an initial design, we choose a set of relevant frequencies, $[\omega_1 ... \omega_n]$, for the parametric processes we wish to consider. Typically, this includes the pump (ω_p), signal (ω_s), three-wave-mixing idler ($\omega_p - \omega_s$), four-wave-mixing idler ($2\omega_p - \omega_s$), sum frequency signal ($\omega_p + \omega_s$), upconverted signal ($2\omega_p + \omega_s$), second pump harmonic ($2\omega_p$), and third pump harmonic ($3\omega_p$). We consider one signal frequency ω_s at a time, and iterate the process across all frequencies ($02\omega_p$) for which we are interested in the gain. Next we define the initial conditions for the amplitudes at frequencies at the input of the parametric amplifier, setting $I_s(0) \ll I_p(0)$ and every other input $I_n(0) = 0$.

The theoretical critical current of the amplifier will be [80]

$$I_c = 0.75wt\Delta_0^{3/2}\sqrt{\frac{N_0\sigma}{\hbar}} \tag{3.35}$$

which sets the maximum limit of the initial condition for $I_p(0)$ and $I_{\mathrm{DC}}(0)$. In practice, the critical current is unlikely to reach this idealized limit (see section 4.1 for details), so it is best to limit both to half of this value or base it on experimental results from similar designs.

Taking these initial conditions, we then calculate the amplitudes of each of the frequencies, $\mathcal{W} = [\omega_1 ... \omega_n]$, as they propagate through the device. First, we extend the set of frequencies to their negative counterparts: $\mathcal{W}' = [-\omega_n, -\omega_{n-1}, ... -\omega_1, \omega_1 ... \omega_n]$, then we consider each possible combination $\omega_\Sigma = \omega_a + \omega_b + \omega_c$ with $\omega_{a,b,c} \in \mathcal{W}'$ such that the resulting $\omega_\Sigma \in \mathcal{W}$. For all such combinations, we calculate the spatial derivative contribution to I_Σ according to equations 2.46. This process necessitates that we calculate one signal frequency at a time, or the resulting coupled-mode equations would include all parametric mixing processes between the calculated signal frequencies, which would be computationally infeasible to solve.

Starting from the initial conditions, we iterate this process across some small δL, feeding the output amplitudes into each subsequent section to solve the coupled mode equations for the amplitudes at the output of the amplifier. The above calculation is then repeated for each signal frequency of interest.

Once the calculation is complete, we check the amplitudes of the undesirable parametric processes as a function of position along the device to ensure that they never consume much pump power. An example of such a calculation in Figure 3.6. Note that the power for these poorly-matched processes will oscillate between the pump and other participating frequencies.[89] In this example, the pump amplitude is frequently reduced by five percent due to second harmonic generation, indicating that additional dispersion is needed to mismatch that process.

Optimizing the gain is a highly iterative procedure involving generating a device geometry, solving for its dispersion curve, then calculating the efficiencies of the various parametric processes. Once we have obtained the result, we modify the original design as needed: by increasing/reducing the dispersion through changing the lengths of the capacitive fingers, modifying the amplitude/frequency of the sinusoidal variations to their lengths that generate band gap(s) for phase matching, and make corresponding changes to the dielectric thickness to maintain the desired impedance.

While this process is crucial for designing a potentially working amplifier, it is difficult to obtain accurate predictions for the amplitude of the resulting gain prior

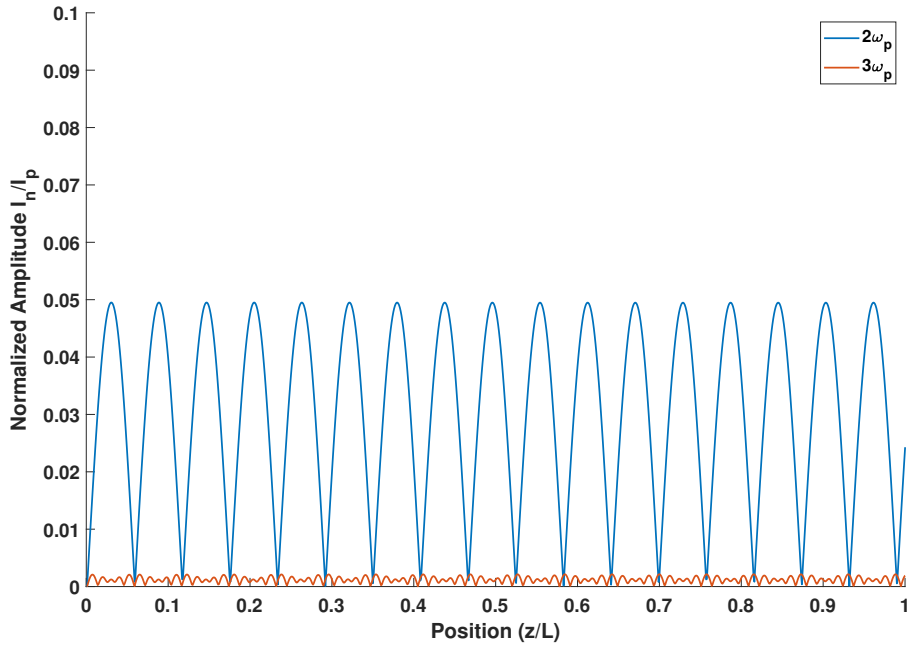

Figure 3.6: The second and third harmonic amplitudes normalized by the initial pump amplitude $I_p(0)$ plotted from the start to end of a model microstrip transmission line.

to laboratory testing due to the difficulty of accurately various device parameters, particularly the critical current. Guided by experimental measurements, however, the procedure outlined in this chapter can reliably reproduce laboratory result and inform better estimates of fabrication-dependent material properties.

Chapter 4

LOW FREQUENCY PARAMETRIC AMPLIFIERS

4.1 DC Screening

Our parametric amplifiers are typically fabricated on four-inch crystalline SOI wafers. Each device has a physical footprint of roughly 250 x 25 mm, resulting in three full columns of chips with 36 fully formed devices in the central row and an additional 20 on each side. Because the process of mounting and testing individual amplifiers is quite time consuming, it is more effective to perform a simple DC screening to identify which of the 76 amplifiers on each wafer is most promising for further investigation. The screening procedure is outlined below.

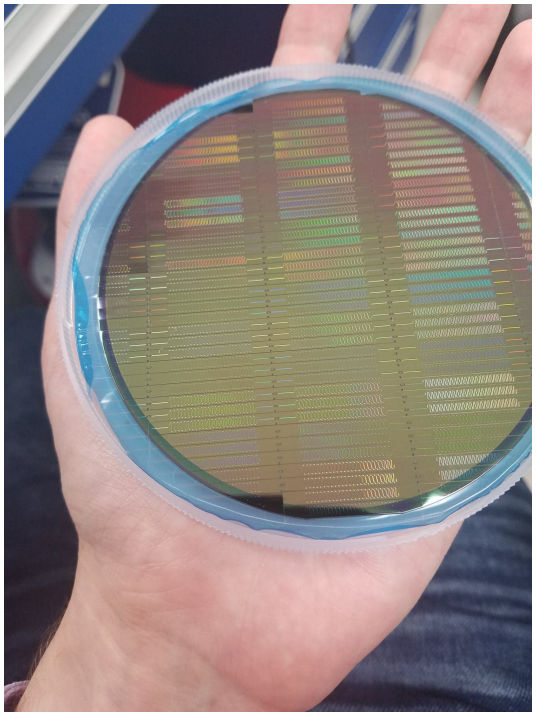

Figure 4.1: A four-inch wafer containing six different parametric amplifier designs.

1. Using a pair of tweezers, gently remove 12 devices from the wafer.

Because there will typically be some small level of non-uniformity of layer thicknesses across the wafer, it is typically best to start with the devices nearest to the center as those are the most likely to be closest to the designed parameters. However,

imperfect calibrations during fabrication or mistakes during the design may mean that the desired NbTiN or amorphous Si thickness is obtained somewhere along the gradient. As a result, it can be useful to record the location of the samples taken so that one can preferentially select devices nearest those with the best performance.

2. Remove the protective layer of photoresist.

Firmly holding each device over a beaker, spray the top surface of the amplifier with acetone for several seconds. The acetone dissolves the photoresist but leaves behind a residue, to prevent this, continue by cleaning the surface in a similar manner using isopropyl alcohol. Then, while maintaining a strong grip on the device, blow away the remaining liquid using a can of compressed nitrogen gas. During this last step, it is important to direct the airflow parallel to the surface of the amplifier so that the liquid runs off of the device rather than normal to the surface. Failure to do so allows the remaining liquid to evaporate while on the surface, leaving behind a residue which will make the subsequent steps of wire bonding the sample much more difficult.

3. Attach the devices to a DC screening probe using a small amount of GE Varnish.

The probe is a simple setup consisting of a tube that can be lowered into a container of liquid Helium, a box containing 26 BNC connectors at room temperature, and a copper sample-stage with 24 individual bonding pads with soldered wires leading up to the connectors. Because these devices will need to be non-destructively detached from the sample plate after screening, it is best to only use a bare minimum amount of varnish and slightly under-cure it so that the devices are held firmly in place but will budge under any non-negligible amount of pressure.

4. Wire bond the device inputs, outputs, and ground.

Because this step will only check the amplifier performance at DC, it is unimportant to make short wire bonds or an excellent connection of the Nb sky plane on top of the devices to ground. Two wire bonds to each input/output for redundancy is ideal, and six to ten spread out connections of the device ground plane to the copper box is sufficient.

5. Dip the devices into liquid Helium and measure I_c at 4K. The measurement setup for determining I_c is shown in Fig. 4.3. Prior to measuring I_c, disconnect the connection to ground after the amplifier (leaving it open) and increase V_s to a small non-zero value. Since there is now an open circuit, the probe should measure a voltage difference of $V_d = V_s$ to ground. If any other value is measured, there is

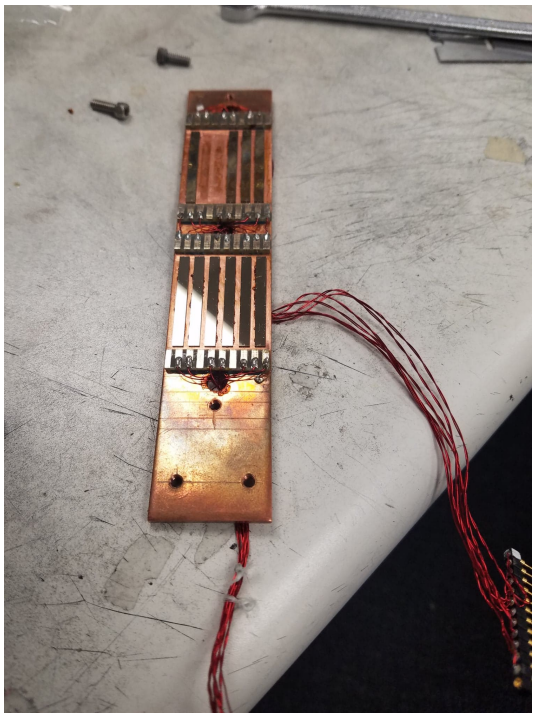

Figure 4.2: The DC screening probe with twelve devices mounted, two of which were removed for further testing.

an unintended connection to ground through the dielectic. It is not uncommon to see devices with an internal resistance to ground of a few kΩ or higher, and there is seemingly no adverse affect on the RF performance of the device. Shorts to ground (and other, smaller internal resistances through the amorphous Silicon) introduce significant reflections in the device and can greatly degrade device performance.

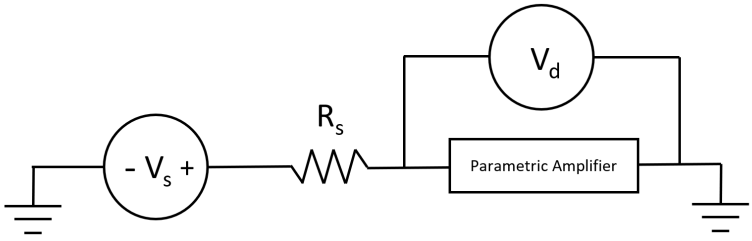

Figure 4.3: Schematic diagram of the measurement setup for the I_c screening. The parametric amplifier is connected to a voltage source, V_s, with a series resistor, R_s, and grounded on the other side. A voltage meter tracks the voltage drop, V_d, across the device.

Our amplifiers typically have an $I_c \approx 1$ mA, but can reach several mA depending on

the design. For a standard 5V power supply, the series resistance must be sufficiently low in order to supply this level current, meaning

$$R_s < \frac{V_{\max}}{I_c} = 5\ \text{k}\Omega. \tag{4.1}$$

However, special care must be taken for choosing an R_s based on the device design. The NbTiN films in our devices have a sheet inductance of 4.2 pH/sq. Our parametric amplifiers' conductive section is typically 250 nm wide and on the order of 10 cm long, corresponding to a total kinetic inductance of 1.7 μH. Converting this to normal state resistance of our devices:

$$R_n = \frac{\pi \Delta L_k}{\hbar} = 6.3\ \text{M}\Omega. \tag{4.2}$$

At room temperature, the normal state resistance will be on the order of a few kΩ as the primary path of conduction through the device will be not through the NbTiN, but rather through the silicon layer out to the ground of the device housing, then back through the silicon and into the output. At normal operating temperatures (4 K and below), the conductivity of semiconductors exponentially vanishes, and the Silicon dielectric contribution to the overall device resistance becomes negligible, making the above value an accurate approximation of the resistance once the device goes normal.

Because $R_n \gg R_s$, when the applied current exceeds I_c and the device goes normal, nearly all the voltage drop will occur across the amplifier. This poses a potential problem since the breakdown field of Silicon is roughly $3 * 10^5$ V/cm. When the device is driven normal, there will be a a voltage gradient between the NbTiN and the ground plane above it. The typical dielectric thickness of the amorphous Silicon in our devices is on the scale of 50-200 nm (here assumed to be 100 nm for an order of magnitude estimation), so the breakdown electric field is reached when

$$V_{\text{breakdown}} = 3 * 10^5\ \text{V/cm} * 100\ \text{nm} = 3\ \text{V}. \tag{4.3}$$

If this breakdown voltage is exceeded, an electrical discharge may occur between the microstrip conductor and the ground plane, permanently damaging the dielectric. This typically results in the formation of a new conduction path, creating a short to ground at the site and irreparably degrading the amplifier performance. As a result, it is crucial to use a low R_s when applying a DC bias to the device to limit the potential voltage drop across it, particularly for designs with very thin dielectric layers.

Once appropriate care has been made to ensure the breakdown voltage will not be exceeded, one can begin to screen the devices. The current flowing through the amplifier is simply

$$I = \frac{V_s}{R_s + R_{pa}} \tag{4.4}$$

and the internal resistance of the parametric amplifier, R_{pa}, can be calculated from

$$\begin{aligned} \frac{V_d}{R_{pa}} &= \frac{V_s}{R_s + R_{pa}} \\ R_{pa} &= \frac{V_d R_s}{V_s - V_d}. \end{aligned} \tag{4.5}$$

To measure I_c, slowly increase the supply voltage, V_s, while monitoring the voltage drop across the device, V_d. While the device is in the superconducting state, because $R_{pa} = 0$, V_d will stay at exactly 0. Once the critical current is exceeded and superconductivity breakdown, R_{pa} (and therefore V_d) will increase substantially.

As superconductivity break down by exceeding I_c, the internal R_{pa} will not immediately increase to the normal state resistance of a few MΩs for two reasons. First, imperfections in the NbTiN layer create weak spots with locally lower I_c compared to the bulk of the microstrip. Once this critical current is reached, only that small region of the device is driven normal while the rest of the microstrip remains in the superconducting state. Second, the increase in amplifier resistance from these weak spots creates a negative feedback loop for the applied current. As R_{pa} increases, the current drawn from the power supply decreases due to the higher series resistance, effectively creating a self-limiting effect.

In Figure 4.4 we show the typical result of such a screening for a device with relatively poor projected performance. The maximum operating current for the amplifier is set by the I_c of the weakest point in the device, resulting in a significantly lower drive level for devices where such weak points occur far below the I_c of the bulk of the NbTiN layer. Once a region of the microstrip has gone normal, resistive losses generate heat and further increase its resistance and raise the local temperature of the surrounding superconductor (lowering its I_c or even exceeding T_c for a sufficiently high applied current and initial operating temperature). These effects can be seen by the slow, steady rise in R_{pa} once the current has exceeded such a weak link.

The self-limiting effect of the increase in R_{pa} on the current can be more easily seen by plotting the data in Fig. 4.4 in terms of the applied current rather than voltage. Shown in Fig. 4.5, one can see a small but noticeable decrease in current

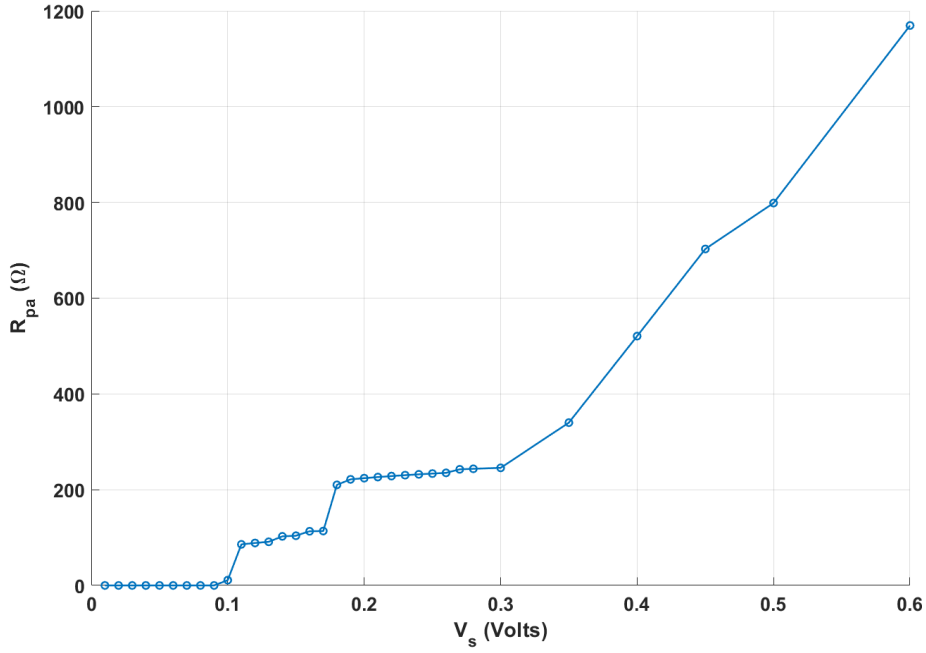

Figure 4.4: An example of the measured R_{pa} for a given applied V_s with $R_s = 1094\,\Omega$ resistance. The sudden increases in resistance at 0.11 V and 0.18 V correspond to weak links being driven normal with full breakdown of superconductivity occurring near 0.3 V as the supplied current reaches the critical current of the bulk of the microstrip.

as the amplifier resistance jumps to 200 Ω. The steady rise in R_{pa} in the previous plot is also explained by the negative feedback of the rise in resistance on the supplied current. As the supplied voltage increases so does the amplifier resistance, meaning the current will remain at I_c until a sufficient voltage is applied to suppress superconductivity across the whole device.

This screening procedure reveals a few crucial pieces of information. First, one can estimate the yield by discarding devices that are open, have shorts to ground, or have very low critical currents. Second, it calibrates the overall quality of the NbTiN film by the relative difference between current at which the weakest links in the film go normal and the current at which the resistance starts climbing rapidly. Finally, it identifies the devices with the highest potential gain due to their large critical currents.

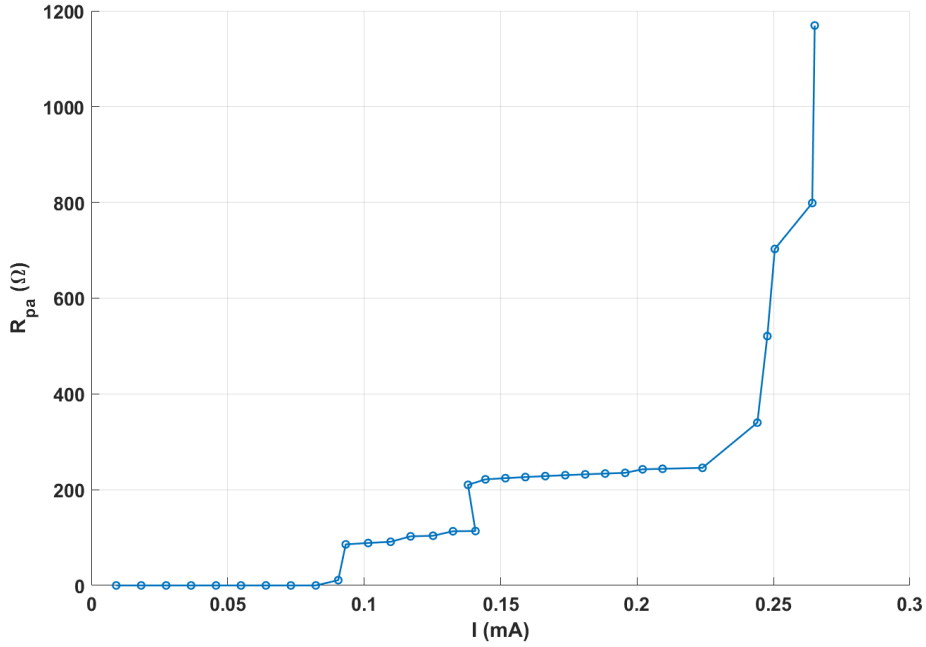

Figure 4.5: An example of the measured R_{pa} vs the applied current.

4.2 Parametric Amplifier Characterization

Once promising chips have been identified through the DC screening, they are mounted in individual housings and wire bonded, ensuring that the sky plane has an excellent RF connection to ground. These devices are then cooled in either a liquid Helium or inserted into a cryostat for further testing.

Gain

The basic gain measurement system we use for initial testing of our devices is shown in Figure 4.6. The parametric amplifier power gain (in dB) is measured to be simply

$$G = 20 \log_{10} \left[\frac{S_{21}^{\text{on}}}{S_{21}^{\text{off}}} \right] \tag{4.6}$$

where S_{21}^{off} is the transmission measured by the VNA without an applied pump and DC current, while S_{21}^{on} is the operating state. While comparing the device transmission in the on and off states is a natural choice for defining gain, it comes with certain disadvantages for three-wave-mixing devices.

The inductance of the transmission line changes with applied DC current (equation 2.5), and this increase of inductance lowers the phase velocity of light through the

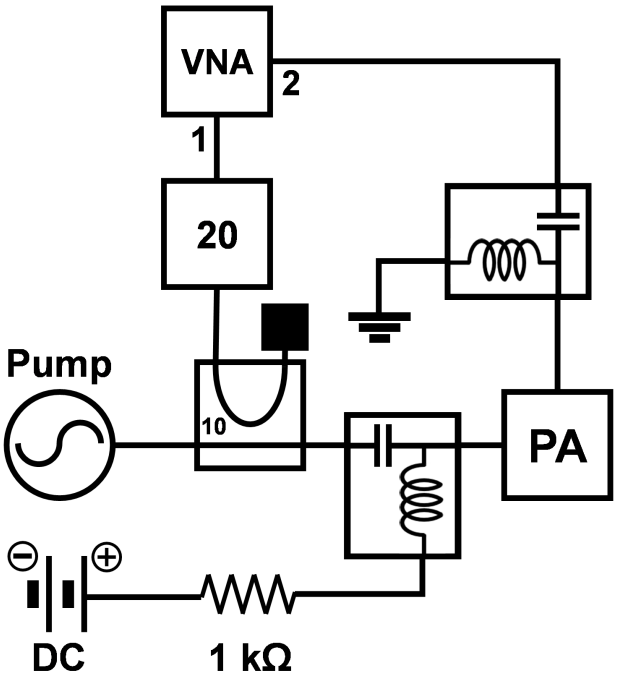

Figure 4.6: A schematic diagram of the typical gain measurement setup consisting of a VNA combined with a pump and DC current through a directional coupler. All components excluding the amplifier are at room temperature.

line (equation 2.24). Impedance mismatches for the amplifier will result in ripples in the S_{21}[90], the frequency spacing of which is set by the spacing of standing waves formed by the reflection $\delta\nu = v_{\text{ph}}/2L$. Thus, as the phase velocity changes with applied DC current, the ripple spacing changes.

Furthermore, the frequency of the photonic band gap introduced for dispersion engineering in 2.55 also depends on frequency and can shift significantly with applied current (see Figure 4.7 for one example). Using the definition for gain in equation 4.6 would thus result in an unintuitive result at the frequencies near the shifting band gap and a gain ripple that is the combination of both the shift in the standing wave ripple and the inherent gain ripple of the device. Thus, in the three-wave-mixing case, taking S_{21}^{off} as the S_{21} with the DC bias turned on (but the pump turned off) gives a more accurate representation of the amplifier gain. This definition is still not perfect as the AC power provided by the pump will have a similar (albeit smaller) effect on the inductance and phase velocity.[91]

In principle, the optimal three-wave-mixing gain should occur near $I_{\text{DC}} = I_p = I_c/2$, so we begin by setting $I_{DC} = I_c/2$. Next, we choose a pump frequency ω_p according

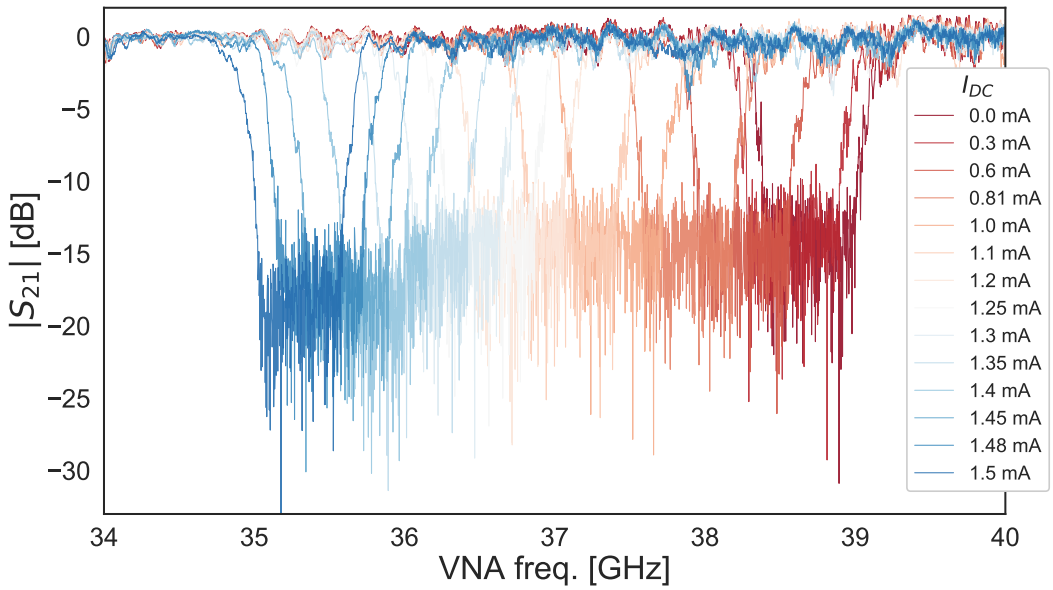

Figure 4.7: S_{21} near the band gap of a device measured at 1K for various applied bias currents, illustrating the downward shift of the band gap with increasing bias current. The transmission is normalized by subtracting a linear baseline determined by fitting the data outside the band gap.

to the design specifications and slowly raise I_p until superconductivity breaks down and the device goes normal. Due to the frequency dependence in the transmission of the measurement system, the fraction of power supplied to the parametric amplifier will depend on pump frequency, so the maximum supplied power changes with ω_p. After power cycling the applied currents to restore the superconducting state, the pump is returned to a level 1 or 2 dB lower than the breakdown occurred to accommodate for this frequency dependence.

The pump frequency systematically swept in 100 MHz steps to search for regions producing noticeable gain ($>$ 5 dB). Those regions are then similarly swept in 10 MHz steps to look for areas with the most promising gain profiles in terms of gain level, bandwidth, and ripple size. Once these potential ω_p have been identified, the search is repeated in 1 MHz steps, this time also raising the pump power I_p to the maximum level before superconductivity breaks down. The best operating conditions are stored, and the corresponding VNA sweeps are recorded. Ideally, this search is then repeated across a broad range of applied DC currents.

It should be expected that the operating conditions for maximizing gain slightly deviate from the theoretically designed parameters. Note that the optimal phase matching condition in equation 3.34 depends on the maximum pump amplitude,

I_p. If this value was not perfectly predicted, then the optimal pump frequency for maintaining the phase matching criterion will also change.

Over the past few years, we have characterized the gain of close to a hundred different travelling-wave parametric amplifiers. The following figures reproduce the measured gain performance of a few selected devices that do not appear in other sections of this thesis. We are able to fairly consistently design amplifiers with measured gain relative to the un-pumped transmission exceeding 20 dB across an octave or greater of bandwidth. The applied DC current and pump power varies both between devices and operating conditions, with different ratios of current and pump power capable of producing similar gain profiles. The pump power applied for producing optimal gain typically falls within the range of -35 to -25 dBm, while the corresponding DC current in the three-wave-mixing devices is on the order of 0.5 to 0.2 mA. Saturation occurs for input signals with power levels on the order of -60 to -55 dBm depending on the device, using the conventional definition of 1 dB gain compression.

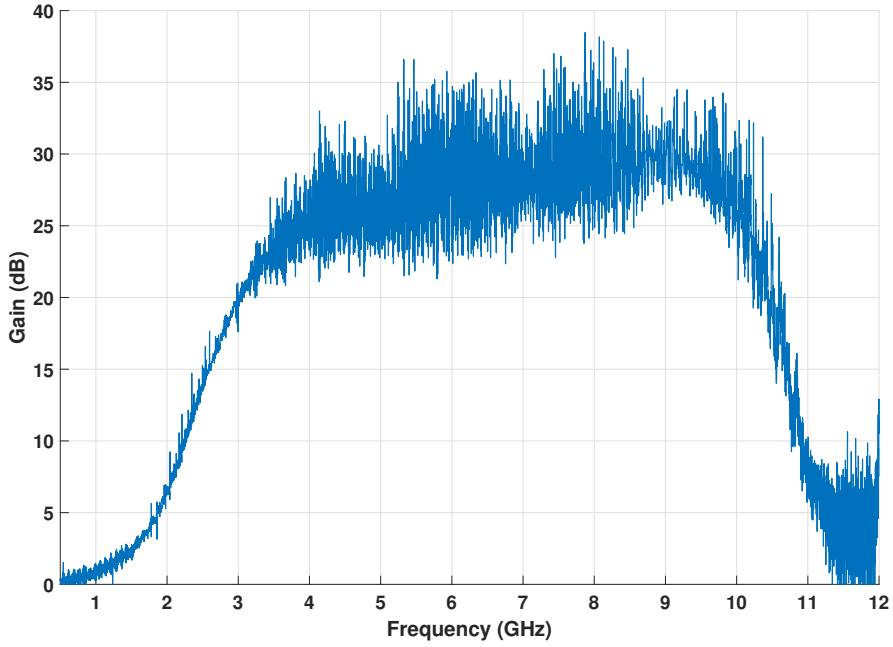

Figure 4.8: Three-wave-mixing gain with a 12.1 GHz pump measured at 4K.

Although these devices were designed for three-wave-mixing amplification, we occasionally also see a significant amount of four-wave-mixing gain when a pump is applied below the designed band gap. Figure 4.10 shows one such device where

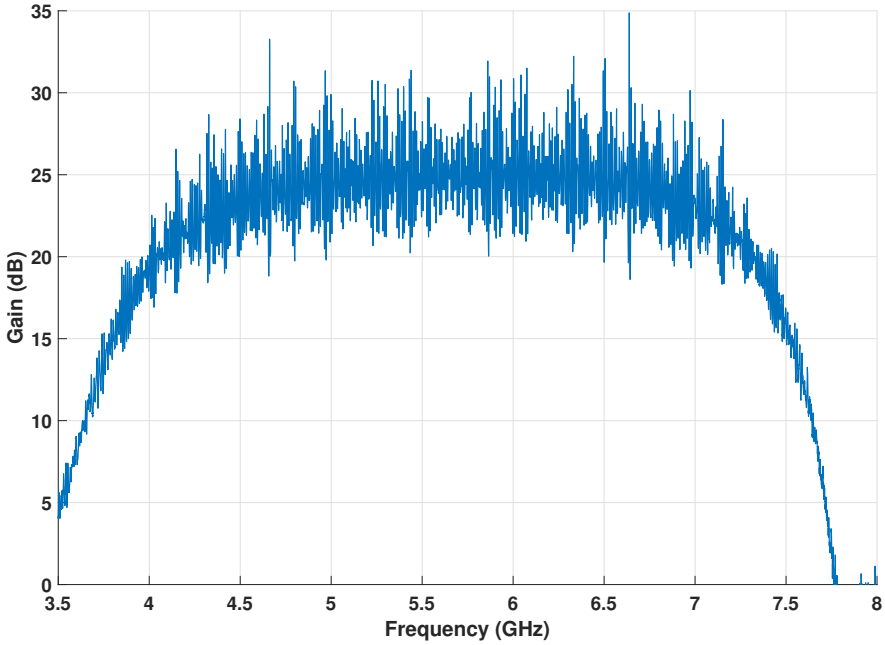

Figure 4.9: Three-wave-mixing gain with an 11.3 GHz pump measured at 4K.

the band gap is used to block the pump's third harmonic, and Figure 4.11 achieves the optimal phase matching condition between a low frequency signal and an idler just above the band gap frequency. Naturally, the lack of intentional dispersion engineering limits the bandwidth of the amplifiers when operated in this mode, but such devices are potentially useful due to the low frequency at which they obtain gain.

Other Parametric Processes

In addition to characterizing the parametric amplifier gain, it is useful to investigate the efficiency of other parametric processes that may degrade device performance as discussed in section 3.2.

The presence of these undesired parametric processes can be identified through pump depletion.[92] By connecting the output of our system in Figure 4.6 to a spectrum analyzer rather than the second port of the VNA, we can measure the ratio of the input and output pump power, which should be constant if there is no efficient parametric conversion. Because the efficiency of parametric processes scales with pump power (a natural result of the coupled mode equations in 2.2), the fraction of missing pump power will not be constant in their presence. If the output of these

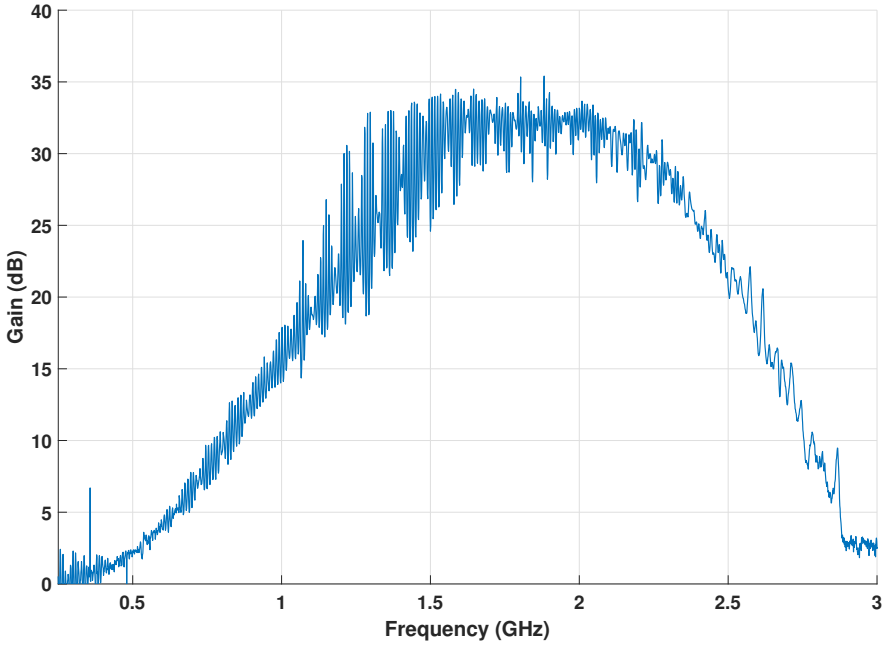

Figure 4.10: Four-wave-mixing gain from a 4 GHz pump measured at 4K.

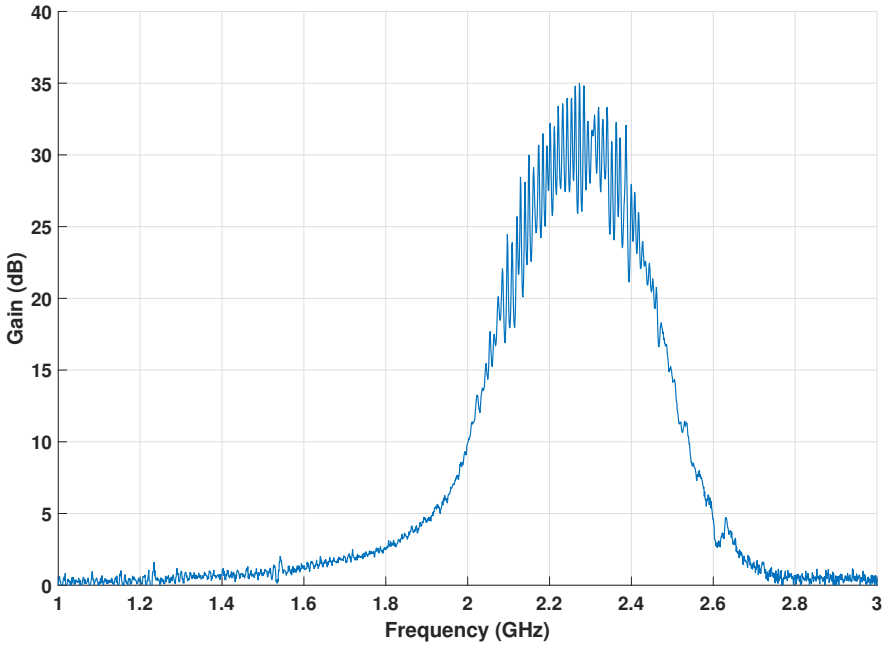

Figure 4.11: Four-wave-mixing gain from a 7.8 GHz pump measured at 4K.

processes falls within the readout range of the spectrum analyzer, they can be easily identified by noting the frequency of the spurious output signal peaks that are not present in the input.

Some frequency conversion processes can be identified without the use of a spectrum analyzer as they create a noticeable change in the S_{21} as measured by the VNA. Up-conversion of a signal from ω_s to ω_o in both in the three-wave-mixing ($\omega_o = \omega_p + \omega_s$) and four-wave-mixing ($\omega_o = 2\omega_p + \omega_s$) forms results in what appears to be a deamplification of the signal with rising pump power during a VNA measurement.

Some degree of deamplification is ubiquitous across our three-wave-mixing designs, especially when the pump is applied well below the designed frequency. Figure 4.12 shows the effect of a 4 GHz pump applied to one of our devices with a designed pump frequency near 15 GHz. Because the device had minimal dispersion at these frequencies, there was strong second and third harmonic generation, allowing for numerous efficient up-conversion processes. As the pump strength is increased, the majority of the low-frequency signal vanishes from the VNA sweep due to up-conversion.

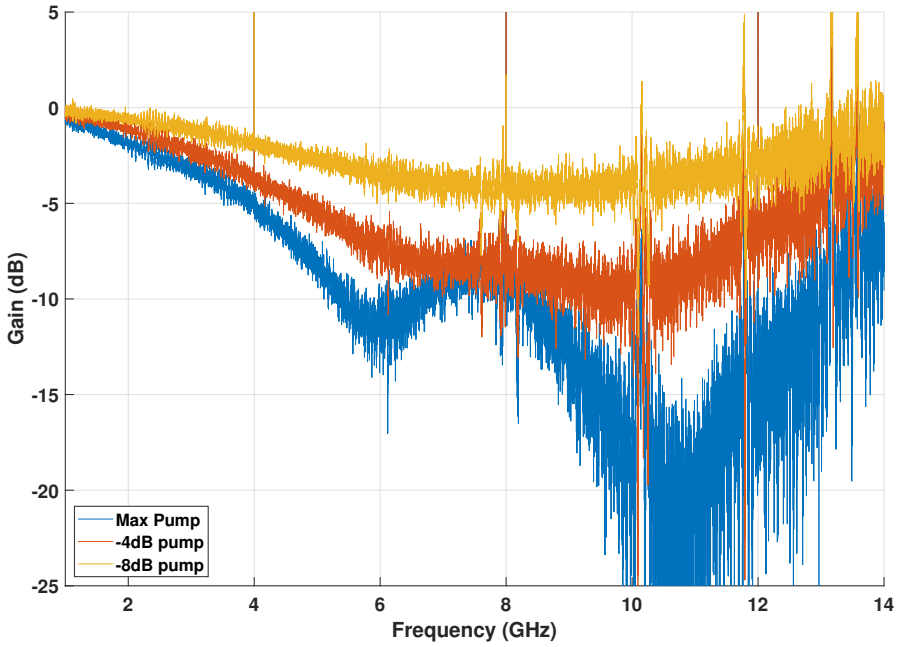

Figure 4.12: Broadband deamplification from a 4 GHz applied pump and 0.15 mA DC bias with various levels of pump power.

Under normal operating conditions, these effects are not as pronounced but can

manifest as asymmetries in the gain profile. Note that the coupled mode equations derived in 2.42 and 2.25 are symmetric under a relabeling of 'signal' and 'idler,' meaning the gain must also be symmetric across reflections over the center of the gain band. Any asymmetries in the gain profile are thus the result of other parametric gain mechanisms (such as unintended four-wave-mixing in a primarily three-wave-mixing device) or frequency conversion processes.

Weak Spots

In addition to identifying weak spots using the discontinuities in resistance when screening the device at DC, we can gain more information on device health by performing time domain reflectometry.[93] By observing the S_{11} or S_{22} in the time

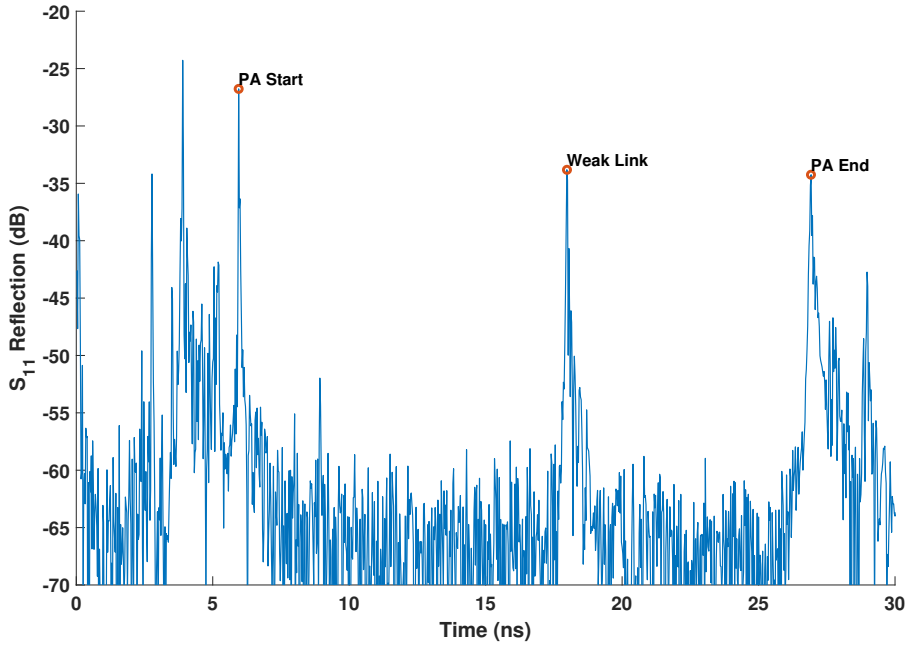

Figure 4.13: S_{11} time-domain measurements of a parametric amplifier. The readout power of the VNA exceeds the critical current of a single weak link along the microstrip, driving that region normal and generating a reflection. The unlabeled reflections corresponds to other components of the measurement: the bias tees and directional coupler shown in Figure 4.6.

domain, we can identify the components responsible for each round-trip reflection by considering the physical length and phase velocity of the coaxial cables connecting them. As the readout power of the VNA is gradually increased, defects in the transmission line will manifest as a reflection as shown in Figure 4.13. Amplifiers

with several weak links will see additional reflections arise as the power is increased further. Using the time domain data, we can roughly identify the physical position of these weak links along the transmission line, which can be subsequently imaged for insights about the fabrication procedure which caused them.[93]

Reflections and Parametric Oscillation

One of the main limiting factors in parametric amplifier performance has been the formation of parametric oscillation. A continuous signal I_{in} at the input of the parametric amplifier will result in an output signal of

$$I_{\text{out}} = S_{21} I_{\text{in}} \tag{4.7}$$

where S_{21} is the transmission of the device, where the gain $G = |S_{21}$. If $S_{22} \neq 0$, then a portion of this output signal will be reflected back into the device. As the signal propagates backwards through the amplifier, it does not experience any gain due to the phase-matching criterion. Then, if the input is also not perfectly reflectionless, some portion of the signal will be sent back for another trip through the amplifier. The overall output signal is thus

$$I_{\text{out}} = S_{21} I_{\text{in}} \left(1 + S_{22} S_{12} S_{11} S_{21}\right) \tag{4.8}$$

where the additional term picks up all the S-parameters (one from each input reflection, output reflection, forward transmission, and backwards transmission through the device). Because this new signal is similarly subject to input and output reflections, the overall output of the system will be

$$I_{\text{out}} = S_{21} I_{\text{in}} \sum_{N=0}^{\infty} \left(S_{22} S_{12} S_{11} S_{21}\right)^N . \tag{4.9}$$

The sum converges to a value of

$$\sum_{N=0}^{\infty} \left(S_{22} S_{12} S_{11} S_{21}\right)^N = \frac{1}{1 - S_{22} S_{12} S_{11} S_{21}} \tag{4.10}$$

when (again using $G = |S_{21}|$)

$$G \left|S_{22} S_{12} S_{11}\right| < 1. \tag{4.11}$$

If it does converge, the overall output has a strong dependence on the overall phase picked up by the signal on the round-trip, $2\phi(\nu)$ where $\phi(\nu)$ is the phase delay through the device, as the reflected waves will constructively or destructively

interfere with one another. The log of the ratio between the two limiting cases where $2\phi(\nu) = 2\pi n$ and $2\phi(\nu) = \pi(2n+1)$ for some integer n:

$$-10\log_{10}\left(\frac{1+G\,|S_{22}S_{12}S_{11}|}{1-G\,|S_{22}S_{12}S_{11}|}\right) \tag{4.12}$$

gives the peak-to-peak amplitude of the transmission (or gain) ripple of the amplifier in dB. As expected, when the reflection coefficients at the input and output of the device are zero, there is no resulting ripple. Notably, and unfortunately for the amplifier performance, the ripple size is highly nonlinear with the gain. For example, a 0.1 dB ripple in the transmission when the amplifier is off ($G = 1$) grows to a 3 dB ripple when the amplifier is turned on to a 15 dB gain. Reducing the ripple in the gain curve requires exceptional impedance matching for the amplifier itself.

When the gain of the amplifier exceeds the round trip reflection and transmission losses,[94] the reflected signal gains in power on each subsequent set of reflection rather than diminishes to zero. Once this occurs (the criterion in equation (4.11) is broken for any frequency), the sum in equation (4.9) diverges, and the output power formally goes to infinity. In practice, the amplifier starts to oscillate, converting power from the pump frequency to the parametric oscillation frequency, which lowers the gain until a steady state is reached.

This process of parametric oscillation sets another limit on the maximum gain that can be achieved by the amplifier. As an example, Figure 4.14 shows a portion of the gain curve of an amplifier with gain limited due to the formation of a runaway cavity mode at 4.57 GHz. Note how the gain steadily increases with pump power until the ripple at a single frequency grows to produce nearly 50 dB of gain. Increasing the pump power further produces no additional broadband gain since the additional pump power is consumed by this mode until the resulting pump depletion lowers the gain back to the steady state.

The onset of parametric oscillation creates an additional metric by which we can judge the quality of an amplifier within the context of a particular measurement system. The gain of the amplifier should nominally increase as the applied pump power increases, until I_p exceeds I_c resulting in the breakdown of superconductivity. If the gain saturates at an $I_p < I_c$, then the scale of the difference between the two can be used to calculate how much potential gain was lost due to poor impedance matching.

As our parametric amplifier designs have improved, the overall gain has more frequently become limited by parametric oscillation rather than the applied pump

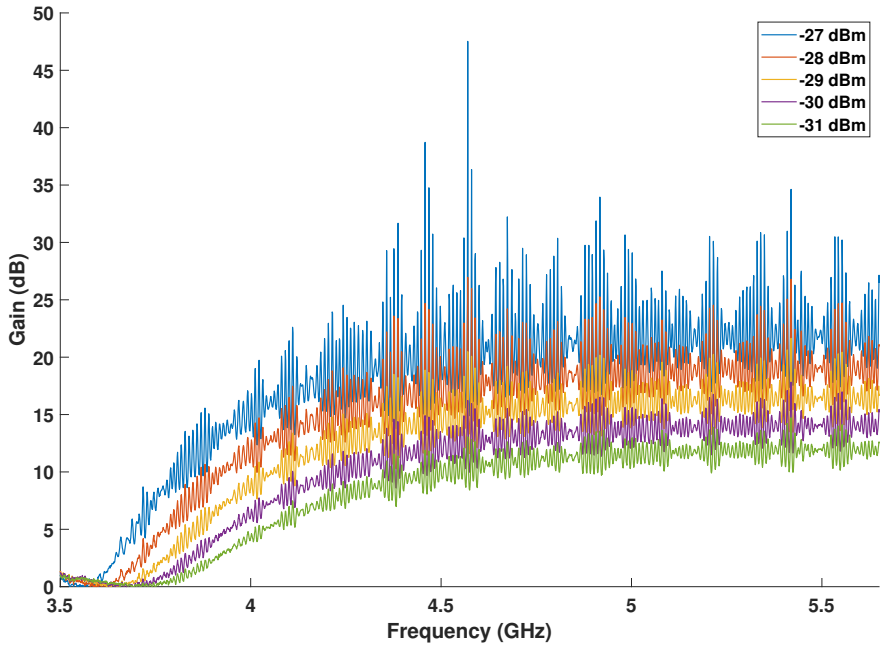

Figure 4.14: A portion of the gain of a three-wave-mixing amplifier with an 11.3 GHz pump as a function of pump power.

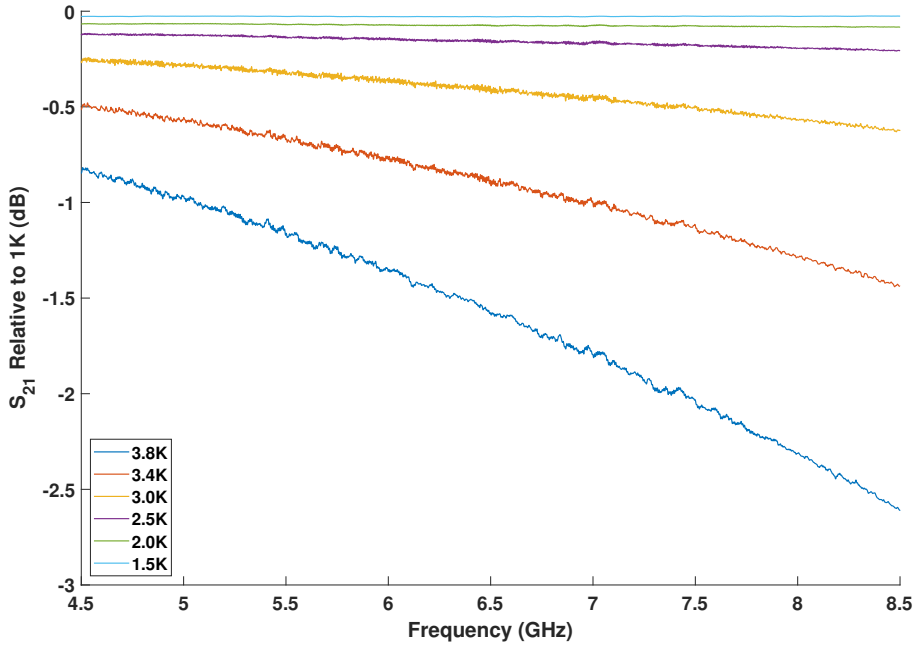

Figure 4.15: Excess attenuation as a function of temperature compared to the S_{21} of the amplifier at 1K.

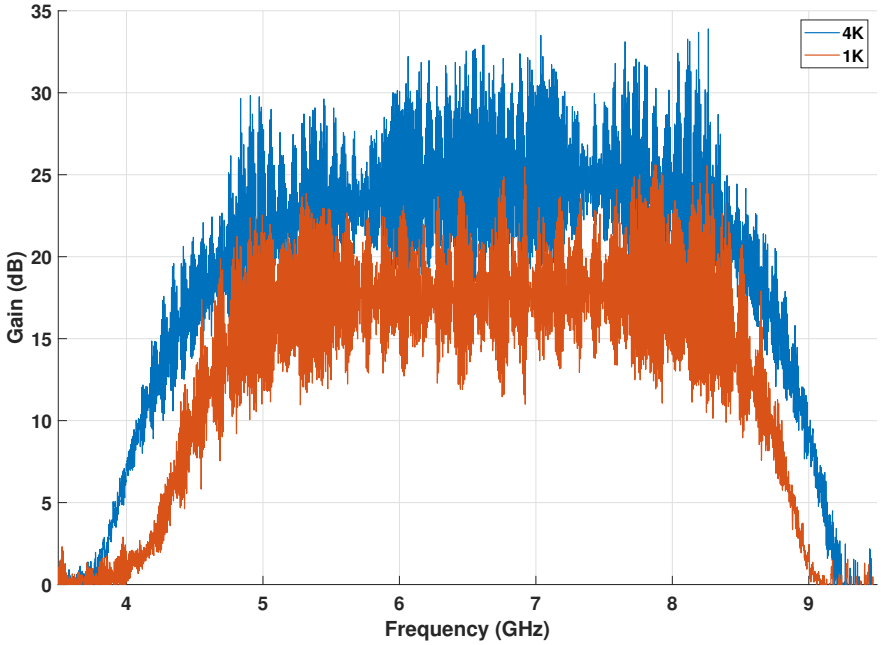

Figure 4.16: Three-wave-mixing gain of a parametric amplifier with an 13.1 GHz pump at 4K (blue) and 1K (red). Both gain curves are calculated relative to the un-pumped transmission at their own temperature.

power. This is particularly evident when comparing device performance when operated at different temperatures. In our NbTiN amplifiers, RF losses rapidly increase at the temperature exceeds 2 Kelvin, particularly at higher frequencies (see Figure 4.15). As noted in equation 4.11, the resulting decrease in $|S_{21}|$ and $|S_{12}|$ allows for twice as much of an increase in gain before the onset of runaway parametric oscillation. The corresponding increase in gain for this device is shown in Figure 4.16 demonstrating a significant degradation in device performance at low temperatures.

While it was not written explicitly, the quantities in the expressions above are all frequency-dependent. As a result, it is possible to maintain excellent amplifier performance with only moderate gain ripple if $S_{11}(\nu)$ and $S_{22}(\nu)$ are only large in regions where $G(\nu)$ is small. It is also worth noting that the reflection coefficients of the amplifier itself are not the only concern for staying beneath the cavity mode formation condition in equation (4.11). A similar expression could be derived in an identical manner for the reflections formed by components before and after the amplifier that might also result in parametric oscillation. As a general guideline,

if the S_{11} and S_{22} are limited to below $-X$ dB then the maximum amplifier gain will at best be roughly $2(X + L)$ dB, where L is the loss between the amplifier and those components. These considerations lead to a practical impact on the noise measurement setup for maximizing gain, as will be discussed in the following section.

4.3 Noise Measurement Setup

We characterize the noise of our low frequency (< 16 GHz) parametric amplifiers using a modified Y-factor technique. In a traditional y-factor noise measurement, a variable temperature load (supplying a noise P_{in}) is connected to the input of an amplifier, and the output power of the system is measured:

$$P_{\text{out}} = |S_{21}^{\text{system}}|^2 G \left(P_{\text{in}} + P_{\text{amp}}\right) \tag{4.13}$$

where G is the gain and P_{amp} is the amplifier noise.[71] By performing this measurement for various known values of the input load, P_{in}, one can easily calculate the amplifier noise without the need to know the transmission and gain of all subsequent readout electronics (S_{21}^{system}).

For our measurements, we employ a modified version of this method by inserting a switch that connects to our variable temperature loads or parametric amplifier output. In this scheme, we instead perform four measurements of the output power:

$$\begin{aligned} P_{\text{out}} &= |S_{21}^{\text{system}}|^2 G \left(P_{\text{in}} + P_{\text{amp}}\right) \\ P'_{\text{out}} &= |S_{21}^{\text{system}}|^2 P_{\text{in}} \\ P''_{\text{out}} &= |S_{21}^{\text{system}}|^2 P_L \\ P'''_{\text{out}} &= |S_{21}^{\text{system}}|^2 P_H \end{aligned} \tag{4.14}$$

corresponding to the case with the parametric amplifier on, parametric amplifier off, low temperature load, and high temperature load, respectively. The final two measurements calibrate the system's response to an input load of known temperature (or power) which then allows us to calibrate the noise power from the amplifier on measurement to a noise temperature referred to the input of the device.

While the overall measurement scheme has remained the same, the exact noise measurement setup we use has changed with each cryostat cooldown as we have discovered flaws that reduced amplifier performance, built accommodations for amplifiers with varying operating frequencies given available components, and shared readout systems across multiple experiments. Figure 4.17 shows the final

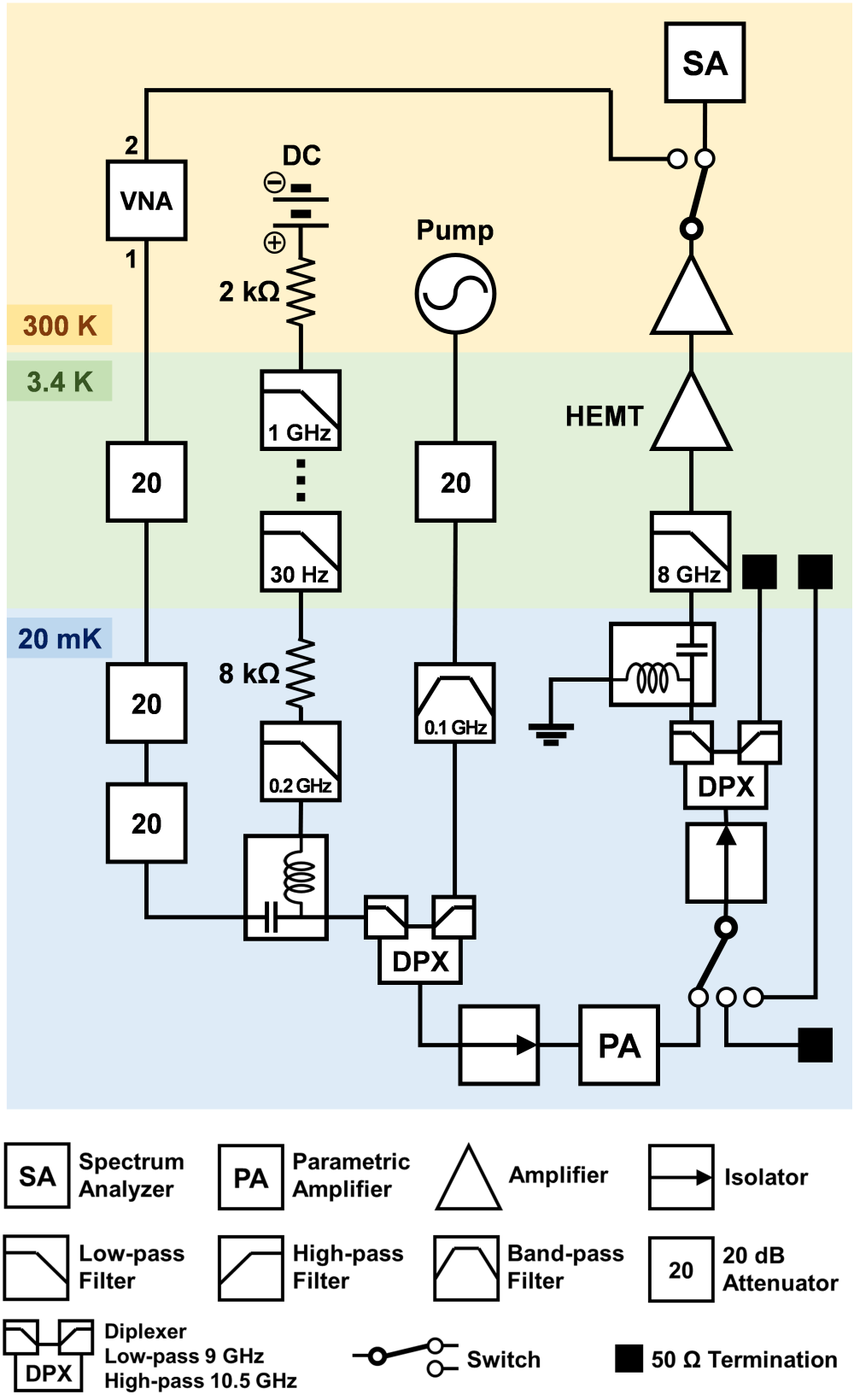

Figure 4.17: A typical noise measurement setup.

outcome of these iterations as of the writing of this thesis. The following sections discuss the motivations behind the choices made in its construction followed by some recent results and corresponding analysis of the noise performance of one of our devices.

Input Channel

If we want to measure an added noise contribution near the quantum limit, we must operate in the regime where the half photon vacuum fluctuations dominate over the Johnson-Nyquist noise per unit bandwidth at the amplifier input, which implies

$$\frac{1}{2}h\nu \gg kT. \tag{4.15}$$

For one of our typical parametric amplifiers operating in the 4-10 GHz range, this corresponds to an input noise temperature that is lower than 100 mK. The cold stage of our dilution refrigerator can maintain a stable temperature of 20 mK, but we must also ensure that the noise contributions from the input lines do not exceed this temperature.

This is achieved by sufficient attenuation of the input line at each stage of the cryostat. The roughly 300 K of room temperature noise is lowered by 20 dB at the 3.4 K stage (resulting in 3 + 3.4 = 7.4 K total thermal noise), which is then attenuated by a further set of two 20 dB attenuators at the cold stage for a total of $0.74 + 20 \approx 21$ mK of thermal noise. While this method is sufficient for the input channel, which only supports a weak test tone for gain measurements, supplying a sufficient level of pump power would not be possible through that degree of attenuation. Our devices typically operate in with a supplied pump of a few μW at the device input. 40 dB of attenuation at the cold stage would thus require supplying several mW of power at the cold stage, most of which is dissipated as heat in the attenuators and creates an unsustainable thermal load on the cold stage for maintaining the 20 mK base temperature.

Pump Insertion

The pump is thus brought in using a second channel, which also contains a 20 dB attenuator at the 3.4 K stage, but instead uses a combination of filters at the cold stage to reach the required level of suppression for the thermal Johnson noise. We accomplish this using a narrow ($\sim$100 MHz), tunable, reflecting band-pass filter which is then coupled to the signal through the high-pass port of a diplexer. The combined low-pass transmission of these two components provides even stronger suppression

of the thermal noise in the gain bandwidth while also similarly suppressing pump phase noise.

Notably, this method for input noise suppression through the pump channel does not filter the the thermal noise at the pump channel. To first order, the amplifier added noise to the signal is only affected by the noise at the idler frequencies, but fluctuations in the pump amplitude can also couple to the signal through the resulting variance in the amplifier gain.[95] Consider the case for the optimal three-wave-mixing exponential gain of

$$G_s = \frac{1}{4} e^{2\Delta\phi_p L}. \tag{4.16}$$

The parameter $\Delta\phi_p$ depends linearly on the applied pump power, P_p, times some constant, so we can define $a_p P_p = \Delta\phi_p L$. Using standard error propagation, the standard deviation of the gain in terms of the fluctuations in the pump will be

$$\sigma_G = \left(\frac{\partial G_s}{\partial P_p}\right) \sigma_P = 2 a_p G_s \sigma_p. \tag{4.17}$$

Furthermore, we can rewrite equation 4.16 as

$$a_p P_p = \frac{1}{2} \ln (4 G_s) \tag{4.18}$$

which then simplifies the above expression to

$$\sigma_G = G_s \ln (4 G_s) \frac{\sigma_p}{P_p}. \tag{4.19}$$

In the limit where the pump amplitude fluctuations are dominated by the Johnson noise, $\sigma_p = P_N$, we would like for the fluctuations in the linear gain to remain small, $\sigma_G \ll 1$. This is achieved when

$$\frac{P_N}{P_p} \ll \frac{1}{G_s \ln(4 G_s)}. \tag{4.20}$$

For an amplifier with 20 dB gain, this condition is achieved when the pump power is more than 1000 times larger than the thermal noise power within its bandwidth (the width of the pump tone). A simple calculation of the thermal Johnson-Nyquist noise, $P_N = 4kTB$ using the effective 7.4 K noise temperature of the 20 dB attenuator is many orders of magnitude lower than the pump power of a few μW, even for a very generous choice of bandwidth. Thus, while we need not worry about thermal noise near the pump frequency impacting our measurement, the pump power should be kept stable to within a fraction of a percent if we wish to maintain gain stability.

DC Bias

Maintaining a stable gain imposes similar considerations for fluctuations in the DC bias current for identical reasoning. This is achieved by using a series resistance of a few kΩs to allow for supply voltages of several Volts for a 1 mA current. The DC bias then passes through numerous low-pass filters with cutoffs between a 30 Hz and 1 GHz to further limit any fluctuations.

Reference Loads

In order to calibrate the noise equivalent power from the parametric amplifier, we need a known absolute reference at the same location in the system. A cold switch is inserted immediately after the parametric amplifier connecting to the amplifier, a 50 Ω termination (cold stage), and a second 50 Ω termination at the 3.4 K stage connected through a superconducting coax with minimal loss. Given the terminations are properly impedance matched and their temperature is known, we can use the cold switch to directly compare the output system's response from the known loads to the parametric amplifier signal, calibrating its power without the necessity of knowing the losses and gains of all the subsequent components in the common path.

When the parametric amplifier is off, the output of the cold switch sees a combination of the emission of the 20 dB attenuators at frequencies below the diplexer cutoff and the thermal signal passing through the band-pass filter above it. As calculated above, the noise output from the final 20 dB attenuator is nearly identical to a 20 mK load. Because the following components (diplexer, bias tee, isolator, and unpumped parametric amplifier) are all passive components also at 20 mK, the overall power spectrum in the amplifier off state after the cold switch will be identical to that of the 20 mK load. Thus, the cold stage load is ultimately unnecessary for this measurement.

The introduction of a cold switch and placement of the calibration loads at the amplifier output rather than input has the minor added benefit of avoiding complications and potential measurement error associated with input noise at the idler.[63] Our scheme provides a calibrated measurement of the output noise temperature of the parametric amplifier, which can be referred to the input of the parametric amplifier by dividing by the measured gain.

Post-Amplification

Our measurement procedure relies on the spectrum analyzer accurately differentiating the signal power emitted by the 20 mK and 3.4 K loads. To achieve this, we use a low noise HEMT amplifier, specifically the Low Noise Factory LNF-LNC0.3_14A,[96] which provides 37 dB of gain and noise temperature that is not much higher than 3 K across our measured range of frequencies.

The DC current path is terminated by a short to ground, while the pump is separated from the signal using a diplexer and terminated at the 4K stage. Any pump power that escapes through the low-pass port of the diplexer is attenuated using a low-pass filter prior to the HEMT to ensure we stay well below its 1 dB compression point.

The signal is then further amplified by a room temperature amplifier, typically the Mini-Circuits ZVA-183-S+[97] which provides an additional 26 dB gain. The SM200A spectrum analyzer settings are further chosen to minimize its internal input attenuation and maximize the gain.[98]

Reflection Considerations

As discussed in section 4.2, any amount of input and output reflections could actively degrade the parametric amplifier performance, which poses a particular problem for the noise measurement setup. Each additional component required for the measurement (diplexers, bias tees, HEMT, cold switches) slightly increases the amount of reflections through the amplifier, and the low temperature and superconducting coaxial cables used throughout limit the loss for round-trip signals.

These effects ultimately result in severely degraded amplifier performance, often with 5-10 dB lower gain prior to the onset of parametric oscillation when compared to other setups where the small amount of loss in between the other components and the amplifier suppresses their contributions to the round-trip reflected signal.

To suppress these effects, we place two isolators immediately before and after the parametric amplifier to suppress round-trip reflections from all other components. Unfortunately, an isolator placed after the amplifier but prior to the cold switch connecting the thermal loads used to calibrate the noise measurement would become a non-common path component whose transmission would need to be compensated for in the analysis. We have attempted to do so, but found it infeasible to perform the necessary calibrations to the degree of accuracy required for a clean noise measurement.

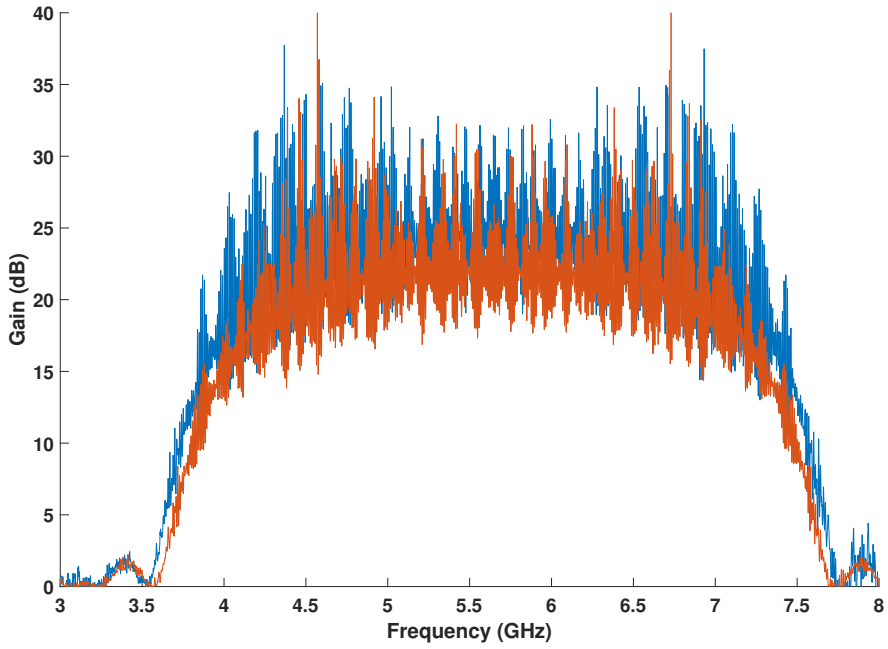

Figure 4.18: The three-wave-mixing parametric amplifier gain obtained in two version of our noise testing setup. Both the red and blue data were taken using the same parametric amplifier driven by an 11.3 GHz pump. The red curve corresponds to the experimental setup given in Figure 4.17. The blue curve was taken with the second isolator moved before the cold switch but an otherwise identical setup.

We choose to avoid these systematics and place the second isolator as close to the parametric amplifier as possible but within the common path of the thermal loads, attaching it directly to the cold switch output. Even this minor concession of a single non-amplifier component between the isolators measurably impacts the highest achievable gain. Figure 4.18 shows the maximum gain obtained for a parametric amplifier within this noise testing setup for these two isolator placements. The gain was reduced by nearly 2 dB in the configuration necessary for the Y-factor measurement.

4.4 Y-Factor Noise Measurement

Consider a load with a known temperature, T, located at the position of the parametric amplifier output. The power emitted by that load proceeds through the rest of the measurement system with some unknown gain and attenuation, resulting in a measured output power $P(\nu)$. Taking two such loads with a low (T_L) and high (T_H) temperature, we measure corresponding output powers from the system of P_L and

P_H. Using the slope

$$m = \frac{P_H - P_L}{T_H - T_L} \tag{4.21}$$

and y-intercept

$$y_0 = P_L - mT_L. \tag{4.22}$$

we can calibrate any measured power P to the output of a load with equivalent temperature via

$$T = \frac{P - y_0}{m} \tag{4.23}$$

assuming the relationship between power and temperature is linear.

At low temperatures, the Johnson noise emitted by a load will not be linear in temperature due to quantum mechanical effects, meaning we cannot directly perform the simple Y-factor calculation as described above.[99] Rather than perform the noise calculation using the nonlinear power, it is more convenient to transform to a coordinate system where the output is linear. To derive the necessary coordinate transformation, we can consider the mean energy of an oscillator with a natural frequency, ν, and a temperature, T, given by [100]

$$E(\nu, T) = \frac{1}{2}h\nu + \frac{h\nu}{e^{\frac{h\nu}{kT}} - 1}. \tag{4.24}$$

The first term, which corresponds to the zero-point fluctuations, dominates at low temperatures (where $kT \ll h\nu$). At higher temperatures (where $kT \gg h\nu$), this relation approaches the limit where it reproduces the expected scaling of

$$E(\nu, T) \simeq kT. \tag{4.25}$$

Expressed in another manner, we can rewrite the above equation as

$$E(\nu, T) = \frac{1}{2}h\nu \coth \frac{h\nu}{2kT}. \tag{4.26}$$

We can then reproduce the high temperature linear scaling of $E \simeq kT$, by defining a new T_{eff}

$$T_{\text{eff}}(\nu, T) = \frac{E(\nu, T)}{k} = \frac{h\nu}{2k} \coth \frac{h\nu}{2kT} \tag{4.27}$$

which acts as a coordinate transformation that linearizes the measured power with respect to noise temperature. Due to this transformation, rather than working in terms of noise temperature, it is often more natural to work in terms of noise quanta.

The noise quanta at a given frequency from a corresponding noise temperature is given by the standard relation [43]

$$\begin{aligned} n(\nu, T_{\text{eff}}) &= \frac{kT_{\text{eff}}}{h\nu} \\ n(\nu, T) &= \frac{1}{2} \coth \frac{h\nu}{2kT}. \end{aligned} \tag{4.28}$$

With this transformation in mind, we perform a series power measurements with the spectrum analyzer for four configurations of the system:

1. $P_H(\nu)$: 3.38 K (T_H) load
2. $P_L(\nu)$: 20 mK (T_L) load
3. $P_{\text{on}}(\nu)$: Parametric amplifier on
4. $P_{\text{off}}(\nu)$: Parametric amplifier off

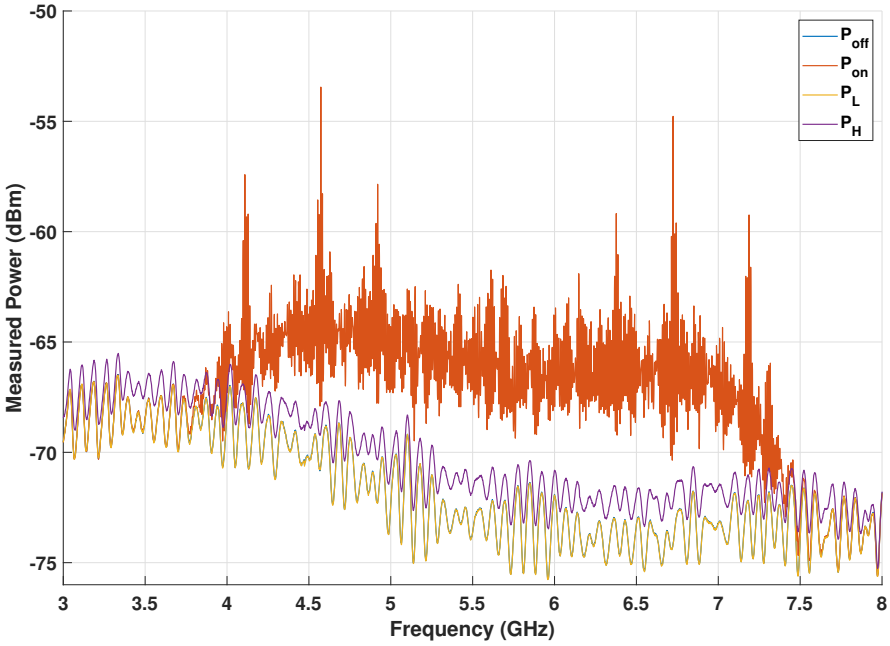

Figure 4.19: Raw spectrum analyzer data used for the y-factor noise measurement. Because P_{off} and P_L are nearly identical, only the latter is clearly visible.

The raw data obtained from these curves is shown in Figure 4.19. As noted in section 4.3, there is no measurable difference between the parametric amplifier off case and low temperature load in our measurement setup. The gain of the amplifier in this measurement configuration is given in Figure 4.20. This particular device is

86 mm in length and uses our standard 250 nm wide and 35 nm thick NbTiN layer with capacitive fingers of similar dimensions extending every 2 μm. The fingers have an average length of 26 μm that is periodically modulated with an amplitude of 2 μm and 110 μm period.

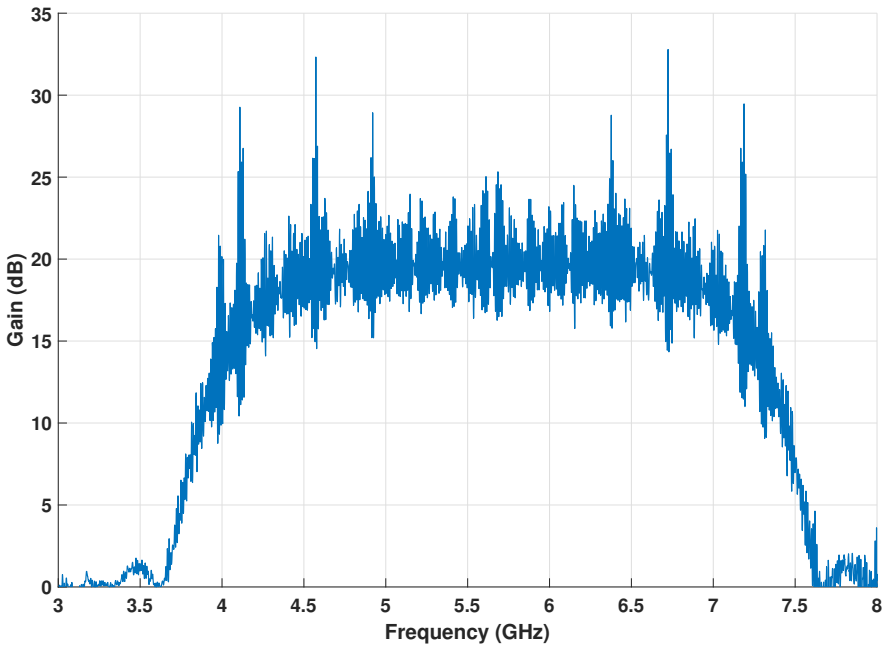

Figure 4.20: The three-wave-mixing parametric amplifier gain measured at 20 mK in the setup shown in Figure 4.17 from an 11.297 GHz -17.2 dBm pump and 0.579 mA DC current.

Using the above calculation, we then define

$$\begin{aligned} T'_L(\nu) &= T_{\text{eff}}(\nu, T_L) \\ T'_H(\nu) &= T_{\text{eff}}(\nu, T_H) \end{aligned} \tag{4.29}$$

and calculate the slope

$$m(\nu) = \frac{P_H(\nu) - P_L(\nu)}{T'_H(\nu) - T'_L(\nu)} \tag{4.30}$$

and intercept

$$y_0(\nu) = \frac{P_L(\nu)T'_H(\nu) - P_H(\nu)T'_L(\nu)}{T'_H(\nu) - T'_L(\nu)}. \tag{4.31}$$

With these quantities at hand, we readily obtain the noise, in units of quanta, referred to the input of the parametric amplifier in both the on and off case:

$$\begin{aligned} N_{\text{on}}(\nu) &= \frac{P_{\text{on}} - y_0}{m}\left(\frac{1}{G(\nu)}\right)\left(\frac{k}{h\nu}\right) \\ N_{\text{off}}(\nu) &= \frac{P_{\text{off}} - y_0}{m}\left(\frac{k}{h\nu}\right) \end{aligned} \tag{4.32}$$

where the factor of $1/G(\nu)$ refers the amplifier on noise to its input rather than out, and the expression $k/h\nu$ converts the units of effective temperature to noise quanta. The amplifier added noise is simply the difference between the on and off cases:

$$A(\nu) = N_{\text{on}}(\nu) - N_{\text{off}}(\nu). \tag{4.33}$$

These measurements and calculation result in Figure 4.21, showing the calculated values from the measured data and the theoretical noise limit for amplifiers as set by 2.89 and the measured gain. As can be seen from the combination of plots, we obtain near quantum-limit noise for an amplifier operated with 20 dB with nearly an octave of bandwidth.

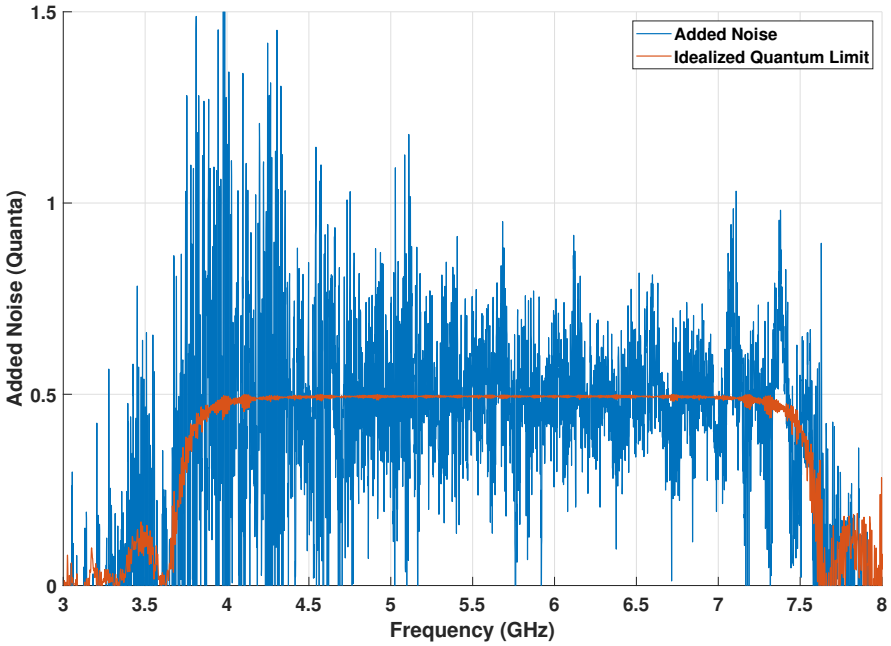

Figure 4.21: The measured added noise in units of quanta for the parametric amplifier operated as described in Figure 4.20 (blue) compared to the theoretical quantum limit (red).

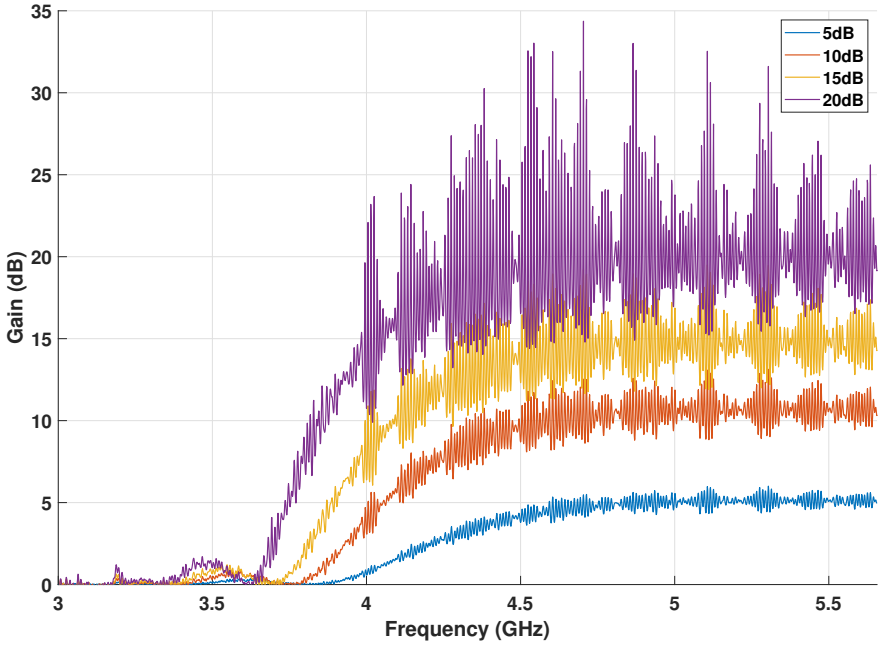

Figure 4.22: The three-wave-mixing parametric amplifier gain measured at 20 mK in the setup shown in Figure 4.17 from an 11.313 GHz pump and 0.583 mA DC current. The applied pump powers of -13.7 dBm (blue), -9.7 dBm (red), -7.7 dBm (yellow), and -5.7 dBm (purple) were chosen to obtain roughly 5 dB, 10 dB, 15 dB, and 20 dB gain, respectively.

While we very consistently see near quantum-limited noise, the measured data does not always match the limit as perfectly as in Figure 4.21 due to an unknown source of noise. As an example, that same device was also measured in a slightly modified setup to Figure 4.17 where the diplexer crossover frequency was near 6 GHz, thus only enabling the measurement of the lower portion of the gain bandwidth. In that configuration, the obtainable gain as a function of applied pump power is shown in Figure 4.22

The measured added noise at these operating points and the corresponding quantum limits are plotted in Figure 4.23. While the measured plots continue to roughly follow the expected quantum limit based on the amplifier gain, there is a small amount of excess noise in the measured values that appears to scale with pump power.

If we turn off the DC current (thereby eliminating all three-wave-mixing amplifier gain) and repeat the noise measurement with just the applied pump power, Figure 4.24 that there is a slight excess in the measured noise despite no amplifier gain

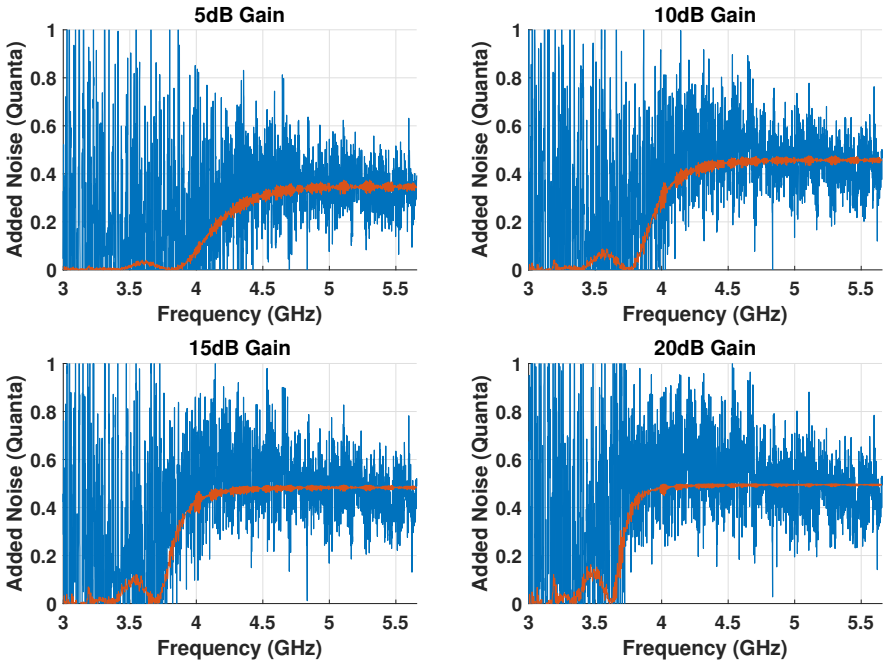

Figure 4.23: The measured added noise in units of quanta for the parametric amplifier operated as described in Figure 4.22 (blue) compared to the theoretical quantum limit (red).

that increases with the applied pump power. We are unsure as to the source of this excess noise, but it is consistent with a flat Johnson noise profile from a thermal effect.[101]

The source of the excess has proven extremely challenging to identify as the effect is not consistent and might change in strength across identical measurements taken over the span of several days. Even in the presence of this excess noise from an applied pump, however, the overall parametric amplifier added noise that we measure is consistently within 0.2 quanta of the quantum limit in our low-frequency three-wave-mixing designs.

4.5 Vacuum Squeezing

The analysis in section 2.4 on the quantum limits of added noise only considered phase insensitive amplifiers that amplify both I and Q quadratures of the signal equally. That condition is generally true for parametric amplifiers, with the notable exception of the degenerate point at the center of the three-wave-mixing gain where $\omega_s = \omega_i = \omega_p/2$ as can be readily seen from applying this condition to our previous analysis of noise limits.

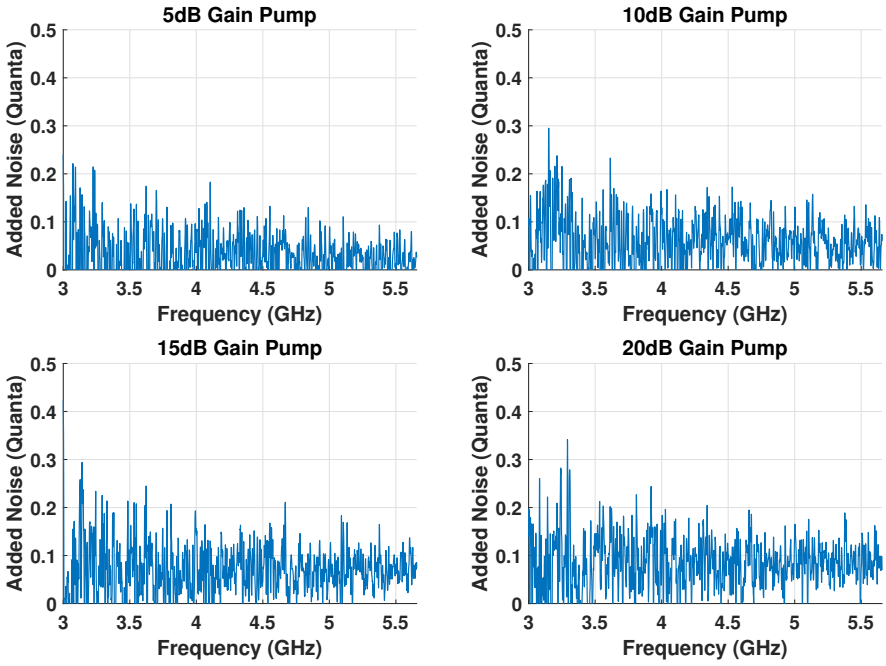

Figure 4.24: The measured added noise in units of quanta for the parametric amplifier operated as described in Figure 4.23 but without any applied I_{DC}.

In the degenerate case we no longer need to consider a second idler frequency, so the idealized operators for the output field reduce to

$$b_s = \mathcal{P}_{ss}\,(I_s + iQ_s) + C_{ss}\,(I_s - iQ_s) \tag{4.34}$$

or, alternatively

$$\begin{aligned} I_b &= (\mathcal{P}_{ss} + C_{ss})\, I_s \\ Q_b &= (\mathcal{P}_{ss} - C_{ss})\, Q_s \end{aligned} \tag{4.35}$$

where we recognize the quantities $G_I = (\mathcal{P}_{ss} + C_{ss})$ and $G_Q = (\mathcal{P}_{ss} - C_{ss})$ must be the linear gain for the I and Q quadratures by definition.

Similarly, the condition imposed by the general unitary condition in equation 2.63 reduces to

$$1 = \mathcal{P}_{ss}^2 - C_{ss}^2 \tag{4.36}$$

where we have chosen our input and output bases such that $\mathcal{P}_{ss}$ and C_{ss} are real. This implies that

$$1 = (\mathcal{P}_{ss} + C_{ss})(\mathcal{P}_{ss} - C_{ss}) \tag{4.37}$$

which combined with the above result requires

$$1 = G_I G_Q. \tag{4.38}$$

Therefore, the degenerate gain of a parametric amplifier must be not only phase sensitive but that the gain in one quadrature results in the inverse suppression of the other: $G_I = G_Q^{-1}$. Continuing the analysis of the added noise, we find that that the ideal degenerate amplification is noiseless,[43] which can be physically interpreted as resulting from the lack of an idler tone which was the source of the added noise in 2.89.

Our measurement scheme and analysis closely follows recent work on degenerate squeezing of parametric amplifiers at other institutions.[102] A schematic diagram of the measurement setup is shown in Figure 4.25. Using the same device in the previous section, we apply an an 11.313 GHz pump and measure the degenerate gain and squeezing of the $\omega_p/2$ frequency at 5.6565 GHz. Splitting the pump tone and using a multiplier allows us to keep a stable phase between the pump, mixer LO, and injected signal used to measure the gain. The I and Q plots read out using a lowpass filtered IQ mixer for various input signal phases are shown in Figure 4.26 with I and Q axes chosen to correspond with the amplified and squeezed quadratures. Fitting these data to calculate the ovals in the amplified and squeezed directions results in Figure 4.27, demonstrating perfect agreement with equation 4.38.

First, we perform a y-factor measurement to calibrate the added noise from all the components after the parametric amplifier, N_h. The output power for the 3.38 Kelvin and 20 mK load will be

$$\begin{aligned} P_{3.38K} &= (N_{3.38\mathrm{K}} + N_h)G_h \\ P_{20mK} &= (N_{20\mathrm{mK}} + N_h)G_h \end{aligned} \tag{4.39}$$

which can be solved for the gain

$$G_h = \frac{P_{3.38K} - P_{20mK}}{N_{3.38K} - N_{20mK}} \tag{4.40}$$

and noise

$$N_h = \frac{1}{G_h}\left(\frac{N_{3.38K}P_{20mK} - N_{20mK}P_{3.38K}}{N_{3.38K} - N_{20mK}}\right). \tag{4.41}$$

This noise can then be propagated to calculate the system noise referred to the input of the parametric amplifier though

$$N_{\mathrm{sys}} = N_{\mathrm{pa}} + \frac{N_h}{G_{\mathrm{pa}}} \tag{4.42}$$

where G_{pa} and N_{pa} are the parametric amplifier's gain and added noise. Assuming this noise is dominated by the parametric amplifier and HEMT, we can express the

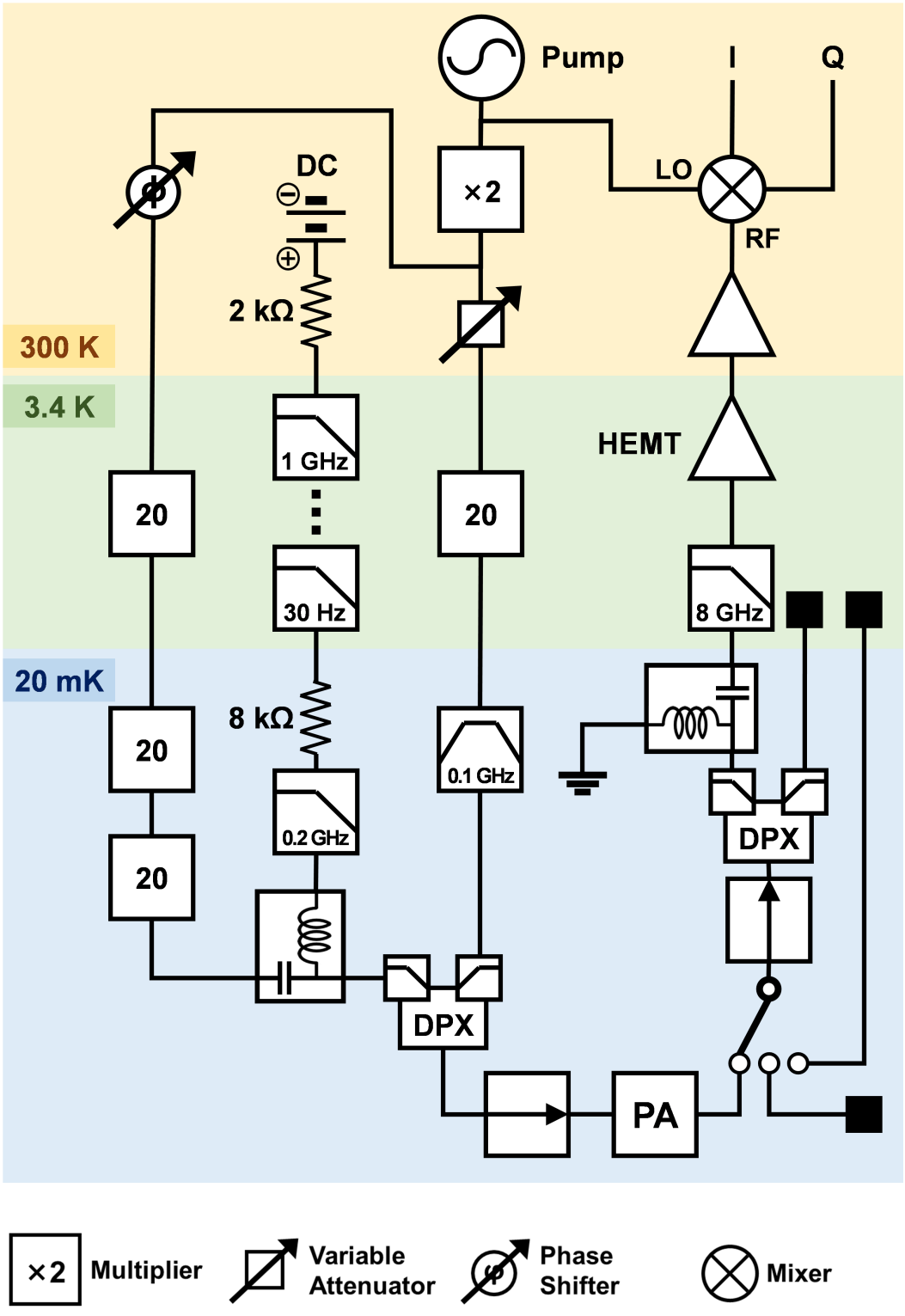

Figure 4.25: A schematic diagram of our degenerate squeezing setup. A single synthesizer supports the pump, mixer LO, and signal input to maintain phase stability between those channels. Refer to Figure 4.17 for complete legend of components.

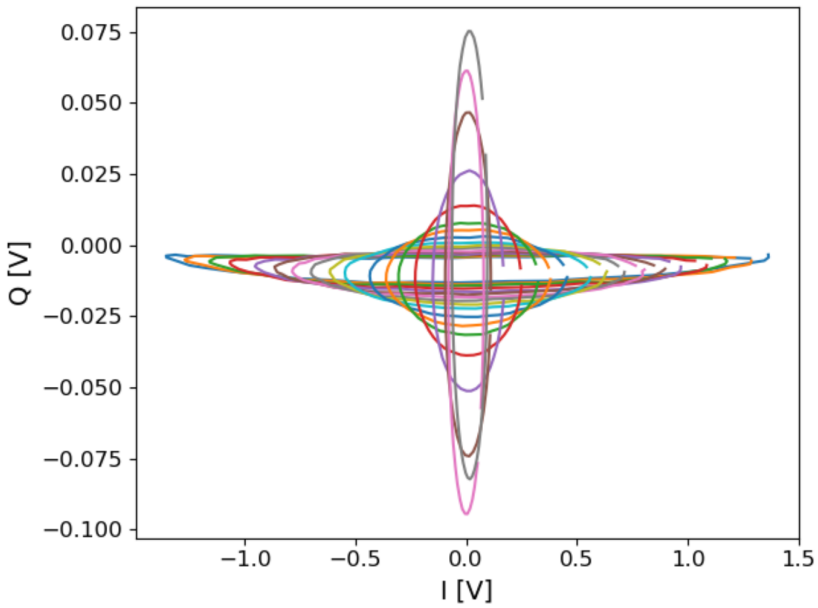

Figure 4.26: The I and Q outputs of the IDC for different phases of the input signal at $\omega_p/2$. Note the scale Q axis has been magnified to better show the squeezed quadrature. Each curve corresponds to a different level of pump power, ranging from the parametric amplifier off to maximum gain.

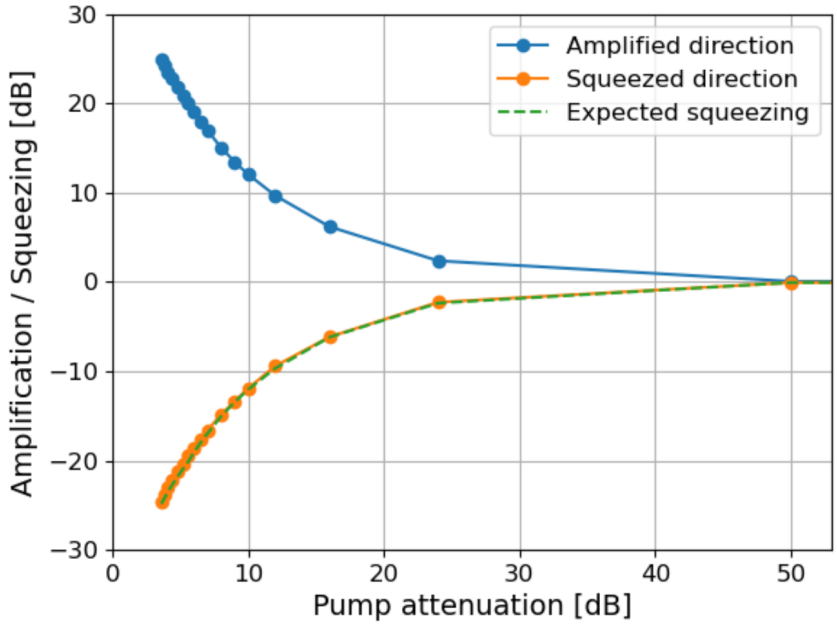

Figure 4.27: The gain and squeezing level of the amplified (blue) and squeezed (orange) quadratures for different levels of pump power (expressed in terms of its attenuation). The green curve corresponds to the expected squeezing level according to equation 4.38 from the amplified direction.

output noise in the amplified and squeezed quadratures more explicitly as

$$\begin{aligned} N_{\text{amp}} &= \left[\left(N_{\text{mk}} + N_{\text{pa}} \right) G_{\text{pa}} A_{\text{loss}} + N_{\text{mk}} (1 - A_{\text{loss}}) + N_{\text{HEMT}} \right] G_{\text{post}} \\ N_{\text{sq}} &= \left[\left(\frac{N_{\text{mk}}}{G_{\text{sq}}} + N_{\text{pa}} \right) A_{\text{loss}} + N_{\text{mk}} (1 - A_{\text{loss}}) + N_{\text{HEMT}} \right] G_{\text{post}} \end{aligned} \tag{4.43}$$

where G_{post} is the combination of the gain and attenuation of the HEMT and subsequent readout system, A_{loss} is the attenuation between the parametric amplifier and HEMT, and G_{pa} / G_{sq} are the amplified and squeezed quadrature gain. Measuring these quantities by taking the power spectral density of the I and Q data streams, we calculate the system noise in the amplified quadrature.[103] The result is shown in Figure 4.28, demonstrating a system noise that falls below the vacuum noise level for high parametric amplifier gain. While this process could in principle be noiseless, the data are best explained with a parametric amplifier added noise of $N_{\text{pa}} = 0.25$ quanta, perhaps caused by the same transient, unexplained process as discussed in the previous section.

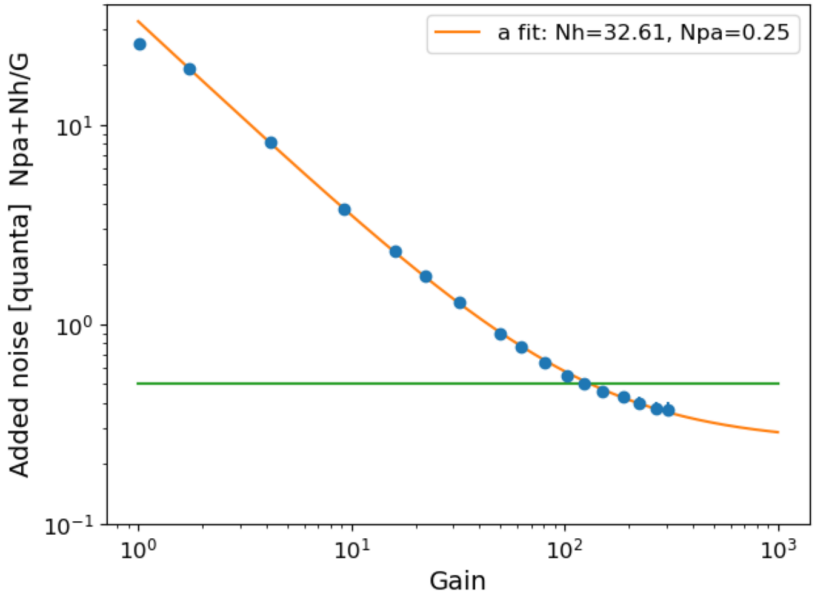

Figure 4.28: The system noise in units of quanta of the amplified quadrature (blue) plotted with respect to the parametric amplifier gain. The modelled fit for N_h and N_{pa} is shown in orange, while the half-photon zero point vacuum fluctuations are plotted in green. At high gains, the system noise falls below the vacuum fluctuations, but is ultimately limited by the $N_{\text{pa}} = 0.25$ quanta noise.

In the squeezed quadrature, we see a small fractional reduction of noise with the parametric amplifier turned on compared to that from the vacuum-noise-level 20

mK input. This squeezing level is given by the radio of the noise with the amplifier on and of

$$\text{Squeezing Level} = 1 - \frac{\left(\frac{N_{\text{mk}}}{G_{\text{sq}}} + N_{\text{pa}}\right) A_{\text{loss}} + N_{\text{mk}}(1 - A_{\text{loss}}) + N_{\text{HEMT}}}{N_{\text{mk}} + N_{\text{HEMT}}} \tag{4.44}$$

and was measured to be a maximum of roughly 1.3% as shown in Figure 4.29, a reduction in noise that definitively indicates some level of vacuum noise squeezing.

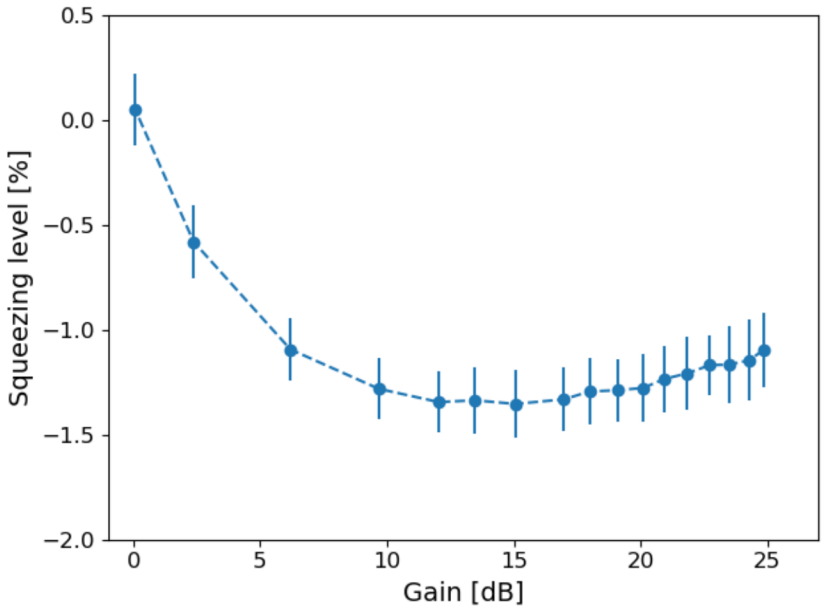

Figure 4.29: The squeezing level defined by the ratio of the system noise measured relative to the amplifier off case plotted against the gain in the amplified quadrature.

Using the above expression and our y-factor measurement, we can factor out the other contributions to the noise and solve for the single unknown parameter, G_{sq}, corresponding to the degree of vacuum squeezing. The result of this calculation is shown in Figure 4.30, indicating a nearly 10 dB level of reduction in vacuum noise in the squeezed quadrature at the parametric amplifier output. For an ideal device, the degree of vacuum noise squeezing should be perfectly linear with the amplified quadrature gain (see equation 4.38), and asymptotic behavior to a minimum squeezed value is indicative of some amount of added noise in the device that limits the squeezing level. The level of added noise indicated by this data corresponds to 0.13 quanta, which is unsurprising given that we have seen hints of excess noise on that scale from an applied pump with our system (see Figure 4.24).

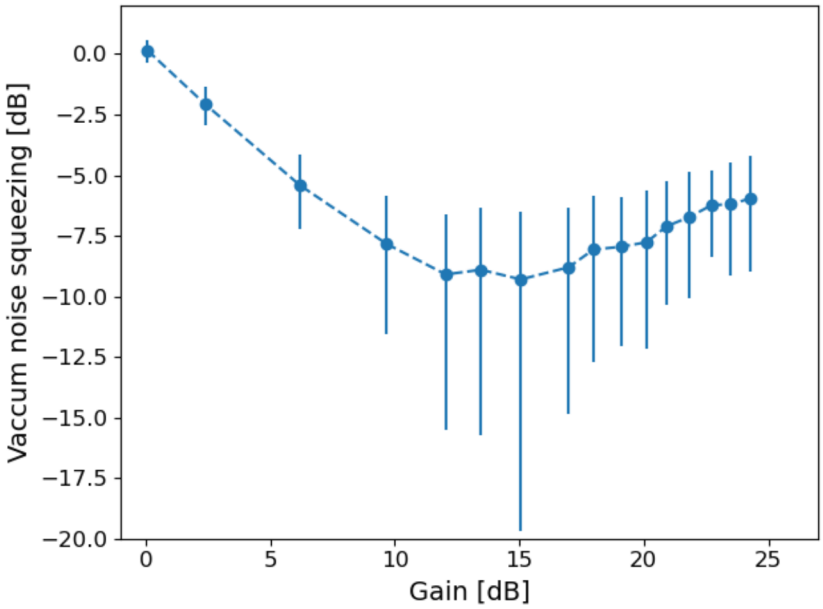

Figure 4.30: A plot of the level of vacuum squeezing $1/G_{\mathrm{sq}}$ calculated from the data shown in Figure 4.29. The result shows a maximum squeezing level of -9.3 dB when the amplified quadrature has 15 dB gain.

These results indicate that the parametric amplification process occurring in our devices is acting in a nearly ideal manner, with minimal effects from excess noise.[104]

Chapter 5

OTHER EXPERIMENTS

5.1 Loss Measurement

All of our parametric amplifiers over the past several years have been designed with a uniform basis for the microstrip line: a 250 nm wide, 35 nm thick NbTiN layer deposited on a Silicon substrate separated from the ground plane by a layer of amorphous Silicon. Because the central conductor and adjacent materials remain identical across our device, we can accurately estimate the loss across all of our devices through a careful measurement of a single similar test structure.

We accomplish this by fabricating an on-chip Fabry-Pérot interferometer centered at 8.3 GHz consisting of a 93 mm transmission line in between two Bragg reflectors.[64] The device, shown in Fig. 5.1, acts as an etalon for frequencies within the stop band. This creates transmission peaks in the S_{21} at frequencies

$$\omega_n = \frac{n\pi v_{\text{ph}}}{L} \tag{5.1}$$

where L is the distance between the reflectors.[64] From the measured frequency spacing in Figure 5.1 (c), we find that $v_{\text{ph}} = 0.0077c$, in perfect agreement with the value measured in our low-frequency parametric amplifiers. The transmission of the etalon may be expressed as

$$S_{21} = \frac{t^2 e^{-\gamma L}}{1 - r^2 e^{-2\gamma L}}, \tag{5.2}$$

where t and r are the frequency dependent Bragg reflector transmission and reflection amplitudes and γ is the propagation constant on the internal transmission line section as given in 3.29. Near the resonance frequencies, ω_n, the transmission peaks are nearly Lorentzian and follow

$$S_{21}(\omega_n + \delta\omega) \approx \frac{Q_r}{Q_c} \frac{t^2}{1 - r^2} \frac{e^{-\gamma L}}{1 - 2iQ_r\delta\omega/\omega_n}, \tag{5.3}$$

for some small $\delta\omega$ where Q_r is quality factor measured by the full width half maximum of the resonance and can be decomposed into the quality factor from the internal losses, Q_i, and from the coupling, Q_c, via

$$Q_r^{-1} = Q_c^{-1} + Q_i^{-1}. \tag{5.4}$$

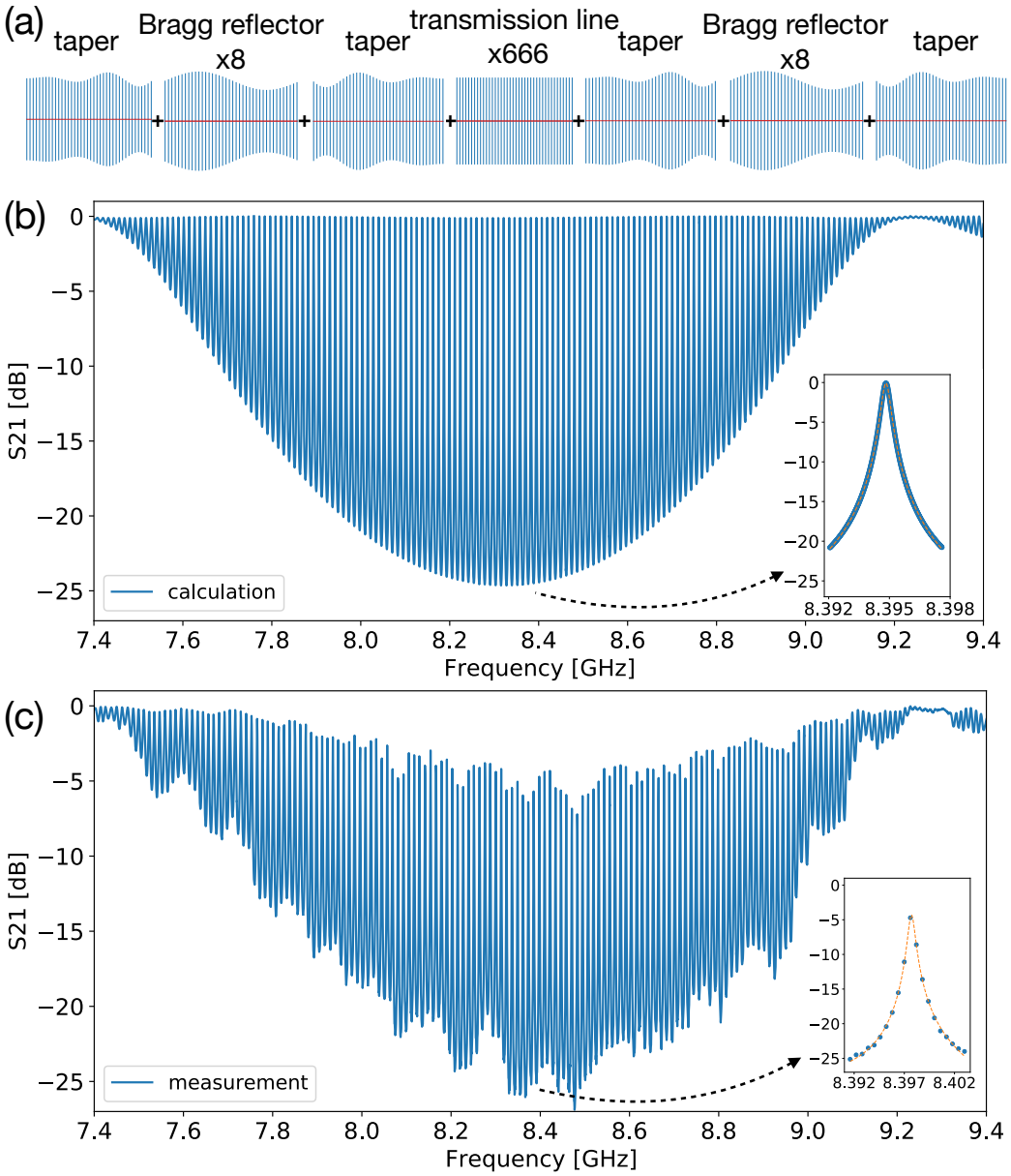

Figure 5.1: (a) The schematic structure of the on-chip Fabry-Pérot interferometer. The capacitive fingers have an average length of 26 μm spaced 2 μm apart and are sinusoidally modulated with an amplitude of 12 μm and periodicity 140 μm for a total of 8 periods to form the Bragg reflectors, and this modulation is then tapered across 2 periods to decrease the impedance mismatch with the transmission line. (b) The calculated S_{21} according to the method in section 3.1. (c) The measured S_{21} at 1 K with baseline loss removed from fitting the higher/lower frequencies.[64]

We can further express these two individual quality factors as

$$Q_c = \frac{\omega_n L}{v_{\text{ph}}} \frac{r^2}{1 - r^2} \tag{5.5}$$

and

$$Q_i = \frac{\beta}{2\alpha} \tag{5.6}$$

where α and β are the real and imaginary components of $\gamma = \alpha + i\beta$. Neglecting loss in the Bragg reflectors by taking

$$r^2 + t^2 = 1 \tag{5.7}$$

and normalizing the transmission to that of a single pass through the internal transmission line section (dividing by $e^{-\gamma L}$), the above expression reduces to simply

$$S_{21} \approx \frac{Q_r}{Q_c} \frac{1}{1 - 2iQ_r \delta\omega/\omega_n}. \tag{5.8}$$

The S_{21} transmission of the device was measured in a setup similar to Figure 4.6 at 1 K without the unnecessary pump channel and directional coupler. The result, shown in Figure 5.1, has great agreement with the theoretical prediction.

We then extracted Q_i using two different methods. In the first "circuit model method," we apply the lossless circuit model used to obtain the predicted S_{21} in Figure 5.1 (b) to extract Q_c according to equation 5.8 (nothing that in the lossless calculation, $Q_r = Q_c$). With this calculated value of Q_c at hand, we fit our measured S_{21} data to extract Q_i. In the second "resonance height method," we instead note that the maximum resonance height

$$\max(|S_{21}|) = \frac{Q_r}{Q_c} \tag{5.9}$$

which when combined with equation 5.4 can be solved for

$$Q_i = \frac{Q_r}{1 - \max(|S_{21}|)} \tag{5.10}$$

using the measured S_{21} and fitting the full width half maximum of each resonator for Q_r. We only perform this analysis for resonances near the center of the stop band because the higher Q_c makes them more sensitive to changes in Q_i. The results of both of these calculations are shown in Figure 5.2 (a).

The large variance and slope of the circuit model calculation suggests that the coupling quality factors, Q_c, deviate from the idealized values in our model. At 8.4

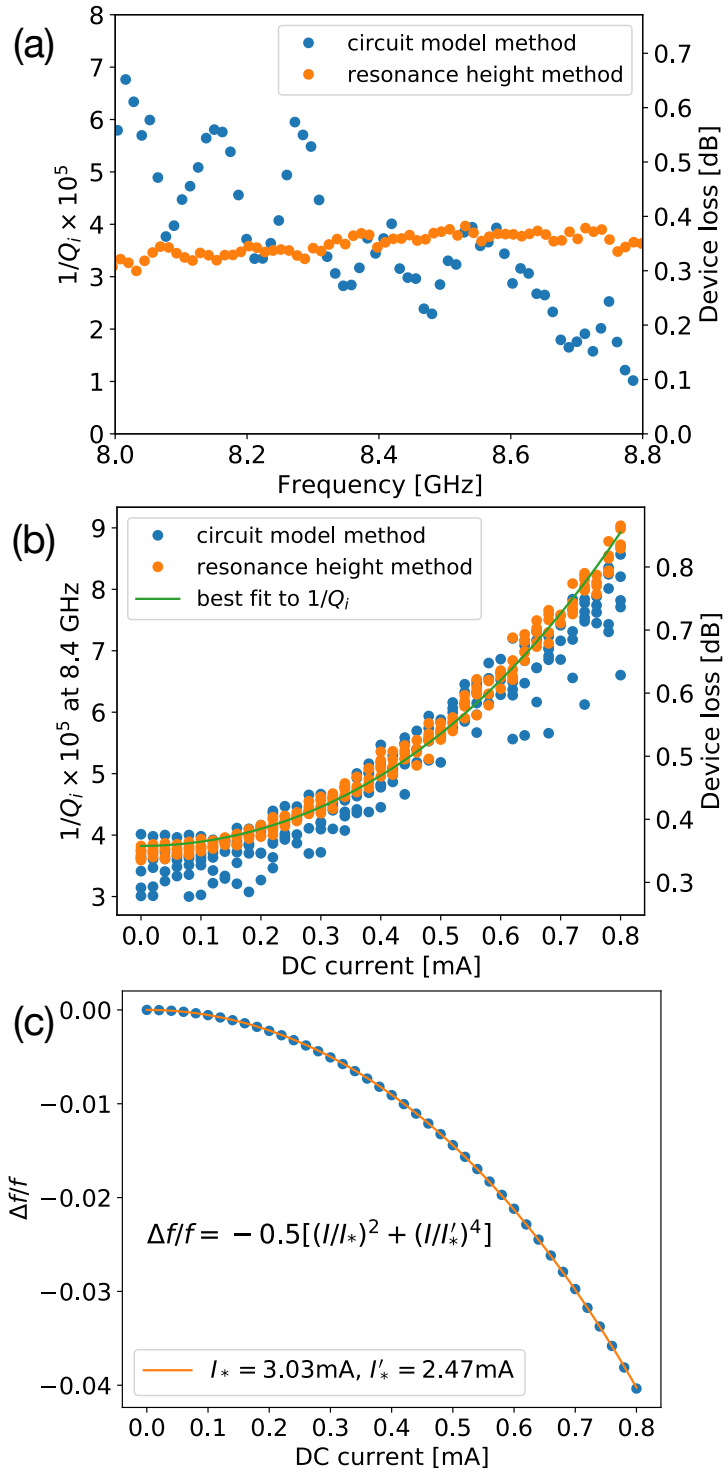

Figure 5.2: (a) The frequency dependent attenuation factor when $I_{DC} = 0$. (b) Quality factor and corresponding attenuation as a function of current. The device loss for a one-way parametric amplifier with the same 93 mm length. (c) The frequency shift of a single resonance by increasing DC current and corresponding extracted nonlinearity scale factors. [64]

GHz where the two methods give consistent results, we obtain an $\alpha = 3.7$ dB/m and $Q_i = 2.8 * 10^4$. This result is lower than the $Q_i > 10^5$ than has been observed in resonators using an identical amorphous Silicon dielectric,[79] indicating that some of the losses may result from the NbTiN film itself.

Repeating the measurements across a range of applied DC currents reveals a degradation in the quality factor at high currents (Figure 5.2 (b)) and measured frequency shift of the resonators due to the change in v_{ph} (Figure 5.2 (c)). While the latter result provides an excellent measure of I_* and I'_* for our gain calculations, the source of of the increased attenuation at higher currents is unclear. The temperature dependent loss (previously shown in Figure 4.15) for NbTiN is too small near 1 K to account for heating effects to account for the three-fold increase in attenuation. Furthermore, a calculation of Q_i using the Usadel and Nam's equations remains above 10^8 for the highest current we applied, so it is not explained by the changing density of states.[105, 106, 107, 108] One potential explanation is the presence of magnetic fields perpendicular to the microstrip, where a 3 mT field has been reported to degrate Q_i in NbTiN resonators from 10^5 to 10^3.[109] The magnetic field generated from our DC current is 0.84 mT, and the geometry of the meandering microstrip and induced ground plane currents may yield a similar, smaller effect that we see in our measurements. Further experiments are needed to confirm or refute this hypothesis.

5.2 K_a band Amplifier

At frequencies higher than 20 GHz, our general device structure and housing needs to be adjusted to ensure that the box-modes formed by the channel between the conducting sky plane and device housing remain outside the working frequency range. Figure 5.3 shows the reduced chip size and housing this for one of our devices designed to produce three-wave-mixing gain in the K_a band from 24.5 to 40 GHz.[110] This frequency range was chosen due to the potential relevance for downlink communication from the Deep Space Network. [111]

The amplifier is fabricated on a thin, 100 μm Silicon substrate, maintaining our usual dimensions of 250 nm wide 35 nm thick NbTiN central conducting layer. Impedance matching is obtained by capacitive fingers averaging 3 μm in length and otherwise identical dimensions, which are then modulated with an amplitude of 0.2 μm and period 38.25 μm to produce a band gap at 38.5 GHz.

The gain of the amplifier is measured using the standard setup shown in Figure 4.6 where the individual components used have designed operating frequencies up to

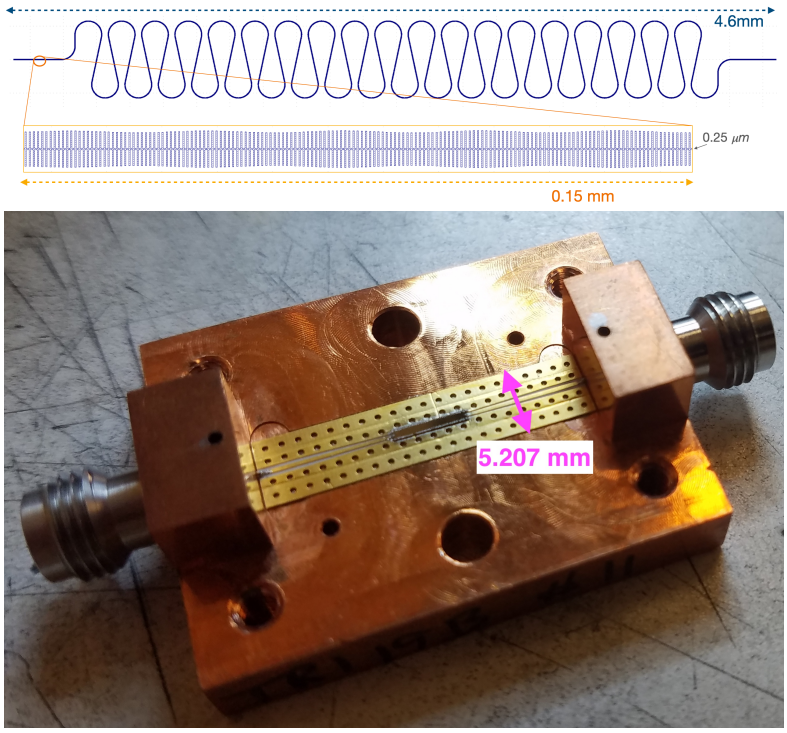

Figure 5.3: A schematic diagram of our Ka-band parametric amplifier (top) and photo of the device in its housing (bottom). The microstrip is arranged in a meandering path that extends the physical dimension of 4.6 mm to a total device length of 21 mm. The zoom-in shows the capacitive fingers and their modulation to produce the photonic band gap.[64]

65 GHz. The resulting gain measured at 1 K is shown in Figure 5.4 and does not include the expected 0.01 dB/GHz loss of the device. While this device does not obtain the level of gain seen in some of our lower-frequency amplifiers, it produces a significant amount of gain across over three octaves of bandwidth, spanning from 4 to 34 GHz.[64]

5.3 W-band Amplifier

Beyond the Ka band devices, we have also developed an initial prototype for even higher frequency parametric amplifiers,[112] operating in the W-band motivated by the need for high frequency readout electronics with lower noise figures for radio telescopes at those frequencies.[113] In particular, the proposed amplifier technologies for the Atacama Large Millimeter/submillimeter Array (ALMA) band 3 receivers only obtain noise temperatures on the order of 24 Kelvin, roughly 10 times higher than the quantum limit at those frequencies.[114]

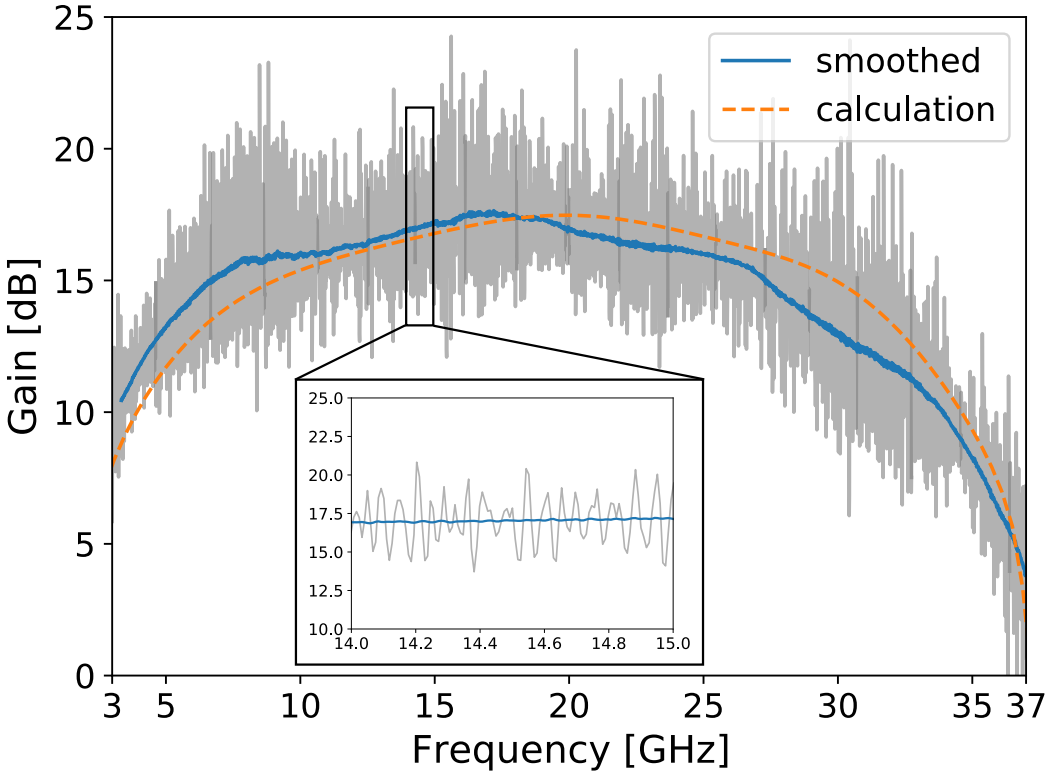

Figure 5.4: Three-wave mixing gain of the parametric amplifier gain measured at 1 K with a -29.3 dBm pump tone at 38.8 GHz and I_{DC} = 0.75 mA. The gray curve shows the raw data as measured by the VNA, while the blue curve is the smoothed over frequency and the inset shows the gain ripple in more detail. The orange curve shows the coupled mode calculation for the expected performance.[64]

Our measurement system for W band parametric amplifiers is housed in a separate cryostat complete with WR-10 waveguide components that allow for measurements from 75 to 110 GHz.[115] The schematic diagram for our W-band noise and gain measurement setup is shown in Figure 5.5. The system design follows the same motivations outlined for our low-frequency amplifiers, with a few alterations given the availability of certain components at these higher frequencies.

Unlike our low-frequency setup where the base temperature required was on the order of tens of milliKelvins, the cold stage is cooled by a Chase Research Cryogenics single-stage ^{4}He cooler (#CRC4-014) which allows for a base temperature of almost exactly 1 Kelvin. We are able to operate at this relatively high temperature while retaining sensitivity to quantum-limited noise due to the scaling of noise quanta with temperature as given in equation 4.28. Operating at such a high temperature for a 5 GHz amplifier would introduce roughly 4 quanta of input noise. In contrast,

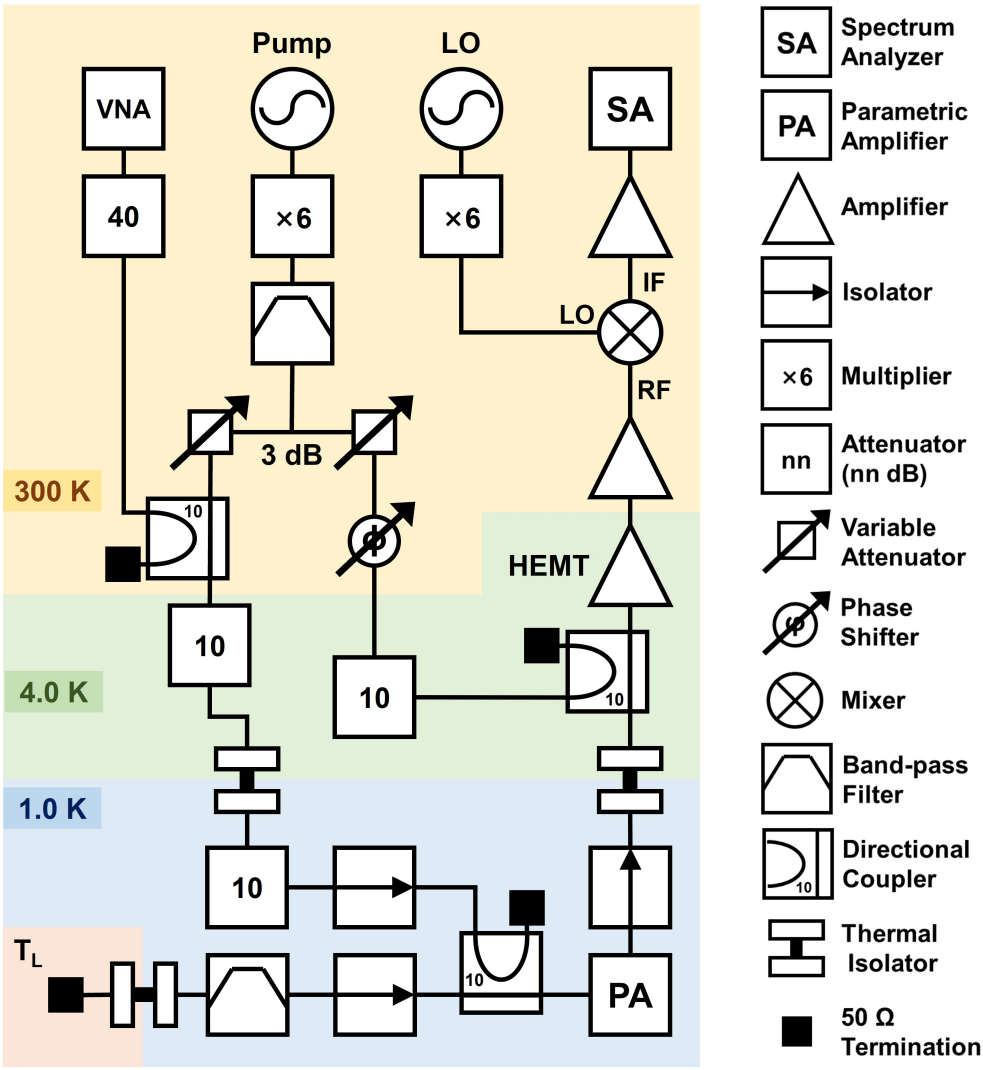

Figure 5.5: Schematic diagram of our noise measurement setup for W band parametric amplifiers.

a 1 K load produces less than 0.02 quanta of noise beyond the quantum limit in the W-band, well below the expected measurement sensitivity. By a similar argument, less attenuation is needed along the input line as the room temperature noise does not need to be reduced significantly below the sub-Kelvin level. These two decisions in turn allow us to combine the pump and signal channels outside the cryostat as the resulting heat dissipation does not exceed our cooling power at these higher temperatures.

Because we do not have access to a W-band VNA, synthesizer, or spectrum analyzer, we instead up and down convert our signals using multipliers and mixers. The C4220 VNA output is up-converted using a VNAX-816 frequency extender, while the

parametric amplifier pump and local oscillator for the mixer are supplied using low frequency synthesizers and QMC-MX6-10F10 multipliers.[116] These multipliers generate a large amount of excess noise that is insufficiently attenuated by the input line, so we further filter it using a QMC-BPF10-9204 band-pass filter (90 to 94 GHz),[117] which excludes those frequencies from our noise measurement range. Unfortunately, our four-wave-mixing parametric amplifier requires a 90 GHz pump, meaning we also see this excess noise in the corresponding 4 GHz idler bandwidth from 86 to 90 GHz. Because the band-pass filter does not cutoff immediately, we can only attempt a noise measurement at frequencies outside of the 85 to 95 GHz range for this device.

The signal after the parametric amplifier is read out using an SM200A spectrum analyzer [98] after it has been amplified in the W-band using a HEMT and SAGE Millimeter Low Noise Amplifier (providing 20 dB gain and 5 dB noise figure),[118] mixed to a lower frequency, and further amplified by a ZVA-183-S+ RF amplifier.[97] The HEMT we use in this experiment is a prototype built at JPL that provides over 20 dB gain with approximately 27 K noise temperature within our measurement frequency range.[119] The pump necessary for the parametric amplifier would saturate the HEMT and there are no commercially available diplexers for these frequencies for separating it from the signal. To lower the power supplied to the HEMT, we separate the pump tone using a 3 dB splitter and recombine it using a directional coupler with amplitude and phase tuned to cancel the pump tone from the parametric amplifier. For an unknown reason, the cancellation is not perfectly stable and requires minor re-tuning of the amplitude and phase on the time scale of several minutes to an hour.

The device itself uses our standard microstrip geometry, with a 320 nm wide and 35 nm thick NbTiN superconducting layer that has 7 mm total length. The capacitive fingers have similar dimensions with an average of 2.85 μm length that is modulated with an amplitude of 0.1 μm and 16 μm period to create a band gap slightly above 90 GHz. The gain obtained by this device relative to the 1 K transmission with the pump off is shown in Figure 5.6. Note that this device is our first iteration of a W-band amplifier, so it has not undergone the series of revisions and edits to the design that resulted in the gain curves shown in the previous chapter.

Within our final noise-measurement setup, the gain obtained from this amplifier within the measured frequency range is shown in Figure 5.7, demonstrating roughly 15 dB gain over a broad bandwidth. In this operating condition, we performed a

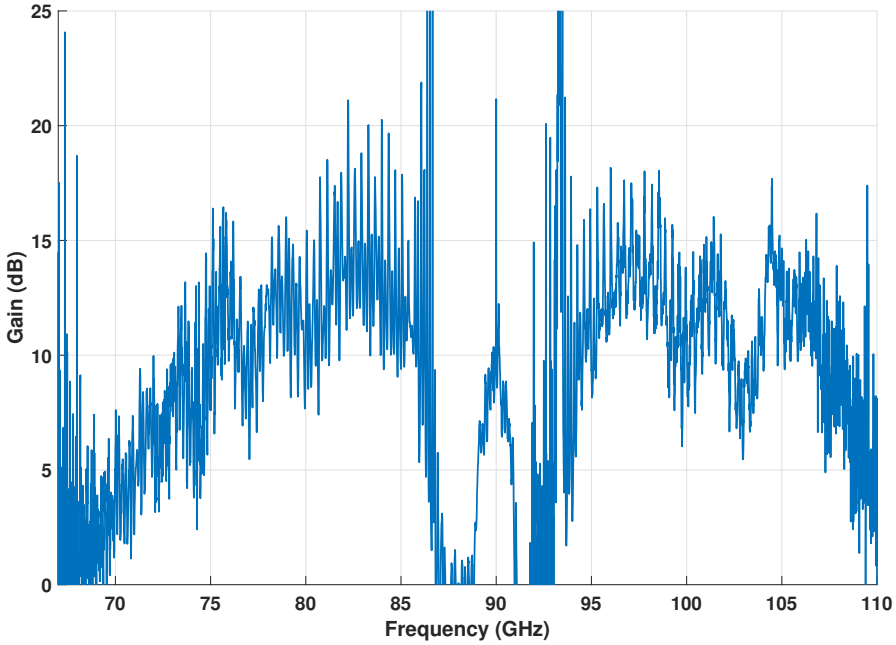

Figure 5.6: Gain relative to pump off transmission of our W-band parametric amplifier with a 90 GHz pump as measured in our initial device screening.

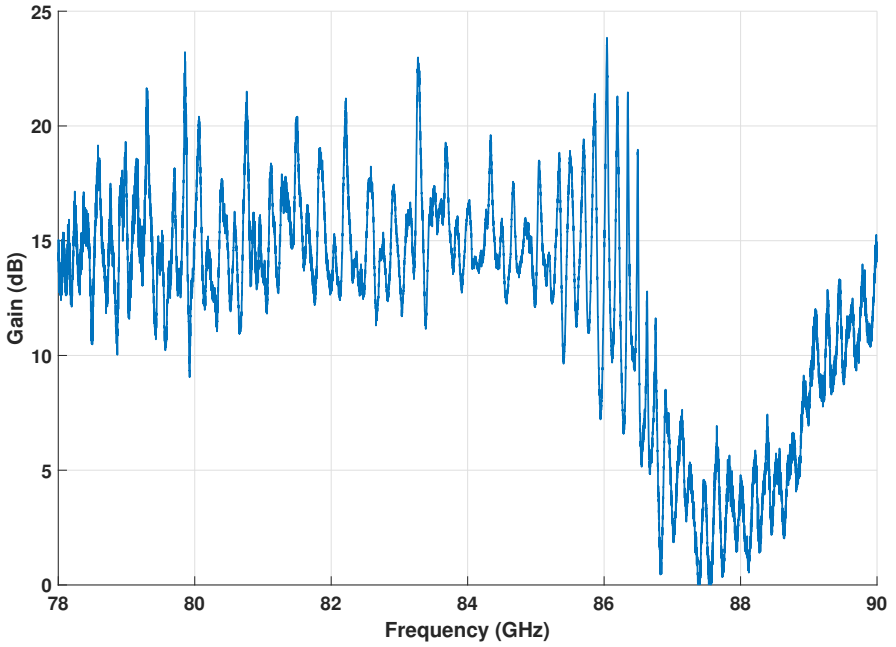

Figure 5.7: Gain relative to pump off transmission of our W-band parametric amplifier with a 90 GHz pump during the noise measurement.

standard y-factor measurement to characterize the system and amplifier noise by varying the temperature of the load at the input of the parametric amplifier. Note that we have inserted a band-pass filter (bandwidth from 79 to 87 GHz) that limits the frequency range affected by this input noise. This ensures that the parametric amplifier added noise remains constant due to the identical idler input noise and allows us to calibrate out any drifts in the system using the stable baseline outside of that frequency range. The spectrum analyzer response relative to the output at the base temperature is shown in Figure 5.8.

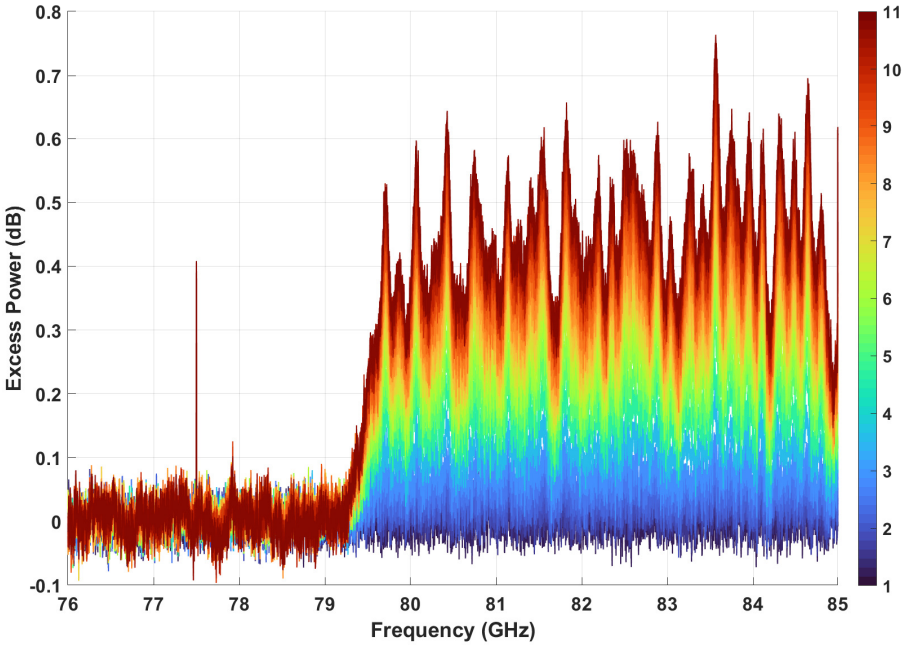

Figure 5.8: Excess noise as measured by the spectrum analyzer at various load temperatures from 1 to 11 K. Due to the band-pass filter, the power only changes above 79 GHz. The system drift over the course of these measurements (less than 0.1 dB) is removed by enforcing a consistent baseline near 76 GHz.

Assuming the variable temperature load is well-impedance matched, at $T = T_L$ it will have a noise output per unit bandwidth of

$$N_L(\nu, T) = \frac{1}{2} \coth \frac{h\nu}{2kT} \tag{5.11}$$

in units of quanta.[71] Due to the attenuation between the load and the amplifier, given by $S_{21}(\nu)$, the number of noise quanta per unit bandwidth at the amplifier's input will be

$$N_{\text{in}}(\nu, T_L) = N_L S_{21}(\nu, T_L) + N_S(\nu, T_S)(1 - S_{21}(\nu)) \tag{5.12}$$

where N_S is given by equation 5.11 calculated at the base temperature $T_S = 1$ K. The S_{21} of the relevant components was measured at a similar temperature in a series of subsequent cooldowns. The power measured by the spectrum analyzer per unit bandwidth will be

$$P(\nu, T_L) = G_{\text{sys}}(\nu)[N_{\text{in}}(\nu, T_L) + N_{\text{sys}}(\nu)] \tag{5.13}$$

where $G_{\text{sys}}(\nu)$ is the system gain and N_{sys} is the total system noise in units of quanta. In this linearized form, the system noise is given by the negative y-intercept of $P(T_L)$. Taking two measurements of the spectrum analyzer output for a cold ($T_L = T_C$) and hot ($T_L = T_H$) load, we can calculate this intercept to be

$$N_{\text{sys}}(\nu) = P(\nu, T_H)\frac{P_H(\nu, T_H) - P_C(\nu, T_H)}{N_H(\nu) - N_C(\nu)} - N_C(\nu). \tag{5.14}$$

If the system noise is dominated by the parametric amplifier and HEMT noise, this quantity will equal

$$N_{\text{sys}}(\nu) = N_{PA}(\nu) + \frac{N_{\text{HEMT}}(\nu)}{G_{PA}(\nu)|S_{21}(\nu)|^2} \tag{5.15}$$

where $S_{21}(\nu)$ is the attenuation between the parametric amplifier and HEMT, G_{PA} and N_{PA} are the parametric amplifier gain and noise, and N_{HEMT} is the HEMT added noise in units of quanta.

The result of this calculation is shown in Figure 5.9. A quick calculation shows that this noise exceeds the noise temperature of the HEMT at ∼7 quanta. A careful investigation showed that the cause is an extremely low transmission of 0.1 through the parametric amplifier and its housing.

Other such devices in identical housing (shown in Figure 5.10) have shown transmission ratios of 0.5, which combined with our loss measurements make it unlikely that the poor transmission of our amplifier is primarily due to loss mechanisms within the device instead. Our current hypothesis is that the device was mounted off-center, reducing the coupling coefficient between the signal and waveguide probe at the input and output of the amplifier.

The overall added noise of our parametric amplifier and measurement system is highly dependent on how this coupling and loss that results in poor transmission is distributed. For example, if the attenuation occurred entirely before the parametric amplifier, this would effectively reduce the load temperature T_L as seen by the device according to equation 5.12. In that limit, the overall system noise reduces to the

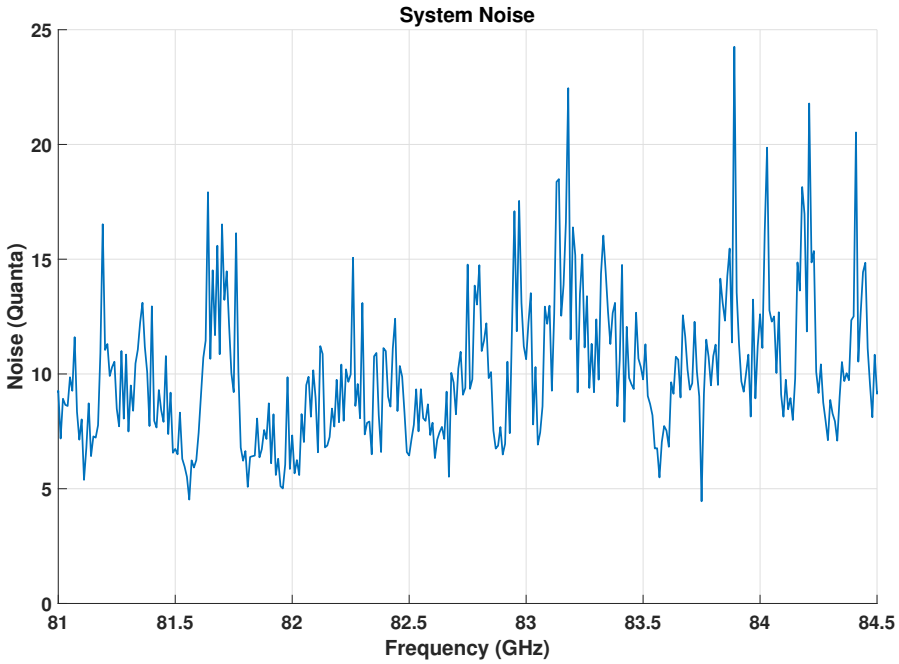

Figure 5.9: The system noise per unit bandwidth in units of quanta for our W-band noise measurement setup with the parametric amplifier on.

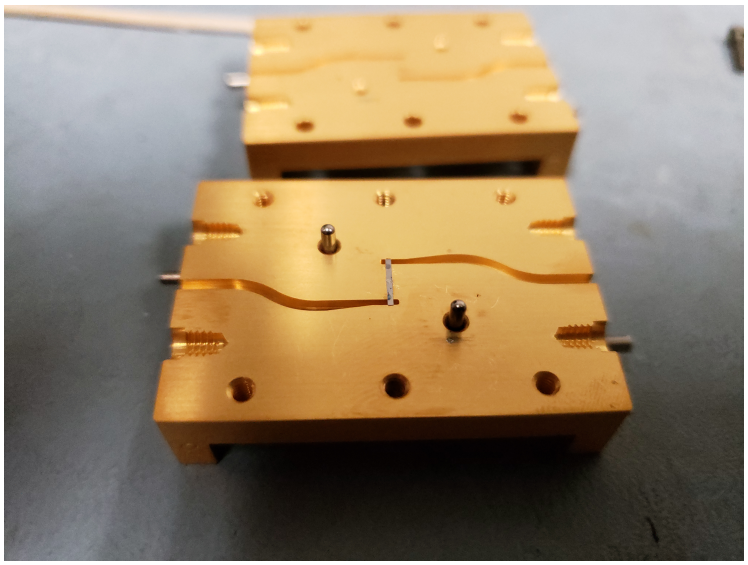

Figure 5.10: A photograph of the housing for our W-band device. The amplifier is secured upside down with silver epoxy to create a connection between the sky plane and ground.

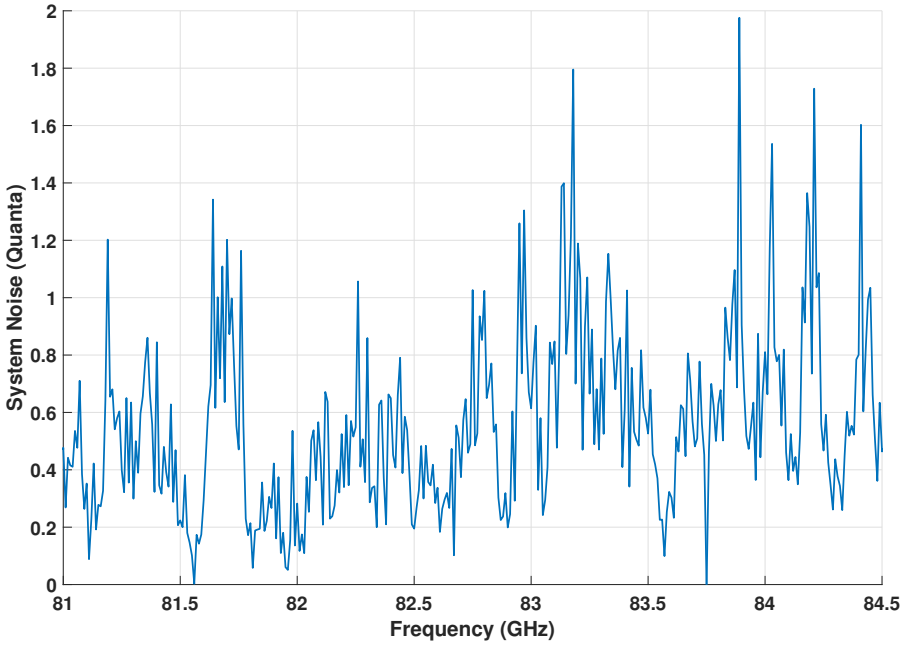

Figure 5.11: The system noise per unit bandwidth in units of quanta for our W-band noise measurement setup with the parametric amplifier on if we assume a 0.1 excess transmission between the temperature load and parametric amplifier.

graph shown in Figure 5.11, giving a noise figure that is unphysically low. On the other hand, if this poor transmission instead occurred entirely within or after the amplifier, we would recover the original system noise as shown in Figure 5.9.

Assuming our hypothesis is correct that the off-centered mounting results in a poor coupling coefficient from the microstrip to waveguide, the overall system noise would fall somewhere in between these two results. A thorough investigation either by careful replication of the experiment with the parametric amplifier housing forward and backwards direction reversed could in principle allow us to calibrate out this transmission effect to calculate the inherent noise of the parametric amplifier itself. However, such a device would only provide a practical 5 dB gain given the housing losses, making it wholly unsuitable for any applications.

There is no non-destructive method of adjusting the device positioning within the housing because this device is fabricated on an extremely thin 100 μm thick substrate and firmly secured with silver epoxy. Furthermore, the duplicate copies of this design have had very low yield in terms of performance with only this chip showing gain in excess of 10 dB, so we do not have an alternative W-band amplifier to replace this

device. While further results will likely have to wait for a newly fabricated wafer, this creates a potential opportunity to further improve on W-band device performance by applying what we have learned in the three years since the development of this original design.

5.4 Frequency Converter

As discussed in section 4.2, we see a large amount of deamplification due to frequency conversion processes when we apply a pump far below the designed frequency range of our devices. These processes are generally interesting to spectroscopic measurements operating in the 100 GHz to several THz regime such as the Herschel-Heretodyne Instrument for the Far-Infrared which require a large number of frequency multipliers driven by a local oscillator.[120] The current state of the art for such multipliers are both relatively bulky and consume many μW or even milliWatts of power for conversion efficiencies far below unity, far from ideal for space missions. Conversely, radio telescopes such as the Atacama Large Millimeter/submillimeter Array (ALMA) use an enormous number of mixers to amplify and down-convert their signal for readout and could also make use of a more compact, lower power, higher-efficiency solution.[113]

Our investigation of these effects has focuses largely on the process $\omega_s + 2\omega_p = \omega_i$ where a signal photon combines with two pump photons to produce a much higher frequency up-converted signal. The coupled-mode equations corresponding to this process are

$$\begin{aligned}
\frac{\partial I_p}{\partial z} &= \frac{ik_p}{8I_*^2}\left[2I_i I_s^* I_p^* e^{i\Delta\beta z} + \left(|I_p|^2 + 2|I_s|^2 + 2|I_i|^2\right) I_p\right] \\
\frac{\partial I_s}{\partial z} &= \frac{ik_s}{8I_*^2}\left[I_i I_p^* I_p^* e^{-i\Delta\beta z} + \left(|I_s|^2 + 2|I_p|^2 + 2|I_i|^2\right) I_s\right] \\
\frac{\partial I_i}{\partial z} &= \frac{ik_i}{8I_*^2}\left[I_p^2 I_s e^{-i\Delta\beta z} + \left(|I_i|^2 + 2|I_p|^2 + 2|I_i|^2\right) I_i\right]
\end{aligned} \tag{5.16}$$

where

$$\Delta\beta = k_i - k_s - 2k_p. \tag{5.17}$$

We choose to investigate this up-conversion mechanism in particular as the design of our three-wave-mixing parametric amplifiers regularly results in very efficient conversion fractions. The engineered band gap introduced for adjusting the dispersion at the pump frequency in the parametric amplifier process serves the same effect for the up-converted idler tone when the pump is placed far below the band gap. This

enables perfect phase matching between some choice of low-frequency signal and pump frequency to an output just above the photonic band gap.

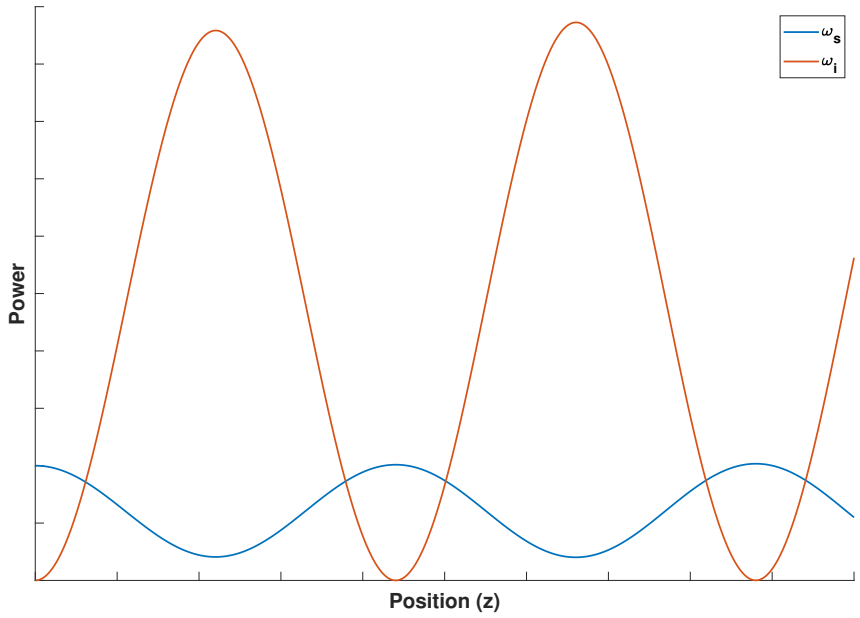

Figure 5.12: A model plot of the signal (blue) and up-converted idler (red) powers for a dispersionless microstrip as they travel through the device. Power oscillates between the two frequencies reaching a maximum photon-conversion efficiency of 80%. The idler tone power exceeds the input signal due to the higher energy carried by each individual up-converted photon. An identical plot can be produced by plotting the output for some chosen z with respect the input pump power, $|I_p|^2$.

A computational solution of the above equations for a simple dispersionless device shows that the power oscillates between the original low-frequency signal and up-converted output (see Figure 5.12). The size and periodicity of this oscillation is determined by both the dispersion criterion and pump power. Adjusting the pump power simultaneously tunes both of these parameters through modifying the pump self-phase modulation that sets the optimal dispersion between the three tones, meaning we can in principle tune a device to perform this up-conversion with arbitrarily high efficiency given it has sufficient length and nonlinearity in the kinetic inductance.

One particular parametric amplifier design showed an extremely high efficiency for this process to warrant further investigation. The device uses our standard NbTiN microstrip geometry with a 250 nm by 35 nm thick conducting layer separated from

the ground plane by a 190 nm amorphous Silicon dielectric. The capactive fingers use similar dimensions and are 37 μm long spaced every 2 μm along the device. Their length is sinusoidally modulated with an amplitude of 3 μm and 164 μm period to produce a band gap at 11 GHz.

We measure the conversion efficiency by first performing a VNA sweep to measure the transmission of the system. As the pump power is increased, some portion of the signal disappears from the VNA scan due to up-conversion (or other frequency translating parametric processes), defining a deamplification in dB. The result of such a sweep when optimized for maximum deamplification is shown in Figure 5.13. This procedure is then repeated by connecting the output to a spectrum analyzer and recording the power at $2\omega_p + \omega_s$.

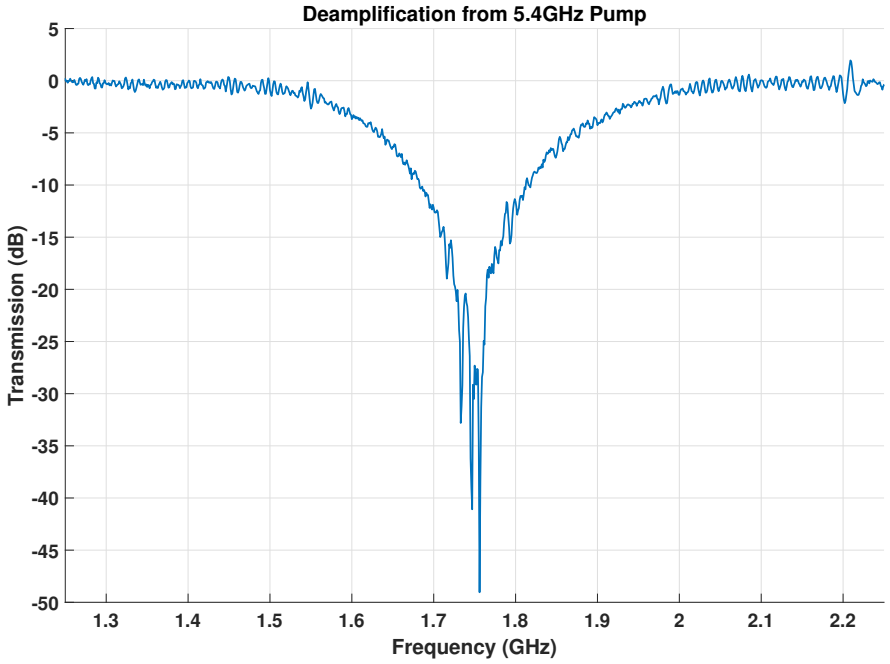

Figure 5.13: an S_{21} measurement with a 5.4 GHz applied pump relative to the un-pumped device transmission.

If the only source of deamplification were the up-conversion process, then the conversion efficiency would simply be

$$\eta = 1 - |S_{21}(\omega_s)|^2 \tag{5.18}$$

A known supplied signal power combined with our measurement of output idler power allows us to calculate the measured conversion efficiency given we know the

attenuation to and from the device. Considering an input signal of $P^{\text{in}}(\omega_s)$, the output idler power as seen by the spectrum analyzer will be

$$P^{\text{out}}(\omega_i) = |S_{21}^{\text{out}}(\omega_i)|^2 \left(\frac{\omega_s}{\omega_i}\right) \eta |S_{21}^{\text{in}}(\omega_s)|^2 P^{\text{in}}(\omega_s) \tag{5.19}$$

where $S_{21}^{\text{in}}(\omega_s)$ is the attenuation from the VNA to the device evaluated at the signal frequency, and $S_{21}^{\text{out}}(\omega_i)$ is the attenuation from the device to the spectrum analyzer at the up-converted frequency. The fraction ω_s/ω_i compensates for the increased energy per photon to give the efficiency η as the fraction of signal photons converted to idler photons. The result of this calculation is shown in Figure 5.14 as compared to the theoretical prediction according to equation 5.18 and the deamplification measured by the VNA.

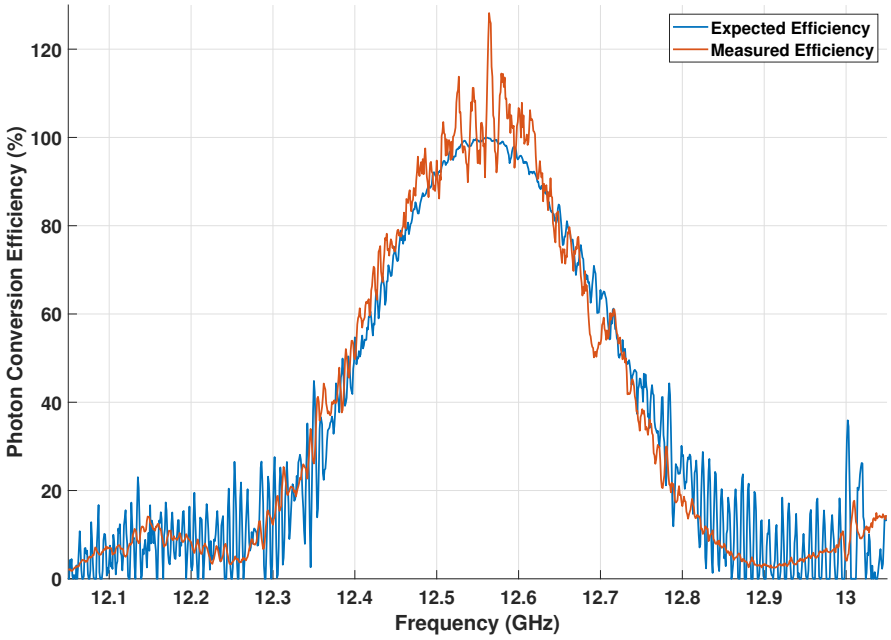

Figure 5.14: A plot of the photon conversion efficiency of the $\omega_s \rightarrow \omega_i$ parametric process as calculated from the missing signal at ω_s (blue) and measured output power at ω_i (red). The change in kinetic inductance due to a supplied current results in a shift of the frequency periodicity of the ripple in the S_{21} caused by standing wave reflections across the amplifier. Because the calculation is more sensitive to these changes in transmission at regions of higher power, we see an artifact of this in our result in areas of low conversion efficiency in the blue curve and high efficiency in the red curve.

In addition to the above result, we also see the expected onset of the sinusoidal

conversion between the signal and idler tones (see Figure 5.15), but are unable to complete the full cycle due to the limited length and I_c of the device.

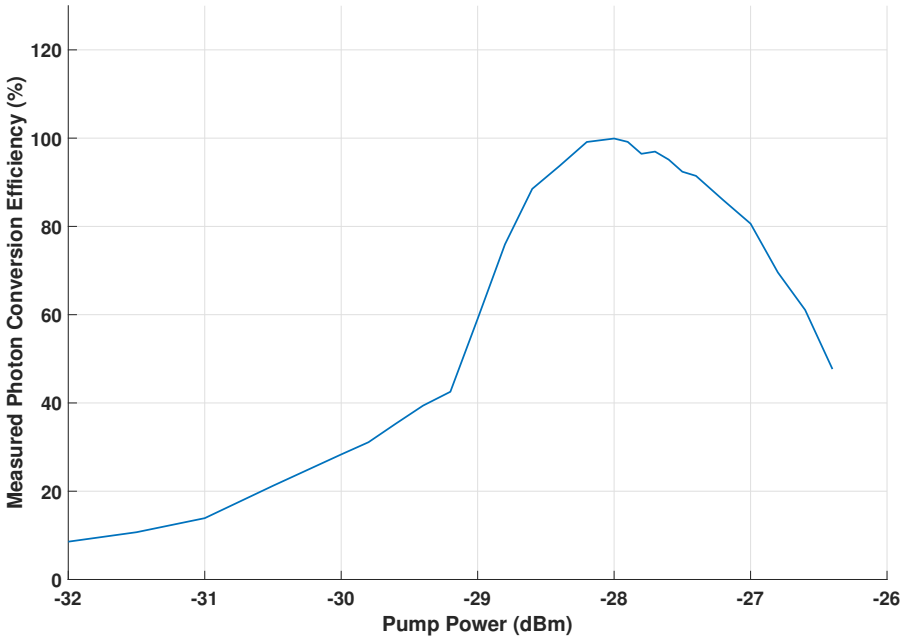

Figure 5.15: A plot of the photon conversion efficiency of the $\omega_s \rightarrow \omega_i$ parametric process for $\omega_s = 1.756$ GHz to $\omega_i = 12.556$ GHz as a function of pump power at the device.

Our results show that we can obtain nearly perfect conversion efficiency for a small range of frequencies. Expressed in terms of the conventional definition for the efficiency of multipliers (the ratio of output to input power), an input signal near 1.75 GHz is converted to a 12.55 GHz output with 717% efficiency due to the increased energy carried by each idler photon. While this device operates with only a limited bandwidth, the input signal can be tuned across several GHz for an alternate choice of pump frequency to provide an up-converted signal near 12.5 GHz above the engineered band gap. The conversion process for a 5.4 GHz pump was chosen due to its excellent efficiency compared to these other operating conditions. Future designs with dispersion optimized for these parametric processes rather than parametric amplification could hope to achieve significantly wider bandwidth. (Inspired by this result, one such prototype for a tripler device using third harmonic generation to generate an output tone at 104.6 GHz has been designed, built, and tested in a similar manner, producing over 30% conversion efficiency in terms of power with minimal heating from the 1 mW pump tone.)

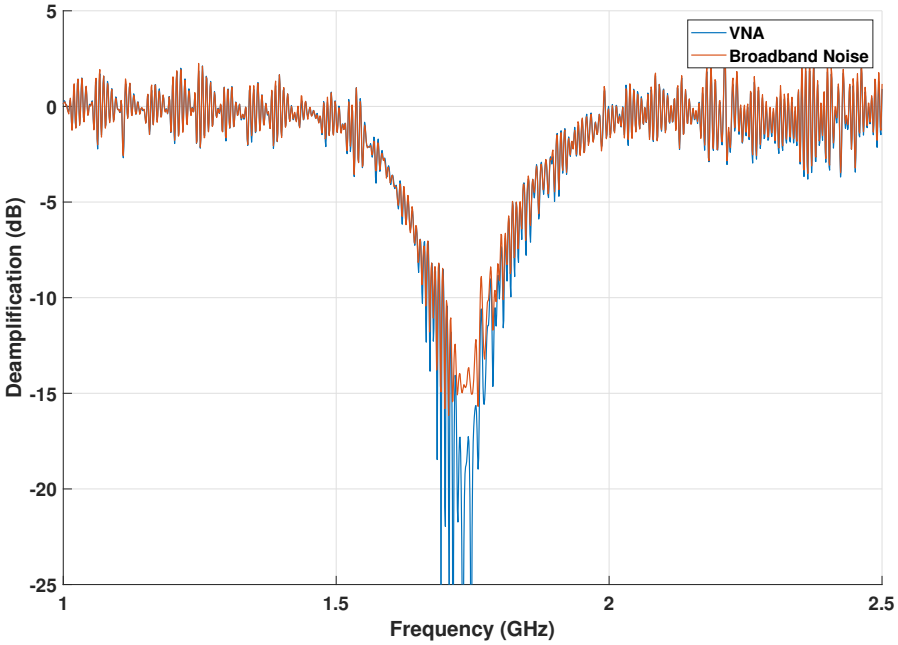

Figure 5.16: A plot of the deamplification as measured by a VNA (blue) or spectrum analyzer for a broadband noise input (red). The discrepancy at the maximum reduction in signal stems from reaching the noise floor of the measurement system and is not necessarily indicative of a fundamental limit of the device itself.

The up-conversion process described in this section is not limited to coherent input signals. Repeating this experiment using a broadband input noise source of roughly 20 Kelvin reproduces an identical result as shown in Figure 5.16. The conversion process greatly reduced the noise near 1.75 GHz, lowering the 20 Kelvin input to below a 1 Kelvin level at those frequencies.

Chapter 6

SUPERCONDUCTING ON-CHIP FOURIER TRANSFORM SPECTROMETER (SOFTS)

In this chapter, we describe the development of a novel integral field unit for mm/sub-mm telescopes where each pixel is read out using a Superconducting On-Chip Fourier Transform Spectrometer (SOFTS). The aim is to develop a high-resolution spectrometer with a significantly smaller footprint than presently available alternatives. Due to the low phase velocity within our devices $v_{\mathrm{ph}} \sim 1\%c$, a SOFTS interferometer would have a factor of 100 times smaller footprint compared to an optical FTS. The following sections will explore the scientific motivations for this endeavor, provide an overview of the theory of operations, present the experimentally measured results from our initial prototype, and comment on the currently ongoing effort to extend these results to a functional detector.

6.1 Motivation

Nearly 30 years ago, a Fourier transform spectrometer aboard NASA's COBE-FIRAS mission performed detailed measurements of the CMB and found it to closely resemble a 2.725 K black body spectrum.[121] Measured deviations from the standard plank curve, both in terms of its spatial anisotropy and spectral distortion, resulted in a radical advancement of our understanding of cosmology and continue to be an active area of research.

There are two primary types of distortion to the CMB spectrum, corresponding to redshifts $z < 10^5$ and $10^5 < z < 3 * 10^6$. The latter, produced during the epoch prior to recombination, results in a Bose-Einstein distribution that modifies the black body spectrum to

$$S_\nu(\nu, T, \mu) = \frac{2h\nu(\nu/c)^2}{e^{x+\mu} - 1} \tag{6.1}$$

where $x = hc\nu/kT$ and μ is the dimensionless, frequency-dependent chemical potential characterizing the distortion. This parameter is of particular interest as it can create significant constraints on various ΛCDM models of inflation.[122]

At lower redshifts after recombination, the interaction of the CMB with the hot electrons, e.g. in the gas surrounding primordial galaxy clusters, results in Compton Scattering that preferentially scatters the CMB to higher frequencies. This

scattering is commonly referred to as the Sunyaev-Zel'dovich effect and defines a 'Comptonization parameter,' y, by integrating over the time that the CMB interacts with the electron gas

$$y = \int_t \sigma_T n_e c \frac{kT_e}{m_e c^2} dt \tag{6.2}$$

where σ_T is the scattering cross-section and n_e and T_e are the electron density and temperature.[123] Ultimately, y sets the scale of the resulting deficit of CMB photons at lower frequencies and excess at higher frequencies compared to a pure black body, which thus provides an integrated history of the temperature and density of the gas it has interacted with.

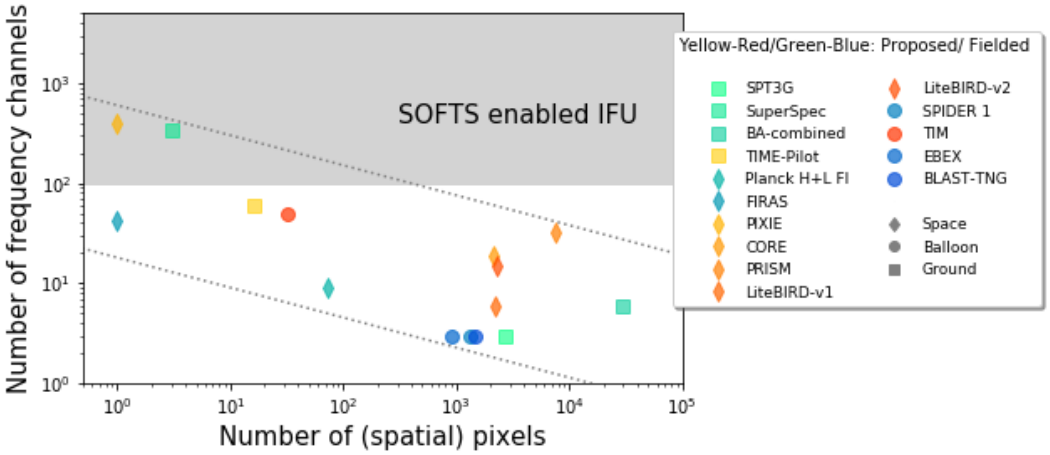

Figure 6.1: A broad survey of mm/submm experiments expressed as number of frequency channels versus number of spatial pixels where a clear trade-off is seen, [124, 125, 126, 127, 128, 121, 129, 130, 131, 132, 133, 134, 135, 136]. SOFTS technology can potentially break the trade-off, enabling $> 10^2$ spectral channels for all spatial pixels (grayed region). Note that this plot does not provide an accurate representation of the resulting mapping speed, which should be computed using metrics pertaining to the instruments and surveys being considered

A number of experiments investigating the CMB spatial anisotropies by the WMAP [137] and Plank [138] missions, SPIDER [134] and EBEX [135] balloons, the South Pole Telescope [139], the Atacama Cosmology Telescope [140], and the BICEP/Keck array [141] have yielded a plethora of insights for cosmology. Previous CMB measurements have been broadly comprised of spectrometers with a small number of pixels or broadband kilopixel cameras with limited spectral resolution. We see a general trade-off in spatial pixels and frequency channels (see Figure 6.1). Despite the enormous progress from those experiments, the COBE-FIRAS measure-

ment continues to set the strongest limits on the spectral distortions [142] because these experiments have largely focused on CMB imaging rather than spectroscopy.

In the case of multi-band imaging cameras, the spectral resolution is achieved by passing the signal from each pixel through N_c bandpass filters to define an equal number of frequency channels each with their own detector. The total number of detectors is scaled proportionally, $N_{\rm tot} = N_{\rm pix} N_c$, and instruments with a large number of pixels or frequency channels quickly run into the current limits of multiplexing technology. Packing limitations set further constraints on these quantities, particularly for space and balloon missions. Each spectral band for each pixel requires a set of filter banks and detectors that have a physical footprint which quickly fill up the available space in the focal plane and back-end readout system (see Figure 6.1).

Although the synchrotron and dust foregrounds exceed the CMB brightness at lower and higher frequencies, they have different spatial and temporal scales of coherency that can be used to disentangle the signals. A recent computational analysis of the foreground showed that unambiguous component separation requires simultaneous < 10 arcminute spatial resolution and < 2 GHz spectral resolution.[143] The aim of the SOFTS project is to develop technology that can realistically meet these measurement criteria in a manner similar to the CONCERTO instrument.[144]

These foregrounds for studying the CMB are also scientifically interesting for the field of Line Intensity Mapping (LIM) or spectral line tomography. In LIM, three-dimensional maps are made by combining the two imaged spatial dimensions with the redshift axis. At the frequencies of interest for studying the spectral distortions of the CMB, the LIM of the Hydrogen 21-cm line, redshifted [CII] line, and rotational CO transitions are excellent tracers of the reionization process in the early universe.[145] A new measurement technology capable of simultaneous spatial and spectral resolution could herald dramatic advancements in our understanding of the early epochs of our universe. SOFTS aims to alleviate these instrumentation issues by utilizing the device physics described in the following section.

6.2 Theory of Operation

Recall from section 2.1 that the inductance of a superconducting transmission line changes with an applied current via the relation

$$\mathcal{L}(I) \approx \mathcal{L}_0 \left(1 + \left(\frac{I}{I_*}\right)^2 + \left(\frac{I}{I'_*}\right)^4\right) \tag{6.3}$$

where I_* sets the scale for the nonlinearity . Since the phase velocity in a microwave transmission line depends on the inductance,

$$v_{\text{ph}} = \frac{1}{\sqrt{\mathcal{L}C}} \tag{6.4}$$

the phase velocity must also be current dependent. The electrical delay when traveling through a transmission line of length L is thus

$$\tau = \frac{L}{v_{\text{ph}}} = L\sqrt{\mathcal{L}C}. \tag{6.5}$$

Thus, as one applies a DC current, the increase in inductance results in an increased electrical delay for signals traveling through the transmission line. Alternatively, we can bundle the current-dependence of the inductance into an "effective length" (L_{eff}) of the transmission line:

$$L_{\text{eff}}(I) = L\sqrt{1 + \left(\frac{I}{I_*}\right)^2 + \left(\frac{I}{I'_*}\right)^4} \tag{6.6}$$

leading to the expression

$$\tau = \frac{L_{\text{eff}}}{\tilde{v}_{\text{ph}}} \tag{6.7}$$

where $\tilde{v}_{\text{ph}} = v_{\text{ph}}(0)$ is the phase velocity at zero current. The ability to control the effective electrical length of a transmission line readily lends itself to the construction of an interferometer. Consider a setup where an input signal is evenly split to travel along two identical transmission lines and later recombined and sent to a receiver. For a single tone input with power P_i, the power measured by the receiver will be given by

$$P = \frac{P_i}{2}\left(1 + \cos\Delta\phi\right) \tag{6.8}$$

where $\Delta\phi$ is the difference in phase delay between the two lines. Without loss of generality, we can choose to keep one of the transmission lines unbiased and apply a DC current bias to the other channel, resulting in a phase difference between the two of

$$\Delta\phi = \frac{2\pi\nu}{\tilde{v}_{\text{ph}}}(L_{\text{eff}}(I) - L_{\text{eff}}(0)). \tag{6.9}$$

The result is a microwave version of the classic Mach-Zehnder interferometer. In practice, the above expression will be slightly more complex as the zero-current transmission will never be truly identical for the two paths. Denoting the two channels as A and B, we can write the complete expression

$$\begin{aligned} P &= P_i\left(\frac{|S_{21,A} + S_{21,B}|^2}{4}\right) \\ P &= \frac{P_i}{4}\left(|S_{21,A}|^2 + |S_{21,B}|^2 + S^*_{21,A}S_{21,B} + S_{21,A}S^*_{21,B}\right). \end{aligned} \tag{6.10}$$

where S_{21} denotes the transmission of each channel between the splitter and combiner. The unconventional factor of 4 in the denominator stems from the choice of defining $S_{21,A/B}$ as the transmission of each path between the power splitter and combiner. Without loss of generality, we can choose an I-Q plane where $S_{21,A} = \mathrm{Re}(S_{21,A})$ and $S_{21,B} = |S_{21,B}|e^{i\Delta\phi}$. In this basis, the above expression becomes

$$\begin{aligned} P &= \frac{P_i}{4}\left(|S_{21,A}|^2 + |S_{21,B}|^2 + |S_{21,A}||S_{21,B}|e^{i\Delta\phi} + |S_{21,A}||S_{21,B}|e^{-i\Delta\phi}\right) \\ P &= \frac{P_i}{4}\left(|S_{21,A}|^2 + |S_{21,B}|^2 + 2|S_{21,A}||S_{21,B}|\cos\Delta\phi\right) \end{aligned} \tag{6.11}$$

Every term in the above expression (P_i, $|S_{21,A}|$, $|S_{21,B}|$, and $\Delta\phi$) is frequency dependent. The total power of the output on a detector is given by the integral of this power at all frequencies

$$\begin{aligned} P_\Sigma &= \int_0^\infty \frac{\Delta P_i(\nu)}{4\delta\nu}\left(|S_{21,A}(\nu)|^2 + |S_{21,B}(\nu)|^2 + 2|S_{21,A}(\nu)||S_{21,B}(\nu)|\cos\Delta\phi\right)d\nu \\ P_\Sigma &= \int_0^\infty \frac{\Delta P_i(\nu)}{4\delta\nu(|S_{21,A}(\nu)|^2 + |S_{21,B}(\nu)|^2)}\left(1 + \frac{2|S_{21,A}(\nu)||S_{21,B}(\nu)|}{|S_{21,A}(\nu)|^2 + |S_{21,B}(\nu)|^2}\cos\Delta\phi\right)d\nu \\ P_\Sigma &= \int_0^\infty \frac{\Delta P_i(\nu)}{4\delta\nu(|S_{21,A}(\nu)|^2 + |S_{21,B}(\nu)|^2)}\left(1 + C_f(\nu)\cos\Delta\phi\right)d\nu \end{aligned} \tag{6.12}$$

where $C_f(\nu)$ is the fringe contrast. Writing out the dependence on current explicitly

$$P_\Sigma(I) = \int_0^\infty \frac{P_0(\nu)}{2}\left(1 + C_f(\nu)\cos\left(\frac{2\pi\nu}{\tilde{v}_{\mathrm{ph}}}(L_{\mathrm{eff}}(I) - L_{\mathrm{eff}}(0))\right)\right)d\nu \tag{6.13}$$

where $P_0(\nu)$ is the output power at each frequency when $\Delta\phi = 0$. While the above expression tells us how the interferometer responds to a known incident spectrum as a function of current bias, the inverse relation is necessary for extracting useful data from the spectrometer. It is useful to define:

$$P_\mu = \int_0^\infty P_0(\nu)d\nu \tag{6.14}$$

and parameterize the current as a function of time $I = I(t)$ corresponding to the measurement sweep. If we then evaluate the expression

$$\begin{aligned} P_\Sigma(I) - P_\mu &= \int_0^\infty P_0(\nu)C_f(\nu)\cos\left(\frac{2\pi\nu}{\tilde{v}_{\mathrm{ph}}}(L_{\mathrm{eff}}(I) - L_{\mathrm{eff}}(0))\right)d\nu \\ P_\Sigma(t) - P_\mu &= \int_0^\infty P_0(\nu)C_f(\nu)\cos\left(\frac{2\pi\nu}{\tilde{v}_{\mathrm{ph}}}(L_{\mathrm{eff}}(t) - L_{\mathrm{eff}}(0))\right)d\nu. \end{aligned} \tag{6.15}$$

we see that the right-hand side resembles the standard Fourier cosine transform and its inverse, defined as:

$$\begin{aligned}\mathcal{F}_c[f(t)] = F_c(\nu) &= \int_0^\infty f(t)\cos(2\pi\nu t)dt \\ \mathcal{F}_c^{-1}[F_c(\nu)] = f(t) &= \int_0^\infty F_c(\nu)\cos(2\pi\nu t)d\nu.\end{aligned} \tag{6.16}$$

By choosing a particular sweep rate, we can switch the basis from current to time using the transformation

$$t = \Delta\tau = \frac{L_{\text{eff}}(I) - L_{\text{eff}}(0)}{\tilde{v}_{\text{ph}}} \tag{6.17}$$

where $\Delta\tau$ is the physical time delay difference between a signal travelling down each of the two STLs. We can then rewrite the above expression as

$$P_\Sigma(t) - P_\mu = \int_0^\infty P_0(\nu)C_f(\nu)\cos(2\pi\nu t)\,d\nu \tag{6.18}$$

and use the definition of the inverse cosine Fourier transform to solve for $P_0(\nu)$:

$$P_0(\nu) = \frac{1}{C_f(\nu)}\int_0^\infty \left(P_\Sigma(t) - P_\mu\right)\cos(2\pi\nu t)\,dt \tag{6.19}$$

Thus, using a calibration of the $|S_{21}|$ of both channels in the interferometer to calculate $C_f(\nu)$, a measurement of the power incident on the detector as a function of bias current, $P_\Sigma(t) = P_\Sigma(I)$, is sufficient to reconstruct $P_0(\nu)$ and therefore the incident power spectrum $P_i(\nu)$ via

$$P_i(\nu) = 4P_0(\nu)\frac{|S_{21,A}(\nu)|^2 + |S_{21,B}(\nu)|^2}{C_f(\nu)}\int_0^\infty \left(P_\Sigma(\Delta\tau) - P_\mu\right)\cos(2\pi\nu\Delta\tau)\,d\Delta\tau. \tag{6.20}$$

The above formulation of a Fourier-transform spectrometer predicts perfect reconstruction of the incident spectrum due to presuming no limitations on readout time or maximum current. The practical limits of a realistic spectrometer are discussed in the subsequent sections. A more complete check of the systematics associated with non-ideal transmission parameters based on simulated and measured data has been completed by our collaboration, see [146] for further detail that is not present in this manuscript.

Frequency Resolution

The highest frequency resolution the resulting spectrometer can provide is given by the inverse of the maximum current-induced time delay.

$$\min[\delta\nu] = \frac{1}{\max[\delta\tau]} \tag{6.21}$$

The maximum current-induced time delay, $\delta\tau$ is given by

$$\begin{aligned}\delta\tau &= \tau(I_{\max}) - \tau(0) \\ &= \frac{L_{\text{eff}}(I_{\max}) - L(0)}{v_{\text{ph}}}.\end{aligned} \tag{6.22}$$

Taking only the first term in our expansion of $L_{\text{eff}}(I)$ (since in practice $I_{\max}$ is significantly smaller than I_*), we obtain

$$\begin{aligned}\delta\tau &= \frac{L}{\tilde{v}_{\text{ph}}}\left(\sqrt{1+\alpha\left(\frac{I_{\max}}{I_*}\right)^2} - 1\right) \\ \delta\tau &\approx \frac{L}{\tilde{v}_{\text{ph}}}\left(\frac{\alpha}{2}\left(\frac{I_{\max}}{I_*}\right)^2\right)\end{aligned} \tag{6.23}$$

where we have used the fact that $I_{\max}$ is typically significantly lower than I_*. In terms of frequency resolution,

$$\min[\delta\nu] \approx \frac{2\tilde{v}_{\text{ph}}}{\alpha L}\left(\frac{I_*}{I_{\max}}\right)^2. \tag{6.24}$$

Thus, we find that the interferometer's resolution is increased as the physical length increases, the phase velocity is reduced, and the maximum applied current (prior to exceeding the breakdown current of the superconductor I_c) is increased.

The zero-current inductance of a superconductor is given by Mattis Bardeen Theory as

$$\mathcal{L}_k = \frac{\hbar R_n}{\pi\Delta} \tag{6.25}$$

where R_n is the normal state resistance and Δ is the superconducting band gap. For a given superconducting material, the phase velocity (eq. 6.4) is thus only reduced by increasing the normal state resistance via shrinking the transverse physical dimensions (width and height) of the transmission line. Ultimately, R_n scales inversely with the cross-sectional area (A) of the microstrip.

$$\tilde{v}_{\text{ph}} \propto \frac{1}{\sqrt{\mathcal{L}}} \propto \frac{1}{\sqrt{R_n}} \propto \sqrt{A} \tag{6.26}$$

Similarly, the critical-current density (J_c) of the superconductor is given by Ginzburg-Landau theory as

$$\begin{aligned}J_c &= \frac{2}{3\sqrt{3}}\frac{\psi_\infty^2 e^*\hbar}{m_*\xi} \\ \psi_\infty^2 &= \frac{m^* c^2}{4\pi e^{*2}\lambda^2}\end{aligned} \tag{6.27}$$

leading to the result that the critical current ($I_c \approx I_{\max}$) in a thin superconducting film is proportional to the cross-sectional area.

$$I_{\max} \propto J_c A \propto A \tag{6.28}$$

The scale of the nonlinearity set by I_* can be roughly approximated by equation the kinetic energy of Cooper pairs ($L_k I^2/2$) to the pairing energy E_p and solving for the current. In doing so,

$$\begin{aligned} \frac{1}{2} L_k I_*^2 &\approx E_p \\ \frac{1}{2} L_k I_*^2 &\approx 2 N_0 \Delta^2 V \end{aligned} \tag{6.29}$$

where N_0 is the density of states at the Fermi level, V is the volume, and Δ is the superconducting band gap. Rewriting this expression in terms of per unit length along the microstrip:

$$\begin{aligned} \frac{1}{2} \mathcal{L}_k I_*^2 &\approx 2 N_0 \Delta^2 A \\ I_*^2 &\approx \frac{4 N_0 \Delta^2 A}{\mathcal{L}} \\ I_*^2 &\approx \frac{4 N_0 \pi \Delta^3 A}{\hbar R_n} \end{aligned} \tag{6.30}$$

we see that the result has a scaling of

$$\begin{aligned} I_*^2 &\propto \frac{A}{R_n} \propto A^2 \\ I_* &\propto A. \end{aligned} \tag{6.31}$$

Combining these together, we can express how $\delta\tau$ scales as

$$\begin{aligned} \delta\tau &\propto \frac{L}{\tilde{v}_{\text{ph}}} \left(\frac{I_{\max}^2}{I_*^2} \right) \\ &\propto \frac{L}{\sqrt{A}} \left(\frac{A^2}{A^2} \right) \\ \delta\tau &\propto \frac{L}{\sqrt{A}} \end{aligned} \tag{6.32}$$

and the smallest frequency resolution scales as

$$\min[\delta\nu] \propto \frac{\sqrt{A}}{L}. \tag{6.33}$$

Therefore to maximize the resolution of the spectrometer, one should reduce the cross-sectional area of the microstrip and increase the overall length of the device. Practical limitations pose some challenge to indefinitely scaling both of these parameters.

The cross-sectional area, A, can be reduced by either creating thinner superconducting films or reducing the width of the conducting section after etching. Our typical designs consist of a 35 nm $*$ 250 nm NbTiN conductor, which is within a few factors of two of the limits of the minimum viable film deposition and stepper accuracy of our fabrication process. Pushing closer to these limits is not necessarily advisable as reducing the cross-sectional area further not only lowers the $I_{\max}$ for the DC bias, but also the corresponding maximum RF power than can be applied. Our current geometry is typically capable of supporting input powers on the order of 1 μW prior to experiencing any strong non-linear effects. Applications with high dynamic range or bright input sources might restrict the minimum suitable cross-sectional area prior to any fabrication limitations.

Increasing the device length, L, encounters similar challenges. As the length increases, the probability of imperfections in the NbTiN film creating weak spots that limit I_c rises accordingly (see section 4.1). The optimal length for the spectrometer will be an optimization based on the above scaling and the frequency (and impact) of imperfections in the superconducting film for the particular fabrication process. Anecdotally, the typical I_c we obtain in our 2 cm long devices is 1 mA, while the average I_c for otherwise identical 11 cm long chips is usually only 0.5 mA due to the presence of these weak links. Because this is a statistical process, we do occasionally find longer devices with an I_c exceeding 1 mA, but those are fairly rare ($< 5\%$ of the chips we screen). These fabrication issues are effectively a limit on expected yield. One could in principle create arbitrarily long spectrometers with no reduction to I_c if they are willing to search for the one optimally working device among dozens or hundreds of samples.

In applications where many spectrometers are necessary, such as having one spectrometer reading out each pixel of a focal plane array, there may be additional limitations on the length based on the maximum physical footprint available to accommodate each device. While the conductor and capacitive fingers of our devices are typically less than 50 μm wide, the scaling of the area on chip per unit length gives an effective with of closer to 500 μm in reality due to the particular wrapping geometry we use. Under these conditions, a 3-inch diameter 1 kilo-pixel array of interferometers could only support a maximum length of 1 cm per device simply due to size considerations.

Minimum and Maximum Frequencies

The minimum frequency the interferometer can measure is limited by the lowest mode each arm can support, given by the ratio of phase velocity to device length.

$$\nu_{\min} = \frac{v_0}{L} \tag{6.34}$$

This frequency also sets the minimum frequency difference between two input tones that is possible to resolve. However, this measure is only useful for calibration testing as for a realistic input signal comprised of multiple unknown frequencies, the smallest difference in frequency that can be resolved without that a priori knowledge is given by equation 6.24.

The maximum frequency allowed by the interferometer is the minimum between that set by the superconducting bandgap

$$\nu_{\max} = \frac{\Delta}{\hbar} \tag{6.35}$$

or the capacitive fingers, which form quarter-wave resonators at a sufficiently high frequencies.

$$\nu_{\max} = \frac{4v_0}{L_{\text{fin}}} \tag{6.36}$$

For NbTiN, the stronger limit set by the bandgap of 1.2 THz, which corresponds to an equivalent limit on capacitive finger length of just under 10 μm. As discussed in Chapter 2, the capacitive finger length necessary for impedance matching is degenerate with their spacing and dielectric thickness; therefore, it is generally possible to choose a sufficiently short length for the design given the limits set by the fabrication process.

Dynamic Range

Due to the relation of the inductance on the current, any incident power will also change the inductance. The fractional change of inductance from an incident current with non-zero frequency is

$$\frac{\delta \mathcal{L}_k}{\mathcal{L}_k} \approx \frac{I}{I_*} \approx \frac{9.7e^2 D\eta_0 P}{\hbar\omega^2\Delta_0} \tag{6.37}$$

where D is the diffusion coefficient, η_0 is the impedance of the vacuum (377Ω), Δ_0 is the superconducting bandgap at 0 Kelvin, and ω and P are the incident frequency and power of the signal.[147] To a first order approximation, the incident power is split across the two lines, this change in inductance should be identical for the two paths; however, that symmetry breaks when I_{DC} is an appreciable fraction of I_*.

If the incident power is large enough to create a noticeable change in inductance, then the phase change through the interferometer becomes a function of the incident power, creating a systematic error in the result. The degree to which this limits dynamic range depends on the desired resolution of the experiment.

In addition, a sufficiently large incident power will cause a breakdown in superconductivity, similarly to exceeding the DC critical current of the device. For the NbTiN devices we have tested, this occurs roughly when the incident power exceeds $10\mu\mathrm{W}/I_c(\mathrm{mA})$. The dynamic range will then be the ratio between this maximum incident power divided the measurement bandwidth and the noise floor of the power detector reading out the SOFTS channel.

6.3 Initial Prototype

Utilizing this scheme of phase velocity control, we constructed and characterized a prototype Superconducting On-chip Fourier Transform Spectrometer (SOFTS) device using two current-controlled parametric amplifiers, which behave as simple transmission lines when operated significantly below the band gap without an applied pump.[148]

The two parametric amplifiers were both microstrips comprised of a crystalline Silicon subtrate with a 35 nm layer of NbTiN deposited via reactive sputtering. The transmission lines were 250 nm wide and rested below a 190 nm amorphous Silicon dielectric that separated them from the 50 nm NbTiN ground plane above them. In order to achieve proper impedance matching, the transmission line was periodically widened with perpendicular 250 nm wide "fingers" that provide extra capacitance to the ground plane. For one of these devices, these fingers were 37 μm long and spaced 2 μm apart. For the second, the fingers were 14 μm long and spaced 0.75 μm apart. Both cases achieve nominal 50 Ω impedance matching.

The measurement scheme is shown in Figure 6.2. The device was calibrated by applying a test tone from one port of the VNA and recording the summed power after its path through the interferometer. This measurement was then repeated for a linear sweep of bias currents on one of the two STLs between $I = 0$ and $I = I_{\mathrm{max}}$. The complex S_{21} for each individual STL was recorded in a previous calibration and is shown in Figure 6.3.

Figure 6.5 shows the normalized summed output power plotted vs the time delta $\Delta\tau$ between the two transmission lines for several input frequencies. One can see the recovery of the expected cosine function of output power vs time.

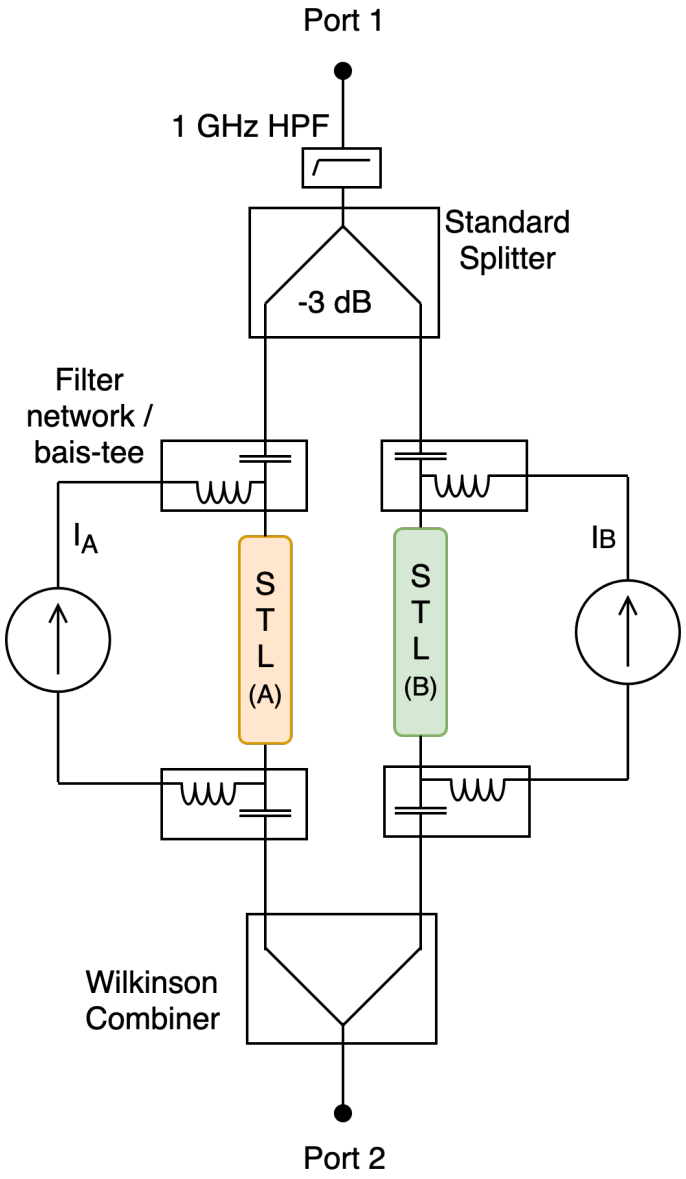

Figure 6.2: The experimental setup used for the initial SOFTS prototype. Ports 1 and 2 are connected directly to a Copper Mountain C4220 VNA outputting a nominal 100 pW signal. The signal is high-pass filtered (>1 GHz) to eliminate a spurious 10 MHz signal and split using a standard 3dB splitter. The DC bias for the two lines is applied through two BT-0026 bias tees connected to a DC power supply through a 1098 Ohm series resistance. While the setup allows us to apply current to both superconducting transmission lines (STLs) for redundancy, only the STL with the larger experimentally measured I_c/I_* was biased during operation. The signal then travels through two sets of long coaxial cables (not shown) to the STLs mounted on the 1 K stage inside our cryostat. The DC signal path is completed by another set of BT-0026 bias tees which are shorted to ground, then the RF output is summed by a broadband Wilkinson Combiner and returned to the VNA.

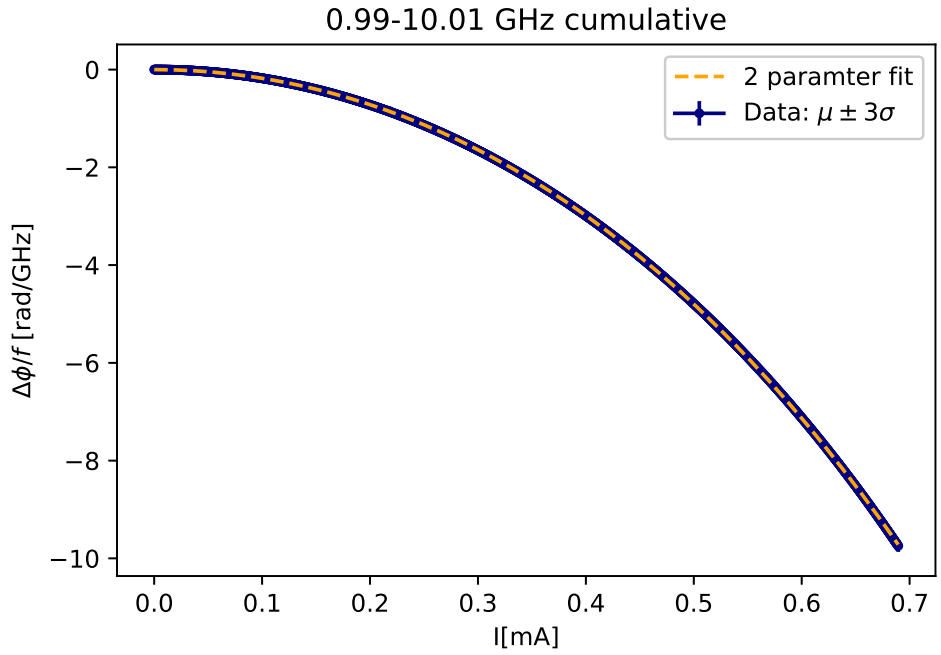

Figure 6.3: Data and fit of the phase delay for one of the STLs as a function of applied DC current for all frequencies between 1 and 10 GHz.

The data collection occurred over the course of many hours, and the cryostat used for this experiment did not have automatic temperature stabilization control. Over the course of the measurement, the temperature of the stage increased by over 0.5 K, introducing a frequency-dependent loss. Furthermore, the particular measurement setup used in this experiment produced a large amount of excess power below 10 MHz that resulted in frequency-dependent loss in our STLs via some unknown mechanism that would strengthen with the applied I_{DC}. This additional loss for applied bias current is shown in Figure 6.4.

Because the data cube was taken from low to high current and the need for additional low frequency filtering was not identified until several months after the conclusion of this experiment, the excess losses from these mechanisms systematically arise at the higher values of current as can be seen by the "decay" in the amplitude of the cosine modulation (by virtue of the decrease in C_f due to the lowered S_{21} as defined above). As a result, the fitting was performed with an additional exponential factor $e^{-\gamma(\nu)\tau}$ to account for this change in S_{21}.

The process performed in this initial SOFTS demonstration shows every step of the calibration and current-induced response necessary to reconstruct an unknown

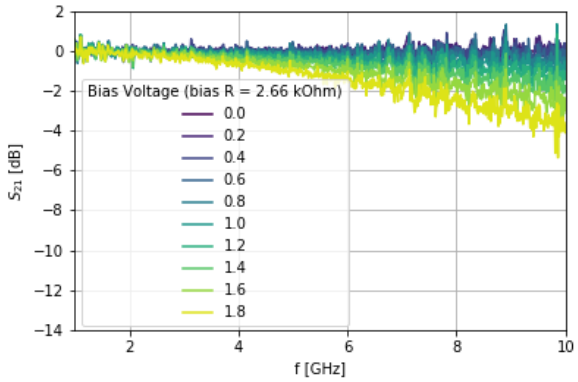

Figure 6.4: The change in the S_{21} with applied current for the STL and setup used in the initial SOFTS prototype.

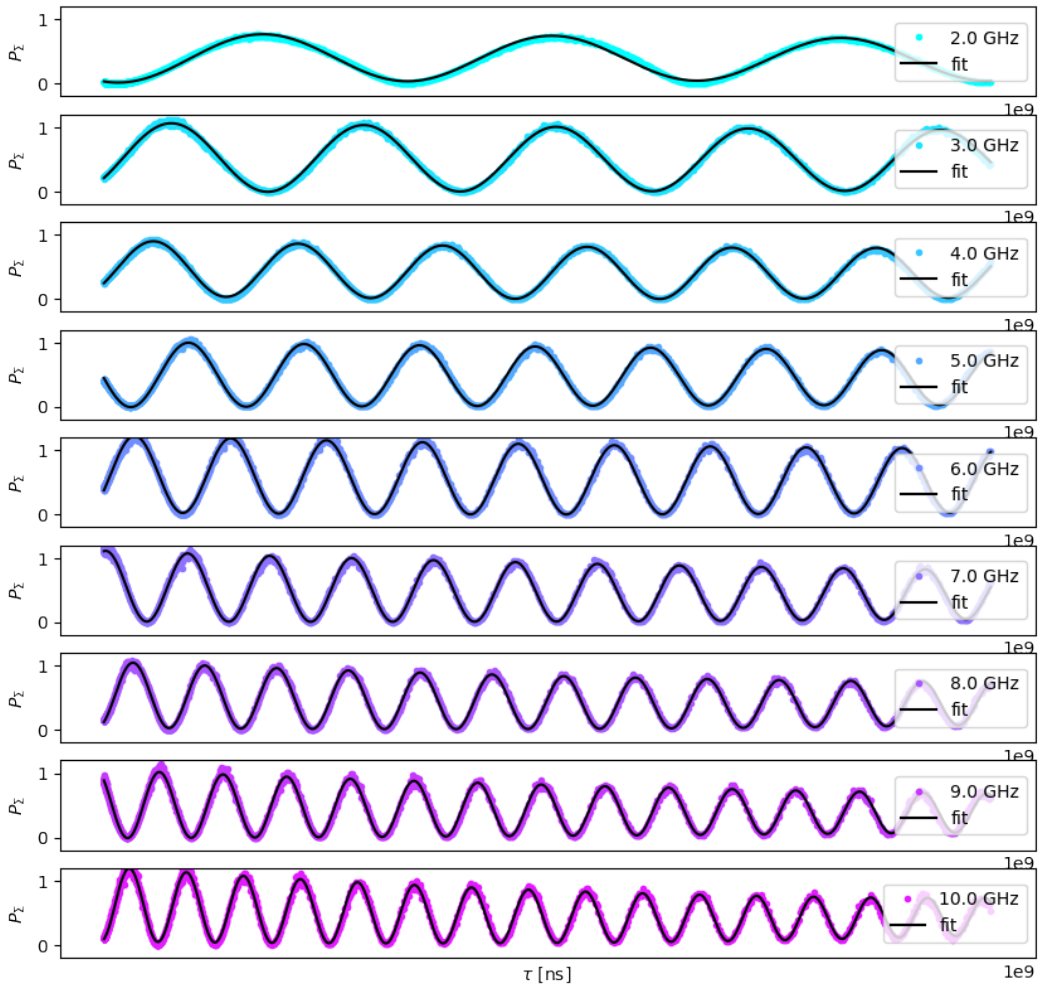

Figure 6.5: Summed power as a function of delay $P_\Sigma(\Delta\tau)$ for a number of frequencies between 2 and 10 GHz.

incident signal $P_i(\nu)$ as derived in the previous section. Specifically, we have experimentally demonstrated the measurement in Equation 6.13 for a variety of single-tone inputs and the capability of extracting the incident spectra from the data analogously to the method in Equation 6.20.

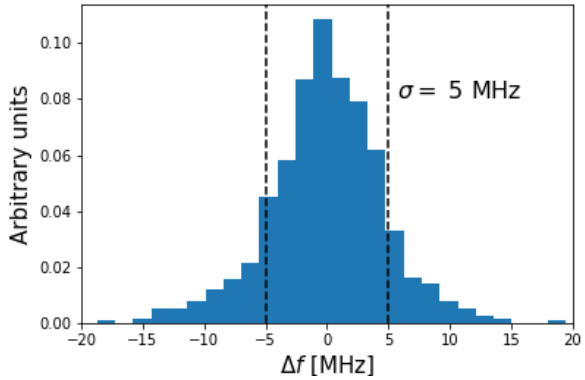

Figure 6.6: Summed power as a function of delay $P_\Sigma(\Delta\tau)$ for a number of frequencies between 2 and 10 GHz.

Because we only used single-tone inputs, the limit on the achievable fitting is given by Equation 6.34 and calculated to be 4.2 MHz derived from the phase noise of the VNA setup. A histogram of the error between the input and reconstructed frequencies is shown in Figure 6.6 and produces a roughly normal distribution with a standard deviation of 5 MHz, an overall great agreement with the theoretical prediction, even considering the nonideal behavior of this physical device.

These results demonstrated a novel application of nonlinear inductance by modifying a transmission line to build a working interferometer. The interferometer achieved a resolution of 5 MHz with an un-optimized physical length-scale of only 25 mm, a substantially smaller size than alternatives such as optical Fourier transform spectrometers.

6.4 Ongoing Efforts

Since the initial demonstration, the number of people working on developing a more optimized SOFTS device has grown considerably. The immediate effort over the past two years has focused on designing, simulating, and experimentally testing a fully integrated single SOFTS pixel, as shown in Figure 6.7.

The four-port SOFTS mask containing everything in the aforementioned setup is shown in Figure 6.8. This particular device is designed to operate roughly in the Ka-

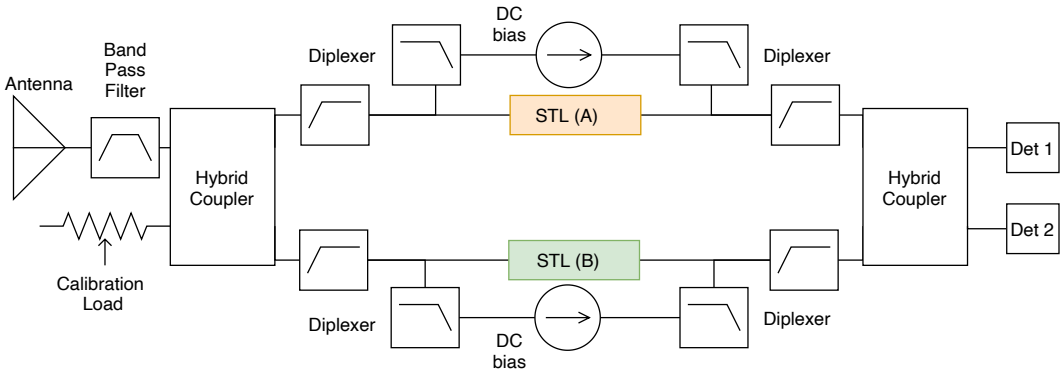

Figure 6.7: A schematic diagram of a single SOFTS pixel reading out an an antenna. The measurement band is set by a bandpass filter prior to being split to the two STLs via a hybrid coupler. A diplexer combines this signal with the DC bias current, until the signals from the two paths are recombined and the summed and difference modes are sent to detectors 1 and 2.

band, between 24-37 GHz, which is set by the hybrid coupler (see Figure 6.9). Given the design of this device, we expect a nominal frequency resolution, $\delta\nu = 1.43$ GHz for a nonlinearity $(I/I_*)^2$ in the one of the STLs of 20% (comparable to performance we have obtained in travelling wave parametric amplifiers with similar designs).

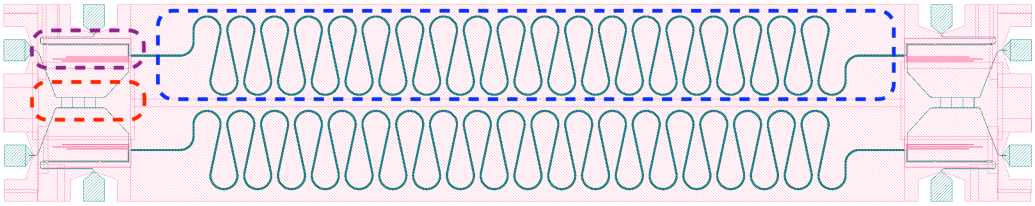

Figure 6.8: A top-down view of the physical design of the initial Ka-band SOFTS system, showing the Hybrid Coupler (red), Diplexer (purple), and meandering Superconducting Transmission Line (blue). The physical dimensions of the above setup are only 1.15 mm $\times$ 6.08 mm.

This design has recently been fabricated and is in the process of being experimentally tested at the time this document is being written. While awaiting this major milestone of realizing a fully-functional single-wafer small-scale interferometer, we have put in a significant amount of effort in simulating the projected performance of an array of such devices for some of the science cases discussed at the start of this chapter.

Consider a system with an antenna at the focal plane of a telescope with optical throughout $A\Omega$ read out by a SOFTS after a band-selection filter. The Noise

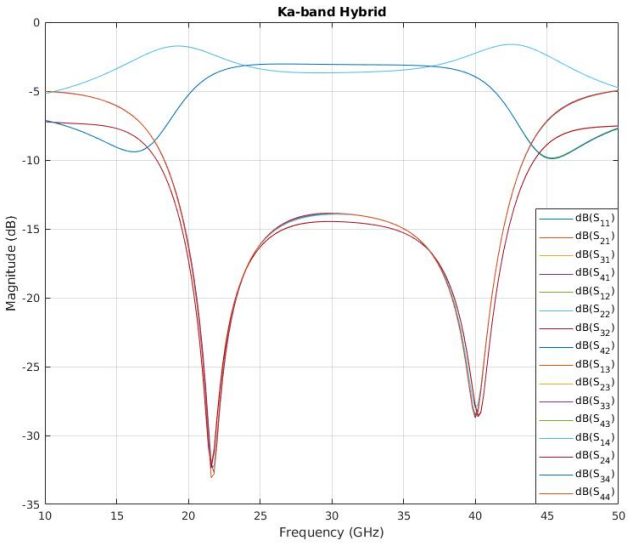

Figure 6.9: Simulated S-parameters of the hybrid coupler in Sonnet showing a working bandwidth of 24-37GHz.

Equivalent Power (NEP) on the readout detector behind this pixel is given by

$$\mathrm{NEP}^2_{\mathrm{photon}} = 4\frac{(kT_N)^5}{h^3}\int_{x_{min}}^{x_{max}} \frac{A\Omega}{c^2}\frac{x^4}{e^x-1}\left(1+\frac{\bar{\eta}}{e^x-1}\right)\bar{\eta}dx \tag{6.38}$$

where

$$x \equiv \frac{h\nu}{kT_N} \tag{6.39}$$

and $\bar{\eta}$ is the product of source emissivity, detector absorption efficiency, and the transmissivity of the system connecting them. (Note that we have taken $A\Omega$ inside the integral, as those are generally frequency-dependent parameters.) Under the single-mode condition (when $A\Omega/c^2 = \nu^{-2}$) this simplifies to

$$\mathrm{NEP}^2_{\mathrm{photon}} = 4\frac{(kT_N)^3}{h}\int_{x_{min}}^{x_{max}} \frac{x^2}{e^x-1}\left(1+\frac{\bar{\eta}}{e^x-1}\right)\bar{\eta}dx. \tag{6.40}$$

As an example, for a device operating between 80 and 160 GHz for $\eta \approx 1$, the NEP would be roughly 20 aW/$\sqrt{\mathrm{Hz}}$. Assuming the SOFTS is read out by a low-noise detector such as an MKID or TES (in the case of high-altitude balloons or space observations), the NEP of each pixel will be roughly equal to $\mathrm{NEP}_{\mathrm{photon}}$. As we perform the fourier transform of the time series measured by the detector, this noise will be distributed among N_c spectral channels given by the frequency resolution, δ_ν.

$$N_c = (\nu_{max} - \nu_{min})/\delta\nu \tag{6.41}$$

Under these assumptions, the minimum brightness sensitivity of a signal (SNR = 1) for an observation time $t_{\rm obs}$ is given by

$$\sigma_B = \frac{\mathrm{NEP}_{\rm photon}}{\sqrt{t_{\rm obs}}} \left(\frac{1}{(\delta\nu) A\Omega} \right) \tag{6.42}$$

in units of Watts per square meter steradian Hz.

We then consider a focal plane roughly split into three bands. Approximating the area per pixel of roughly $(c\nu_{min})^2$ scaled by a packaging efficiency factor of 0.8, we can comfortably fit over 400 detectors into an 83 mm radius focal plane. Separating this focal plane into three bands, we can cover it with a 5×5, 13×13, and 15×15 grid of pixels for each band as given in Table 6.1.

Focal plane details			
Number of Pixels	Resolution [GHz]	min. freq. [GHz]	max. freq. [GHz]
25	2	30	90
169	5	80	240
225	12	180	540

Table 6.1: An example of a realistic IFU focal plane where each pixel is read out by a SOFTS with designed parameters and filtering providing the given resolution, minimum, and maximum frequencies.

Taking $A\Omega \approx \lambda^2$ and an observation time of $t_{\rm obs} = 1$ day, we can calculate σ_B as given by equation 6.42 when looking at the CMB. The result of this particular setup is shown in Figure 6.10 compared to the scale of the Sunyaev-Zel'dovich distortion for $y = 10^{-6}$, corresponding to the level of the strongest currently imposed experimental limits on the distortion.[149] As can be seen by these results, in the photon-noise dominated limit, the proposed SOFTS setup could in principle expand the limits on CMB spectral distortion while providing hundreds of pixels for spatial imaging.

The optimal choice of number of frequency bands, resolution of each band, and number of pixels per band depends heavily on the particular science cases of interest. In tandem with our experimental efforts, we have been actively working on data-driven simulations for optimizing these focal plane parameters for CMB distortion and Line Intensity Mapping measurements.

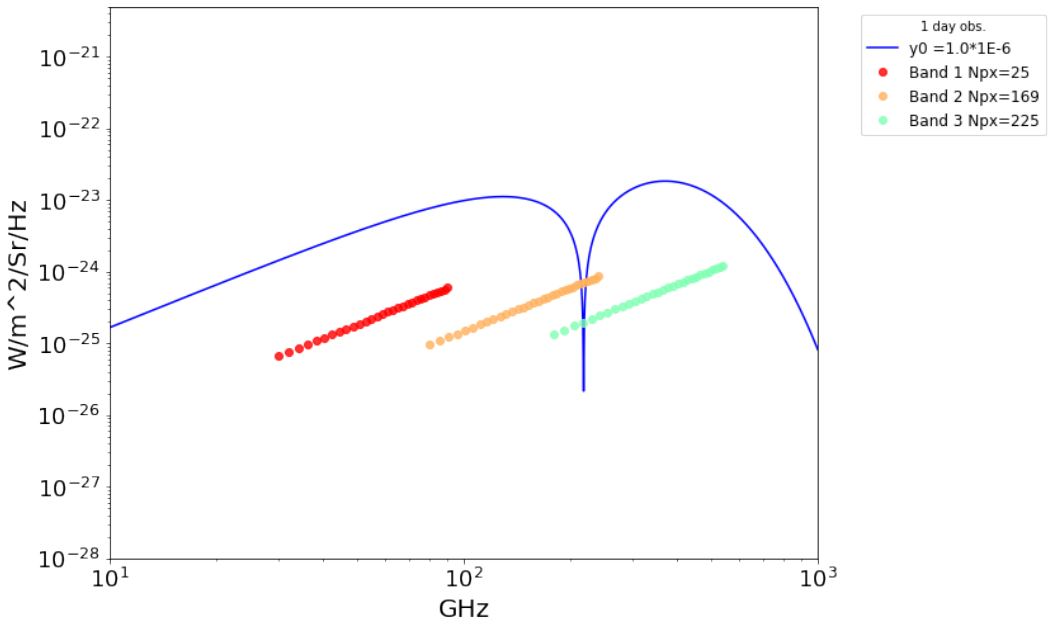

Figure 6.10: A plot of the brightness change in the CMB distortion for $y = 10^{-6}$ compared to the minimum detectable signal level of the above IFU+SOFTS scheme with $t_{\rm obs} = 1$ day.

Chapter 7

HIDDEN PHOTON DARK MATTER

Over the past few decades, several families of cold light particles produced during inflation have emerged as viable candidates for explaining the dark matter component in our universe.[150] Hidden photons, a hypothesized type of massive vector bosons resulting from a new U(1) symmetry that couples to the standard model hypercharge.[151] They can either comprise the entirety of the dark matter component of the universe or merely a component within it that weakly couples to the standard model.[152]

The Lagrangian for ordinary photons A^μ, hidden photons X^μ, and their coupling may be written as

$$\mathcal{L} = -\frac{1}{4}F_{\mu\nu}F^{\mu\nu} - \frac{1}{4}\tilde{X}_{\mu\nu}\tilde{X}^{\mu\nu} - \frac{\chi}{2}F_{\mu\nu}\tilde{X}^{\mu\nu} + \frac{m_{\gamma'}^2}{2}\tilde{X}_\mu\tilde{X}^\mu + J^\mu A_\mu \tag{7.1}$$

where F and $\tilde{X}$ are field strength tensors for photons and hidden photons, $m_{\gamma'}$ is the hidden photon mass, J^μ is the electromagnetic current, and χ is the kinetic mixing parameter governing the strength of the interaction.[153]

7.1 Dish Experiments

In the presence of hidden photon dark matter with density ρ_{HPDM}, the presence of the kinetic mixing term in the above Lagrangian results in an oscillating ordinary electric field with an average amplitude of

$$\sqrt{\langle |E_{\mathrm{HP}}|^2 \rangle} = \chi\sqrt{2\rho_{\mathrm{HPDM}}} \tag{7.2}$$

and frequency [154]

$$\nu_{\mathrm{HP}} = \frac{m_{\gamma'}}{2\pi} = 0.24\ \mathrm{GHz}\left(\frac{m_{\gamma'}}{\mu\mathrm{eV}}\right). \tag{7.3}$$

In the presence of a metallic surface with boundary condition $E_{||} = 0$, this results in the emission of photons perpendicular to the surface. Thus, by using a spherical dish, one can concentrate the power

$$P_{\mathrm{center}} \approx \chi^2 \rho_{\mathrm{HPDM}} A_{\mathrm{dish}} \tag{7.4}$$

onto the center of the sphere.[154] Coupling that concentrated power into an antenna enables us to search for the hidden photon signal by observing the presence of absence of excess power at ν_{HP}.

For a model of hidden photons as a gas with random orientations of velocity relative to the surface of the dish, the expected sensitivity for χ given a minimum detectable power P_{det} will be

$$\chi_{\mathrm{sensitivity}} = 3.7 \times 10^{-14} \left(\frac{P_{\mathrm{det}}}{10^{-23}\mathrm{W}}\right)^{\frac{1}{2}} \left(\frac{0.3\mathrm{GeV/cm}^3}{\rho_{\mathrm{HPDM}}}\right)^{\frac{1}{2}} \left(\frac{1\mathrm{m}^2}{A_{\mathrm{dish}}}\right) \tag{7.5}$$

where ρ_{HPDM} is the local density of the hidden photons component of dark matter.[154]

This method of dark matter detection offers an alternative to the more traditional approach of haloscopes used in axion searches such as ADMX [155] or other cavity experiments.[156] The main advantage of dish-based searches stems from their potentially large instantaneous bandwidth which is only limited by the coupling of the antenna and readout electronics. In contrast, the bandwidth of the cavity resonance in haloscope experiments is tunable but quite narrow, which significantly increases the integration time for searches spanning a large range of $m_{\gamma'}$. The benefit of the haloscope method stems from the large obtainable quality factors in the cavities (on the order of 10^6), significantly boosting the dark matter signal. To obtain a roughly equivalent signal level, a dish experiment would need to cover an area of $A_{\mathrm{dish}} \sim Q\lambda_{\mathrm{DM}}^2$, which is challenging at lower frequencies of a few GHz but easily achieved for higher-frequency measurements above 100 GHz.

Over the past few years, several experiments have already utilized the dish approach to set new limits for hidden photon dark matter at millimeter and sub-millimeter frequencies.[157, 158, 159, 160] These experiments have generally aimed to maximize their sensitivity through a very large dish, typically more than 1 m^2 in area and kept at room temperature. Despite this progress, a large amount of parameter space remains largely unexplored, particularly at frequencies above 7 GHz. These frequencies are especially notable due to the relatively weak limits set by the Cosmic Microwave Background [161] and Stellar measurements [162].

7.2 Experimental Setup

Our experimental design closely mirrors these previous experiments, but our approach for maximizing sensitivity aims to use the near-quantum limited noise performance of our parametric amplifiers to minimize readout noise and thereby lower the

minimum detectable power. To fully utilize these readout capabilities, we must also limit the incident noise background by cooling the antenna, dish, and surrounding parasitic thermal emission to sub-Kelvin temperatures. In doing so, the dish area is subsequently limited by the available space inside the dilution refrigerator, which could at most support a dish of slightly less than one meter in area. To accommodate the simultaneous cooldown of several other experiments, the dish size was limited to only 12.7 cm in diameter, resulting in a collection area of only 0.0127 m^2 for our initial run. In future experiments, this could further be optimized by careful consideration of impedance matching to the dark matter signal.[163]

A schematic diagram of our experimental setup is shown in Figure 7.1. A cold switch before the input of the parametric amplifier allows for the incident signal to be switched between the dish plus horn antenna [164] and a 20 mK load that is used for reference data. When this switch is set to the reference load, the setup is identical to the noise-measurement setup in 4.17 and was used to characterize the parametric amplifier noise performance in the days prior to our dark matter search.

To perform the dark matter search, first we perform a y-factor measurement of the parametric amplifier noise as described in section 4.4, which calibrates the output noise measured by our spectrum analyzer to the noise at the input of the parametric amplifier. Next, we integrate the signal emitted by both the dish and reference load for 8.272 hours each (corresponding to an integration of a few minutes per bin). This sweep is performed from 3.899 to 7.399 GHz, covering the 3.5 GHz bandwidth centered around half the pump frequency of our parametric amplifier within which we see more than 15 dB of gain. The spectrum analyzer measurement is performed using a flat top resolution bandwidth of 3 kHz and video bandwidth of 3 Hz, chosen so that we could extract the spectral profile of the dark matter signal with a width $\delta\nu \approx 10^{-6}\nu$ due to the relative velocity of the galactic dark matter halo and the dish. The spectrum analyzer has an instantaneous bandwidth of approximately 160 MHz utilizing a high-speed digitizer followed by a digital FFT,[98] resulting in an integration time of roughly 5 minutes at each frequency for this experiment. The measurement speed could be significantly increased through the use of readout electronics capable of instantaneous measurement across the entire frequency band.

7.3 Results and Discussion

The results in this section are based on preliminary analysis that has not yet been subject to rigorous peer-review. At the time of writing, we are still actively in

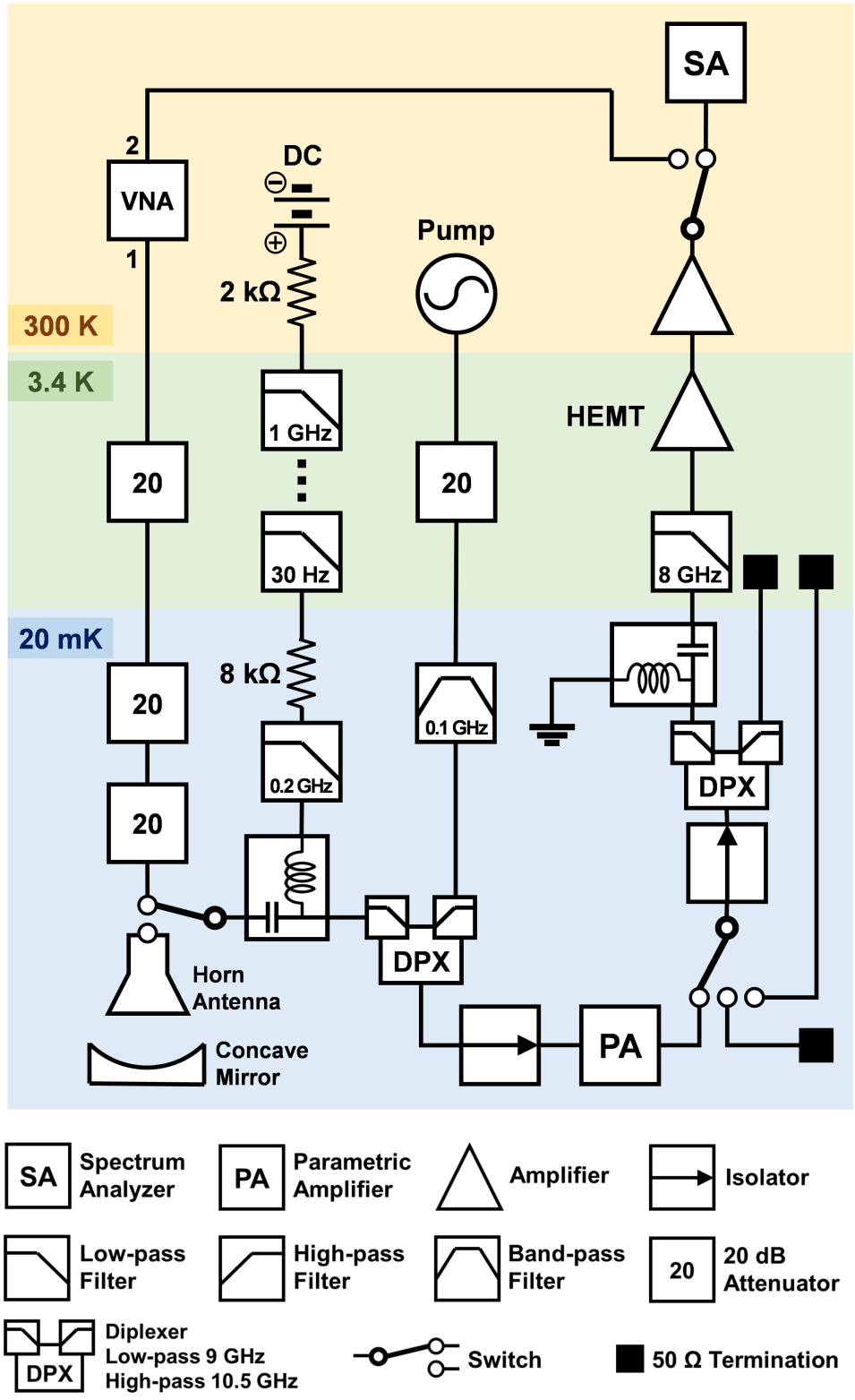

Figure 7.1: A schematic diagram of our hidden photon experimental setup.

the process of improving the modeling of our systematics and hope to produce a published article in the upcoming months. We do not expect further alterations to impact our computed limits on χ by more than a factor of a few.

Our measurement procedure involved four spectrum analyzer measurements: the power emitted by the dish P_{dish}, the power emitted by the reference load P_{ref}, the power emitted by the hot and cold loads after the parametric amplifier (P_H and P_C). The latter three measurements combined with the parametric amplifier gain allow us to refer the spectrum analyzer noise level to the number of noise quanta at the input of the parametric amplifier. This y-factor analysis is identical to that in section 4.4, where it is described in great detail. The resulting calculation is shown in Figure 7.2. The large-scale structure in this result stems from the ripple structure in our system changing as the cold switch after the amplifier is set between the hot load, cold load, and amplifier channels.

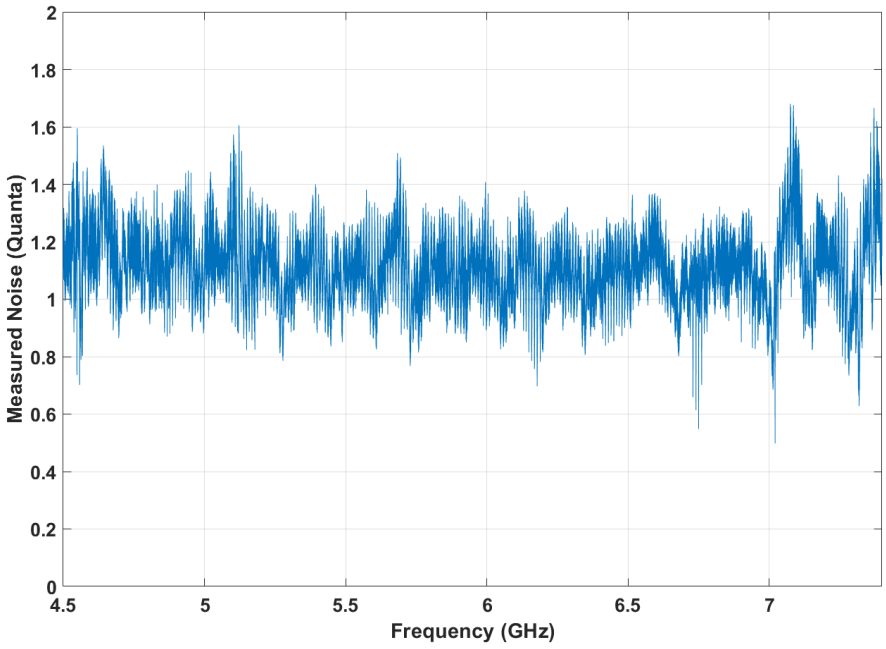

Figure 7.2: The noise in units of quanta referred to the input of the parametric amplifier for the reference measurement of our dark matter search.

Using this calculated value directly would result in an unphysical result at certain frequencies since some fluctuations in the data would place our background level below the combined vacuum fluctuations and quantum limit on parametric amplifier noise.[43] A histogram of the noise result across the frequencies in our experiment

is shown in Figure 7.4. The mean value of this noise at 1.1 quanta is a reasonable estimate for the actual noise level in the system. Instead, we choose to use a very conservative estimate of our noise level to be 3σ above this mean value at $Q_{\text{ref}} = 1.437$ quanta.

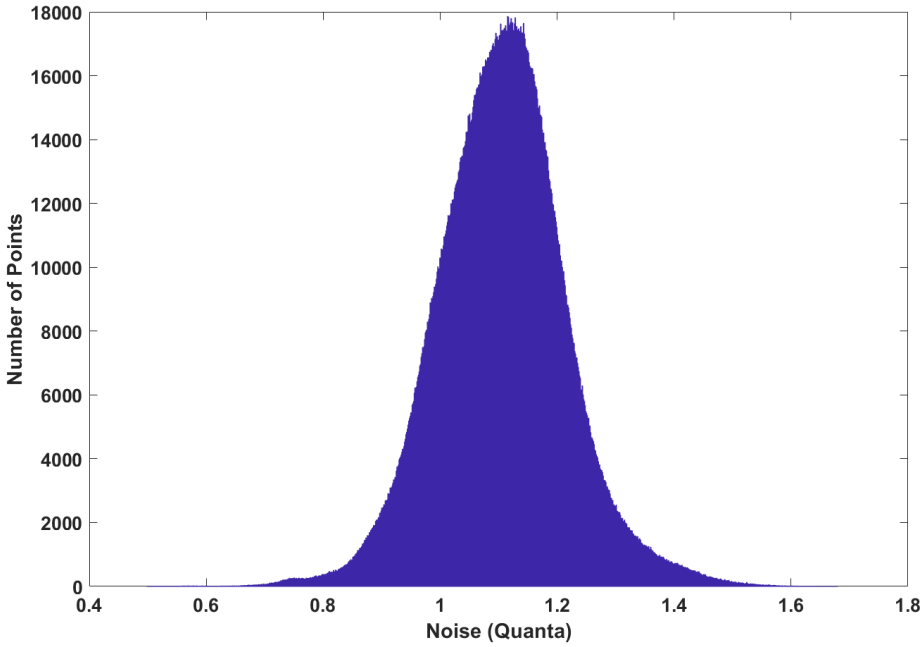

Figure 7.3: A histogram of the measured noise level of our reference load referred to the input of the parametric amplifier within the measurement bandwidth. The mean noise level is 1.106 quanta.

Switching the cold switch at the input of our system between the attenuators and horn antenna also results in a shift of the ripple structure due to the altered path length for the standing wave reflections in our setup. Because these components were connected using a similar length of coaxial cable, the change is relatively minor compared to the effect seen from altering the configuration of the cold switch used in the y-factor measurement. Nonetheless, the different creates a frequency-dependent offset in the residual between the dish data and reference that must be subtracted to detect any excesses corresponding to a dark matter signal.

$$\text{Residual} = Q_{\text{ref}} \frac{P_{\text{dish}} - P_{\text{ref}}}{P_{\text{ref}}} \tag{7.6}$$

The frequency spacing of the ripples is on the order of 8 MHz, so to correct for their shift, we fit a second order polynomial to 500 kHz windows within our data

and subtract it from the result. This process has the additional effect of removing any broad-band background or offset in our measurement. The resulting residual is shown in Figure 7.4, showing fluctuations in our measurement have been averaged to below 0.01 quanta at the input of the parametric amplifier. To ensure that this polynomial subtraction does not impact the reconstruction of our signal, we have performed a simulated signal injection into our data and verified that we are able to recover signals with χ corresponding to our detection limits.

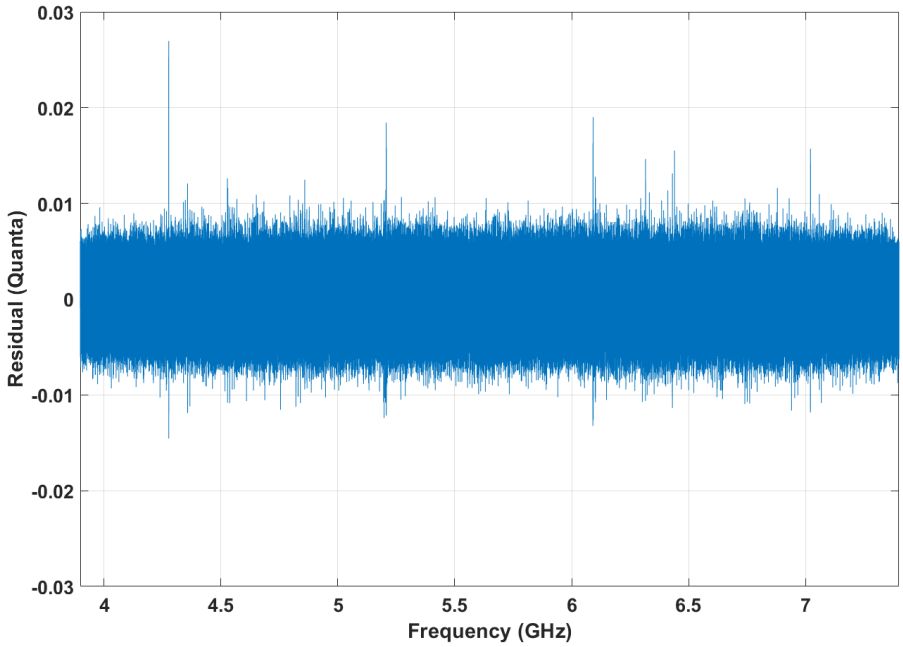

Figure 7.4: The residual, in units of quanta, between the dish and reference load data after correcting for the change in ripple structure.

Because the spectrum analyzer uses overlapping windows as it sweeps the spectrum, the data in bins less than 4 kHz apart is strongly correlated. To remove this correlation, we sum the power of each neighboring set of five bins prior to searching for a hidden photon signal. The frequency ν of the expected hidden photon signal from dark matter with a velocity v will be

$$h\nu = \frac{m_{\gamma'}c^2}{\sqrt{1-(v/c)^2}} \tag{7.7}$$

where the distribution of dark matter velocities can be calculated through

$$F_v(v) = \int_0^v dv' \int^{4\pi} d\Omega f(\mathbf{v}')v'^2$$
$$f(\mathbf{v}) = \frac{1}{(\sqrt{\pi}v_c)^3} \exp\left(-\frac{|\mathbf{v}+\mathbf{v}_c|^2}{v_c^2}\right) \tag{7.8}$$

where $\mathbf{v}$ dark matter velocity and v_c is the velocity of the earth relative to the galactic center.[158] This results in a spread of the signal across frequency as shown in Figure 7.5.

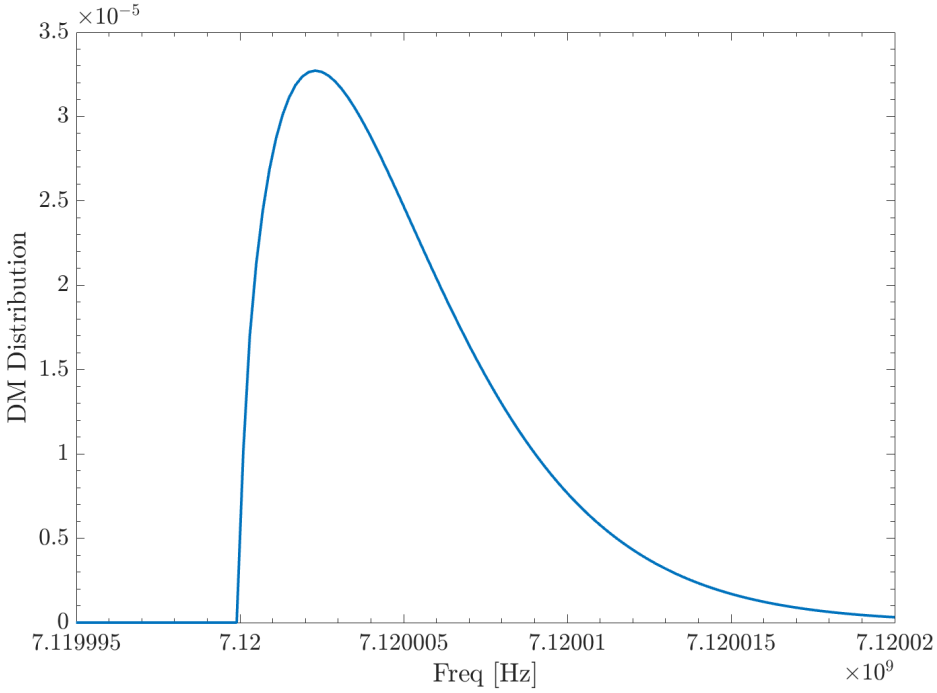

Figure 7.5: An example of the calculated excess signal produced from kinetic mixing to hidden photon dark matter with a rest mass corresponding to 7.12 GHz.

Notably, a mirrored version of this signal with an amplitude ratio of $1 - 1/G_{\text{pa}}$ will also appear at the parametric amplifier's idler frequency as a result of the amplification process. Because this ratio is near unity, any dark matter signal will appear twice within our measurement, effectively doubling our integration time in terms of its signal to noise ratio. The combined signal and idler model is then used to search for excesses as a function of χ within our data according to the expected power given by equation 7.4 and an estimated coupling efficiency through the antenna of 30 percent.

This search is achieved by first generating a signal model for a given frequency, which is then convolved with the experimentally measured flat-top spectrum analyzer response. We then minimize the binned negative log-likelihood LL_{min}, which is modeled taking into account the Poissonian photon noise, with only a single free parameter, the kinetic mixing χ. Using the methodology outlined in other works,[165, 158] we exclude the presence of a signal by comparing the log-likelihood of the no-dark matter model $LL_{\text{no signal}}$ to LL_{min} and accounting for the look elsewhere effect by a Monte Carlo simulation to estimate the number of independent frequency windows for our signal model within our data.

To set the limits on detection, we use the procedure outlined in Tomita et. al. [158] by computing the test-statistic

$$D = 2\,(LL_{\text{model}} - LL_{\text{min}}) \tag{7.9}$$

and calculating the model χ giving LL_{model} which corresponds to a $D = 3.841$, or 95% confidence limit. The resulting 95% confidence limits on χ compared with limits set by other experiments[166] are shown in Figures 7.6 and 7.7.

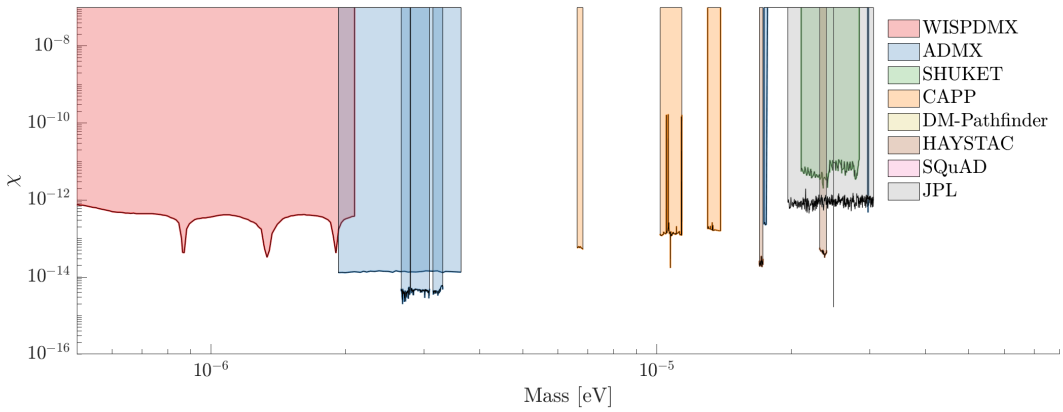

Figure 7.6: 95% confidence limits on the kinetic mixing parameter χ according to our experiment (JPL - gray) and a few selected notable results.

Our search found no presence of a dark matter signal from hidden photons with mass ranges between $1.97 * 10^{-5}$ and $3.05 * 10^{-5}$ eV, excluding a kinetic mixing $\chi < 10^{-12}$ across that frequency range, extending the limits at those frequencies. Considering this result was obtained in less than one day of integration using a significantly smaller dish than could be fit into our cryostat in a cooldown solely dedicated to this experiment, we believe further such experiments would be an extremely fruitful

avenue of pursuit moving forward. In particular, there are very few limits set by other experiments[166] at higher frequencies, so we are eager to someday replicate this experiment using our Ka or W band parametric amplifiers.

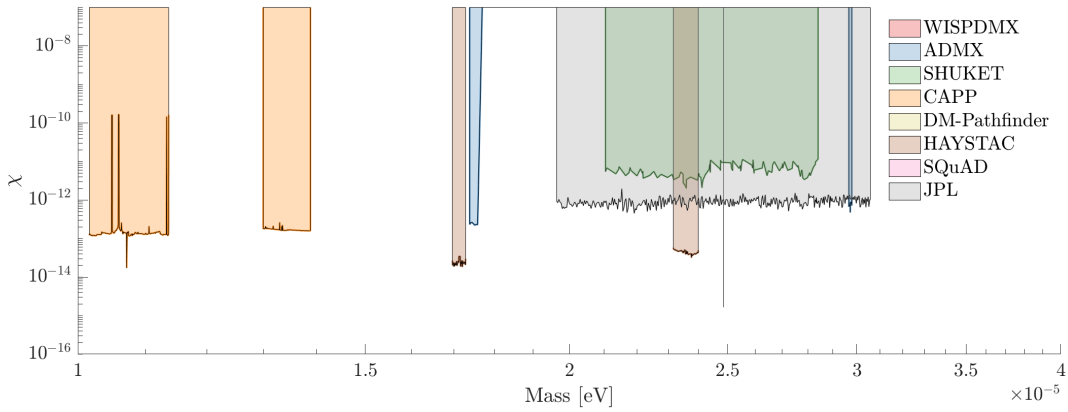

Figure 7.7: 95% confidence limits on the kinetic mixing parameter χ according to our experiment (JPL - gray) and a few selected notable results.

Chapter 8

CONCLUSIONS AND OUTLOOK

In this thesis, we have shown the theoretical and experimental realization of a variety of superconducting devices based on the high nonlinearity of the kinetic inductance in NbTiN microstrip lines. The majority of these devices were traveling wave parametric amplifiers, of both the three-wave-mixing and four-wave-mixing variety, which we have thoroughly characterized for their gain, losses, noise, limits on performance, and applications to other experiments. Operating outside of their designed parameters, we have used some of our amplifiers to demonstrate high-efficiency frequency-converters, and exploited the nonlinearity to develop an on-chip Fourier transform spectrometer.

At low frequencies between 1 and 10 GHz, broadband, low-noise parametric amplifiers are in high demand for multiplexed microwave detector technologies such as MKID arrays. The devices presented in this document have experimentally shown 20-30 dB gain across several GHz of bandwidth within this frequency range, with noise performance at or near the limit set by quantum mechanics. For many practical purposes, our amplifiers are already at a state where they could be integrated into other experimental systems for improved noise performance. One of our amplifiers has already been used to significantly improve the spectral resolution of an MKID array and to reveal further underlying limits to their performance that were previously obscured by readout amplifier noise.[30] We have also used one of our devices to demonstrate nearly 10 dB of vacuum noise squeezing at the half-pump frequency within the squeezed quadrature and sub-half-photon system noise within the amplified quadrature. A two-mode vacuum squeezing measurement using this device has also been completed, but the analysis of those results was not completed in time for their inclusion in this thesis.

We have also presented a particularly promising use case for parametric amplifiers in the read-out system of dish searches for hidden photon dark matter. Parametric amplifiers are particularly useful in such experiments because their gain enables the simultaneous measurement of a large range of hidden photon masses, their excellent noise performance lowers the level of the minimum detectable signal to improve the measurement sensitivity, and the production of the idler tone allows for a correlated

search across two frequencies that further improves the limits set by the experiment. Directly as a result of these advantages, our preliminary analysis indicates that we were able to set new limits on the strength of kinetic mixing ($\chi \sim 10^{-12}$) utilizing only a small dish measured for less than a single day. Considering the ease with which a parametric amplifier noise characterization system can be modified to perform such measurements, we believe that similar experiments would be a fruitful avenue to pursue for anyone with access to similar amplifier.

Building on the success at lower frequencies, we have shown several prototype parametric amplifiers with 15 dB gain operating in the Ka and W bands. The Ka band device was especially notable due to its high bandwidth spanning from 4 to 34 GHz, while the W band device is to our knowledge the first demonstration of a superconducting traveling wave kinetic inductance parametric amplifier for frequencies near 90 GHz. We attempted a y-factor noise characterization of the W band device between 81 and 84.5 GHz but were unable to obtain an accurate result due to transmission losses in the device housing for our best-performing device. Since our measurement system and the amplifier itself appear to be operating nominally, we believe that a full demonstration of a parametric amplifier for millimeter/submillimeter-wave radio telescope receivers is not far on the horizon. Such devices are also of particular interest to the hidden photon dark matter search experiment we have described as the current limits on kinetic mixing are more than an order of magnitude weaker at those frequencies compared to those near 5-7 GHz where we performed our measurement.

Moving forward, reducing reflections is the main area in need of improvement for our parametric amplifiers across all frequencies. In the present state, all of our devices show a significant amount of gain ripple and frequently have gain limited by the formation of runaway parametric oscillation when operated at lower temperatures. These difficulties do not stem solely from the amplifier itself but also the system within which it is operated. Within experiments that allow it, introducing isolators before and after our amplifier to reduce the impact of reflections from other components has yielded a significant improvement in device performance. This problem is quite ubiquitous within the parametric amplifier community and while a number of ingenious ideas have been presented to address it in specific cases[167] solutions to minimize the effects of in-band reflections for purely traveling wave devices are extremely challenging to implement. Barring any major revolutions to device design, one potential approach would be integrating other components

ubiquitous in traveling parametric amplifiers such as bias tees and diplexer into the devices themselves, which could nearly eliminate their contributions to the reflections across the parametric amplifier.

Aside from parametric amplifiers, we have investigated other nonlinear processes occurring in our transmission lines, in particular the up-conversion process. Through careful tuning of pump parameters, we were able to obtain a nearly perfectly efficient up-converter from an low frequency 1.75 GHz signal to an output with over seven times higher frequency and seven times as much power. With further development, such frequency conversion devices could be especially useful for generating local oscillators above 100 GHz or complement technologies such as SIS mixers used in heterodyne receivers.

At optical frequencies, the dispersion of the nonlinear materials is not as easily engineered as in our microwave transmission lines, so the desired characteristics are commonly obtained through quasi-phase-matching where the dispersion is periodically changed along the optical path through materials with different properties. A similar procedure would be trivial to implement in our transmission lines and could be used to modify the dispersion curve to phase-match different parametric processes along different points of the line. One could imagine a device that is driven by a low-frequency pump which is efficiently converted to a >100 GHz tone through harmonic generation, subsequently drives four-wave-mixing amplification for the incident signal, then uses down-conversion to transfer the amplified signal power to lower frequencies for convenient readout. Developing such a device would require impeccable modeling and dispersion engineering, but if realized could replace the nearly the entire readout system of a radio telescope receiver with a single higher-efficiency on-chip device.

BIBLIOGRAPHY

[1] Douglas Scott. "The standard cosmological model." In: *Canadian Journal of Physics* 84.6-7 (Jan. 2006), pp. 419–435. DOI: 10.1139/p06-066. URL: https://doi.org/10.1139%2Fp06-066.

[2] Takuya Hashimoto et al. "The onset of star formation 250 million years after the Big Bang." In: *Nature* 557.7705 (May 2018), pp. 392–395. DOI: 10.1038/s41586-018-0117-z. arXiv: 1805.05966 [astro-ph.GA].

[3] Benjamin D. Boizelle et al. "A Precision Measurement of the Mass of the Black Hole in NGC 3258 from High-resolution ALMA Observations of Its Circumnuclear Disk." In: *The Astrophysical Journal* 881.1, 10 (Aug. 2019), p. 10. DOI: 10.3847/1538-4357/ab2a0a. arXiv: 1906.06267 [astro-ph.GA].

[4] Shogo Tachibana et al. "Spatial Distribution of AlO in a High-mass Protostar Candidate Orion Source I." In: *The Astrophysical Journal* 875.2 (Apr. 2019), p. L29. DOI: 10.3847/2041-8213/ab1653. URL: https://doi.org/10.3847/2041-8213/ab1653.

[5] Giovanni P. Rosotti et al. "Spiral arms in the protoplanetary disc HD100453 detected with ALMA: evidence for binary-disc interaction and a vertical temperature gradient." In: *Monthly Notices of the Royal Astronomical Society* 491.1 (Jan. 2020), pp. 1335–1347. DOI: 10.1093/mnras/stz3090. arXiv: 1911.00518 [astro-ph.EP].

[6] Tomasz Kamiński et al. "Astronomical detection of radioactive molecule ^{26}AlF in the remnant of an ancient explosion." In: *Nature Astronomy* 2 (July 2018), pp. 778–783. DOI: 10.1038/s41550-018-0541-x. arXiv: 1807.10647 [astro-ph.SR].

[7] Samuel E. Gralla, Alexandru Lupsasca, and Daniel P. Marrone. "The shape of the black hole photon ring: A precise test of strong-field general relativity." In: *Physical Review D* 102.12 (Dec. 2020). DOI: 10.1103/physrevd.102.124004. URL: https://doi.org/10.1103%2Fphysrevd.102.124004.

[8] Alexander E. Thelen et al. "Spatial variations in Titan's atmospheric temperature: ALMA and Cassini comparisons from 2012 to 2015." In: *Icarus* 307 (2018), pp. 380–390. ISSN: 0019-1035. DOI: https://doi.org/10.1016/j.icarus.2017.10.042. URL: https://www.sciencedirect.com/science/article/pii/S0019103517305146.

[9] Eric W. Bryerton, Matthew Morgan, and Marian Pospieszalski. "Ultra low noise cryogenic amplifiers for radio astronomy." In: Jan. 2013, pp. 358–360. ISBN: 978-1-4673-2929-3. DOI: 10.1109/RWS.2013.6486740.

[10] John R. Tucker and Marc J. Feldman. "Quantum detection at millimeter wavelengths." In: *Reviews of Modern Physics* 57 (4 Oct. 1985), pp. 1055–1113. DOI: 10.1103/RevModPhys.57.1055. URL: https://link.aps.org/doi/10.1103/RevModPhys.57.1055.

[11] Michael Wengler and David Woody. "Quantum noise in heterodyne detection." In: *IEEE Journal of Quantum Electronics* 23.5 (1987), pp. 613–622. DOI: 10.1109/JQE.1987.1073387.

[12] Marian W. Pospieszalski. "Cryogenic amplifiers for Jansky Very Large Array receivers." In: *2012 19th International Conference on Microwaves, Radar Wireless Communications*. Vol. 2. 2012, pp. 748–751. DOI: 10.1109/MIKON.2012.6233589.

[13] Anthony R. Kerr et al. "Development of the ALMA Band-3 and Band-6 Sideband-Separating SIS Mixers." In: *IEEE Transactions on Terahertz Science and Technology* 4.2 (Mar. 2014), pp. 201–212. DOI: 10.1109/TTHZ.2014.2302537.

[14] Frank Randolph III Rice. "A Very Wide Bandwidth SIS Heterodyne Receiver Design for Millimeter and Submillimeter Astronomy." Dissertation (Ph.D.) California Institute of Technology, 2021. URL: https://resolver.caltech.edu/CaltechTHESIS:09062020-111601302.

[15] Cheuk-yu Edward Tong et al. "Ultra-wide IF bandwidth — The next frontier for SIS receivers." In: *2015 IEEE MTT-S International Microwave Symposium*. 2015, pp. 1–4. DOI: 10.1109/MWSYM.2015.7166804.

[16] Anthony R. Kerr et al. "ALMA Band 6v2 SIS Mixer-Preamp Development." In: (2022). URL: https://science.nrao.edu/facilities/alma/science_sustainability/copy_of_Cycle8CloseOutReport02b1.pdf.

[17] John Carpenter et al. "The ALMA Development Program: Roadmap to 2030." In: (2020). DOI: 10.48550/ARXIV.2001.11076. URL: https://arxiv.org/abs/2001.11076.

[18] National Research Council. *Panel Reports—New Worlds, New Horizons in Astronomy and Astrophysics*. Washington, DC: The National Academies Press, 2011. ISBN: 978-0-309-15962-3. DOI: 10.17226/12982. URL: https://nap.nationalacademies.org/catalog/12982/panel-reports-new-worlds-new-horizons-in-astronomy-and-astrophysics.

[19] Peter Day et al. "A broadband superconducting detector suitable for use in large arrays." In: *Nature* 425 (Oct. 2003), pp. 817–21. DOI: 10.1038/nature02037.

[20] Philip R. Maloney et al. "The MKID Camera." In: *The Thirteenth International Workshop on Low Temperature Detectors - LTD13*. Ed. by Betty Young, Blas Cabrera, and Aaron Miller. Vol. 1185. American Institute of

Physics Conference Series. Dec. 2009, pp. 176–179. DOI: 10.1063/1.3292309.

[21] Steven Hailey-Dunsheath et al. "Kinetic inductance detectors for the Origins Space Telescope." In: *Journal of Astronomical Telescopes, Instruments, and Systems* 7, 011015 (Jan. 2021), p. 011015. DOI: 10.1117/1.JATIS.7.1.011015.

[22] Alex Walter et al. "MEC: the MKID exoplanet camera for high contrast astronomy at Subaru (Conference Presentation)." In: July 2018, p. 31. DOI: 10.1117/12.2311586.

[23] Paul Szypryt et al. "Large-format platinum silicide microwave kinetic inductance detectors for optical to near-IR astronomy." In: *Optics Express* 25.21 (Oct. 2017), pp. 25894–25909. DOI: 10.1364/OE.25.025894. URL: http://opg.optica.org/oe/abstract.cfm?URI=oe-25-21-25894.

[24] Seth R. Meeker et al. "DARKNESS: A Microwave Kinetic Inductance Detector Integral Field Spectrograph for High-contrast Astronomy." In: *Publications of the Astronomical Society of the Pacific* 130.988 (Apr. 2018), p. 065001. DOI: 10.1088/1538-3873/aab5e7. URL: https://doi.org/10.1088%2F1538-3873%2Faab5e7.

[25] Shibo Shu et al. *A multi-chroic kinetic inductance detectors array using hierarchical phased array antenna*. 2021. DOI: 10.48550/ARXIV.2112.05366. URL: https://arxiv.org/abs/2112.05366.

[26] Peter Day et al. "A broadband superconducting detector suitable for use in large arrays." In: *Nature* 425 (Oct. 2003), pp. 817–21. DOI: 10.1038/nature02037.

[27] Nicholas Zobrist et al. "Improving the dynamic range of single photon counting kinetic inductance detectors." In: *Journal of Astronomical Telescopes, Instruments, and Systems* 7, 010501 (Jan. 2021), p. 010501. DOI: 10.1117/1.JATIS.7.1.010501. arXiv: 2012.05192 [astro-ph.IM].

[28] Antonino Miceli et al. "Towards X-ray Thermal Kinetic Inductance Detectors." In: *Journal of Low Temperature Physics* 176 (Aug. 2014). DOI: 10.1007/s10909-013-1033-0.

[29] Jonas Zmuidzinas. "Superconducting Microresonators: Physics and Applications." In: *Annual Review of Condensed Matter Physics* 3.1 (2012), pp. 169–214. DOI: 10.1146/annurev-conmatphys-020911-125022. eprint: https://doi.org/10.1146/annurev-conmatphys-020911-125022. URL: https://doi.org/10.1146/annurev-conmatphys-020911-125022.

[30] Nicholas Zobrist et al. "Wide-band parametric amplifier readout and resolution of optical microwave kinetic inductance detectors." In: *Applied Physics Letters* 115.4 (July 2019), p. 042601. DOI: 10.1063/1.5098469. URL: https://doi.org/10.1063%2F1.5098469.

[31] Benjamin A. Mazin et al. “Digital readouts for large microwave low-temperature detector arrays.” In: *Nuclear Instruments and Methods in Physics Research A* 559.2 (Apr. 2006), pp. 799–801. DOI: 10.1016/j.nima.2005.12.208.

[32] Sean McHugh et al. “A readout for large arrays of microwave kinetic inductance detectors.” In: *Review of Scientific Instruments* 83.4 (Apr. 2012), p. 044702. DOI: 10.1063/1.3700812. URL: https://doi.org/10.1063%2F1.3700812.

[33] Harald T. Friis. “Noise Figures of Radio Receivers.” In: *Proceedings of the IRE* 32.7 (1944), pp. 419–422. DOI: 10.1109/JRPROC.1944.232049.

[34] Ernst F. W. Alexanderson and Samuel P. Nixdorff. “A Magnetic Amplifier for Radio Telephony.” In: *Proceedings of the Institute of Radio Engineers* 4.2 (1916), pp. 101–120. DOI: 10.1109/JRPROC.1916.217224.

[35] Ralph V. L. Hartley. “Oscillations in systems with non-linear reactance.” In: *The Bell System Technical Journal* 15.3 (1936), pp. 424–440. DOI: 10.1002/j.1538-7305.1936.tb03559.x.

[36] John William Planinac. “An Investigation of Junction Diode Parametric Amplifiers at Medium Radio Frequencies.” Master of Science. Oklahoma State University, 1960. URL: https://shareok.org/bitstream/handle/11244/30976/Thesis-1960-P712i.pdf.

[37] Ronald E. Burgess. “Low noise possibilities of certain semiconductor amplifying systems.” In: *Solid-State Electronics* 4 (1962), pp. 25–30. ISSN: 0038-1101. DOI: https://doi.org/10.1016/0038-1101(62)90068-0. URL: https://www.sciencedirect.com/science/article/pii/0038110162900680.

[38] Sander Weinreb. “Low-Noise Cooled GASFET Amplifiers.” In: *IEEE Transactions on Microwave Theory and Techniques* 28.10 (1980), pp. 1041–1054. DOI: 10.1109/TMTT.1980.1130223.

[39] Sander Weinreb, Dan L. Fenstermacher, and Ronald W. Harris. “Ultra-Low-Noise 1.2- to 1.7-GHz Cooled GaAsFET Amplifiers.” In: *IEEE Transactions on Microwave Theory and Techniques* 30.6 (1982), pp. 849–853. DOI: 10.1109/TMTT.1982.1131159.

[40] Takashi Mimura. “The early history of the high electron mobility transistor (HEMT).” In: *IEEE Transactions on Microwave Theory and Techniques* 50.3 (2002), pp. 780–782. DOI: 10.1109/22.989961.

[41] Marian W. Pospieszalski et al. “FETs and HEMTs at cryogenic temperatures-their properties and use in low-noise amplifiers.” In: *IEEE Transactions on Microwave Theory and Techniques* 36.3 (1988), pp. 552–560. DOI: 10.1109/22.3548.

[42] Lisa A Tracy et al. "MilliKelvin HEMT Amplifiers for Low Noise High Bandwidth Measurement of Quantum Devices." In: (Sept. 2018). DOI: 10.2172/1471452. URL: https://www.osti.gov/biblio/1471452.

[43] Carlton M. Caves. "Quantum limits on noise in linear amplifiers." In: *Physics Review D* 26 (8 Oct. 1982), pp. 1817–1839. DOI: 10.1103/PhysRevD.26.1817. URL: https://link.aps.org/doi/10.1103/PhysRevD.26.1817.

[44] Chris Macklin et al. "A near quantum-limited Josephson traveling-wave parametric amplifier." In: *Science* 350.6258 (2015), pp. 307–310. DOI: 10.1126/science.aaa8525. eprint: https://www.science.org/doi/pdf/10.1126/science.aaa8525. URL: https://www.science.org/doi/abs/10.1126/science.aaa8525.

[45] William W. Mumford. "Some Notes on the History of Parametric Transducers." In: *Proceedings of the IRE* 48.5 (1960), pp. 848–853. DOI: 10.1109/JRPROC.1960.287620.

[46] Ping K. Tien. "Parametric Amplification and Frequency Mixing in Propagating Circuits." In: *Journal of Applied Physics* 29.9 (Sept. 1958), pp. 1347–1357. DOI: 10.1063/1.1723440.

[47] Rolf Landauer. "Shock Waves in Nonlinear Transmission Lines and Their Effect on Parametric Amplification." In: *IBM Journal of Research and Development* 4.4 (Oct. 1960), pp. 391–401. ISSN: 0018-8646. DOI: 10.1147/rd.44.0391. URL: https://doi.org/10.1147/rd.44.0391.

[48] Richard A. Connell. "Parametric amplification in thin film superconducting transmission lines." In: *Proceedings of the IEEE* 51.4 (1963), pp. 616–617. DOI: 10.1109/PROC.1963.2227.

[49] Alvin S. Clorfeine. "Microwave amplification with superconductors." In: *Proceedings of the IEEE* 52.7 (1964), pp. 844–845. DOI: 10.1109/PROC.1964.3130.

[50] Hildebrand Zimmer. "PARAMETRIC AMPLIFICATION OF MICROWAVES IN SUPERCONDUCTING JOSEPHSON TUNNEL JUNCTIONS." In: *Applied Physics Letters* 10 (Jan. 1967). DOI: 10.1063/1.1754906. URL: https://www.osti.gov/biblio/4434336.

[51] Andrew Smith et al. "Low noise microwave parametric amplifier." In: *IEEE Transactions on Magnetics* 21.2 (1985), pp. 1022–1028. DOI: 10.1109/TMAG.1985.1063665.

[52] Bernard Yurke et al. "Observation of parametric amplification and deamplification in a Josephson parametric amplifier." In: *Physical Review A* 39 (5 Mar. 1989), pp. 2519–2533. DOI: 10.1103/PhysRevA.39.2519. URL: https://link.aps.org/doi/10.1103/PhysRevA.39.2519.

[53] Erik A. Tholén et al. "Nonlinearities and parametric amplification in superconducting coplanar waveguide resonators." In: *Applied Physics Letters* 90.25 (2007), p. 253509. DOI: 10.1063/1.2750520. eprint: https://doi.org/10.1063/1.2750520. URL: https://doi.org/10.1063/1.2750520.

[54] Martina Esposito et al. "Perspective on traveling wave microwave parametric amplifiers." In: *Applied Physics Letters* 119.12 (2021), p. 120501. DOI: 10.1063/5.0064892. eprint: https://doi.org/10.1063/5.0064892. URL: https://doi.org/10.1063/5.0064892.

[55] Jonas Hansryd and Peter A. Andrekson. "Broad-band continuous-wave-pumped fiber optical parametric amplifier with 49-dB gain and wavelength-conversion efficiency." In: *IEEE Photonics Technology Letters* 13.3 (2001), pp. 194–196. DOI: 10.1109/68.914318.

[56] Byeong Ho Eom et al. "A wideband, low-noise superconducting amplifier with high dynamic range." In: *Nature Physics* 8 (2012), pp. 623–627. URL: https://doi.org/10.1038/nphys2356.

[57] Ted C. White et al. *Traveling wave parametric amplifier with Josephson junctions using minimal resonator phase matching*. 2015. DOI: 10.48550/ARXIV.1503.04364. URL: https://arxiv.org/abs/1503.04364.

[58] David J. Griffiths. *Introduction to Electrodynamics*. 4th ed. Cambridge University Press, 2017. DOI: 10.1017/9781108333511.

[59] Michael Tinkham. *Introduction to Superconductivity*. Dover Books on Physics Series. Dover Publications, 2004. ISBN: 9780486134727.

[60] Anthony J Annunziata et al. "Tunable superconducting nanoinductors." In: *Nanotechnology* 21.44 (Oct. 2010), p. 445202. DOI: 10.1088/0957-4484/21/44/445202. URL: https://doi.org/10.1088%2F0957-4484%2F21%2F44%2F445202.

[61] Uwe S. Pracht et al. "Electrodynamics of the Superconducting State in Ultra-Thin Films at THz Frequencies." In: *IEEE Transactions on Terahertz Science and Technology* 3.3 (May 2013), pp. 269–280. DOI: 10.1109/tthz.2013.2255047. URL: https://doi.org/10.1109%2Ftthz.2013.2255047.

[62] Alexander V. Semenov et al. "Effect of Microwaves on Superconductors for Kinetic Inductance Detection and Parametric Amplification." In: *Physical Review Applied* 13 (2 Feb. 2020), p. 024079. DOI: 10.1103/PhysRevApplied.13.024079. URL: https://link.aps.org/doi/10.1103/PhysRevApplied.13.024079.

[63] Maxime Malnou et al. "Three-Wave Mixing Kinetic Inductance Traveling-Wave Amplifier with Near-Quantum-Limited Noise Performance." In: *PRX Quantum* 2 (1 Jan. 2021), p. 010302. DOI: 10.1103/PRXQuantum.2.010302. URL: https://link.aps.org/doi/10.1103/PRXQuantum.2.010302.

[64] Shibo Shu et al. “Nonlinearity and wide-band parametric amplification in a (Nb,Ti)N microstrip transmission line.” In: *Physical Review Research* 3.2 (June 2021). DOI: 10.1103/physrevresearch.3.023184. URL: https://doi.org/10.1103%2Fphysrevresearch.3.023184.

[65] Robert P. Erickson and David P. Pappas. “Theory of multiwave mixing within the superconducting kinetic-inductance traveling-wave amplifier.” In: *Phys. Rev. B* 95 (10 Mar. 2017), p. 104506. DOI: 10.1103/PhysRevB.95.104506. URL: https://link.aps.org/doi/10.1103/PhysRevB.95.104506.

[66] Ralf Pöpel. “Exact solutions of the Mattis Bardeen theory for thin superconducting films and bulk material.” In: *IEEE Transactions on Magnetics* 27.2 (1991), pp. 1306–1309. DOI: 10.1109/20.133424.

[67] Daniel C. Mattis and John Bardeen. “Theory of the Anomalous Skin Effect in Normal and Superconducting Metals.” In: *Physical Review* 111 (2 July 1958), pp. 412–417. DOI: 10.1103/PhysRev.111.412. URL: https://link.aps.org/doi/10.1103/PhysRev.111.412.

[68] Max Born et al. *Principles of Optics: Electromagnetic Theory of Propagation, Interference and Diffraction of Light*. 7th ed. Cambridge University Press, 1999. DOI: 10.1017/CBO9781139644181.

[69] Saddok Senouci. “A Study of Periodic Microstrip Structures Using Finite Elementary Lines (FEL) Approach.” In: *American Journal of Physics and Applications* 5 (Jan. 2017), p. 52. DOI: 10.11648/j.ajpa.20170504.12.

[70] John D. Joannopoulos et al. *Photonic Crystals: Molding the Flow of Light*. 2nd. USA: Princeton University Press, 2008. ISBN: 0691124566. URL: http://ab-initio.mit.edu/book/photonic-crystals-book.pdf.

[71] Anthony R. Kerr, Mark J. Feldman, and Shing-Kuo Pan. “Receiver Noise Temperature, the Quantum Noise Limit, and the Role of the Zero-Point Fluctuations.” In: *Eighth International Symposium on Space Terahertz Technology*. Ed. by Raymond Blundell and Edward Tong. Jan. 1997, pp. 101–111. URL: https://library.nrao.edu/public/memos/alma/memo161.pdf.

[72] Maxime Malnou et al. *Performance of a Kinetic-Inductance Traveling-Wave Parametric Amplifier at 4 Kelvin: Toward an Alternative to Semiconductor Amplifiers*. 2021. DOI: 10.48550/ARXIV.2110.08142. URL: https://arxiv.org/abs/2110.08142.

[73] Peter W. Anderson, B. I. Halperin, and C. M. Varma. “Anomalous low-temperature thermal properties of glasses and spin glasses.” In: *Philosophical Magazine* 25.1 (Jan. 1972), pp. 1–9. DOI: 10.1080/14786437208229210.

[74] William A. Phillips. “Tunneling states in amorphous solids.” In: *Journal of Low Temperature Physics* 7 (1972), pp. 351–360. URL: https://link.springer.com/article/10.1007/BF00660072.

[75] William A. Phillips. “Two-level states in glasses.” In: *Reports on Progress in Physics* 50.12 (Dec. 1987), pp. 1657–1708. DOI: 10.1088/0034-4885/50/12/003. URL: https://doi.org/10.1088/0034-4885/50/12/003.

[76] John M. Martinis et al. “Decoherence in Josephson Qubits from Dielectric Loss.” In: *Physical Review Letters* 95.21 (Nov. 2005). DOI: 10.1103/physrevlett.95.210503. URL: https://doi.org/10.1103%2Fphysrevlett.95.210503.

[77] Jiansong Gao et al. “Experimental evidence for a surface distribution of two-level systems in superconducting lithographed microwave resonators.” In: *Applied Physics Letters* 92.15 (Apr. 2008), p. 152505. DOI: 10.1063/1.2906373. URL: https://doi.org/10.1063%2F1.2906373.

[78] Aaron D. O’Connell et al. “Microwave dielectric loss at single photon energies and millikelvin temperatures.” In: *Applied Physics Letters* 92.11 (Mar. 2008), p. 112903. DOI: 10.1063/1.2898887. URL: https://doi.org/10.1063%2F1.2898887.

[79] Sunil Golwala et al. *RF Loss Tangent and Two-Level-System Noise of Amorphous Silicon and Crystalline Silicon Dielectrics for Sub/mm Astronomy Applications*. https://agenda.infn.it/event/15448/contributions/95858/attachments/65827/80272/180716GolwalaLTD18Dielectric.pdf. 2019.

[80] Anne Anthore, Hugues Pothier, and Daniel Esteve. “Density of States in a Superconductor Carrying a Supercurrent.” In: *Physical Review Letters* 90.12 (Mar. 2003). DOI: 10.1103/physrevlett.90.127001. URL: https://doi.org/10.1103%2Fphysrevlett.90.127001.

[81] Songyuan Zhao et al. “Nonlinear Properties of Supercurrent-Carrying Single- and Multi-Layer Thin-Film Superconductors.” In: *Journal of Low Temperature Physics* 199.1-2 (Jan. 2020), pp. 34–44. DOI: 10.1007/s10909-019-02306-3. URL: https://doi.org/10.1007%2Fs10909-019-02306-3.

[82] Eric Hammerstad and Ole Jensen. “Accurate Models for Microstrip Computer-Aided Design.” In: *1980 IEEE MTT-S International Microwave symposium Digest*. 1980, pp. 407–409. DOI: 10.1109/MWSYM.1980.1124303.

[83] Harold A. Wheeler. “Transmission-Line Properties of a Strip on a Dielectric Sheet on a Plane.” In: *IEEE Transactions on Microwave Theory and Techniques* 25.8 (1977), pp. 631–647. DOI: 10.1109/TMTT.1977.1129179.

[84] William J. Getsinger. "Microstrip Dispersion Model." In: *IEEE Transactions on Microwave Theory and Techniques* 21.1 (1973), pp. 34–39. DOI: 10.1109/TMTT.1973.1127911.

[85] Judea Pearl. "Vortex Theory of Superconductive Memories." Dissertation (Ph.D.) Polytechnic Institute of Brooklyn, Jan. 1965. URL: https://www.osti.gov/biblio/4562822.

[86] Terence Charles Edwards and Michael Bernard Steer. "Appendix A: Transmission Line Theory." In: *Foundations of Interconnect and Microstrip Design*. John Wiley & Sons, Ltd, 2000, pp. 435–447. ISBN: 9781118894514. DOI: https://doi.org/10.1002/9781118894514.app1. eprint: https://onlinelibrary.wiley.com/doi/pdf/10.1002/9781118894514.app1. URL: https://onlinelibrary.wiley.com/doi/abs/10.1002/9781118894514.app1.

[87] Rolf Landauer. "Shock Waves in Nonlinear Transmission Lines and Their Effect on Parametric Amplification." In: *IBM Journal of Research and Development* 4.4 (1960), pp. 391–401. DOI: 10.1147/rd.44.0391.

[88] S. Chaudhuri et al. "Broadband parametric amplifiers based on nonlinear kinetic inductance artificial transmission lines." In: *Applied Physics Letters* 110.15 (Apr. 2017), p. 152601. DOI: 10.1063/1.4980102. URL: https://doi.org/10.1063%2F1.4980102.

[89] Robert W. Boyd. "Chapter 2 - Wave-Equation Description of Nonlinear Optical Interactions." In: *Nonlinear Optics (Third Edition)*. Ed. by Robert W. Boyd. Third Edition. Burlington: Academic Press, 2008, pp. 69–133. ISBN: 978-0-12-369470-6. DOI: https://doi.org/10.1016/B978-0-12-369470-6.00002-2. URL: https://www.sciencedirect.com/science/article/pii/B9780123694706000022.

[90] Kitti Ratter and Boon-Kok Tan. "A dispersion-engineered Josephson travelling wave parametric amplifier with periodic impedance perturbation." In: (2020). URL: https://www.nrao.edu/meetings/isstt/papers/2020/2020000051.pdf.

[91] Alexander V. Semenov et al. "Coherent Excited States in Superconductors due to a Microwave Field." In: *Physical Review Letters* 117.4 (July 2016). DOI: 10.1103/physrevlett.117.047002. URL: https://doi.org/10.1103%2Fphysrevlett.117.047002.

[92] Govind P. Agrawal. "Chapter 10 - Four-wave mixing." In: *Nonlinear Fiber Optics (Sixth Edition)*. Ed. by Govind P. Agrawal. Sixth Edition. Academic Press, 2019, pp. 401–462. ISBN: 978-0-12-817042-7. DOI: https://doi.org/10.1016/B978-0-12-817042-7.00017-8. URL: https://www.sciencedirect.com/science/article/pii/B9780128170427000178.

[93] Clinton Bockstiegel et al. "Development of a Broadband NbTiN Traveling Wave Parametric Amplifier for MKID Readout." In: *Journal of Low Temperature Physics* 176 (Aug. 2014), pp. 1–7. DOI: 10.1007/s10909-013-1042-z.

[94] Songyuan Zhao et al. "Loss and saturation in superconducting travelling-wave parametric amplifiers." In: *Journal of Physics D: Applied Physics* 52.41 (July 2019), p. 415301. DOI: 10.1088/1361-6463/ab3236. URL: https://doi.org/10.1088%2F1361-6463%2Fab3236.

[95] Slaven Moro et al. "Phase noise in fiber-optic parametric amplifiers and converters and its impact on sensing and communication systems." In: *Optics Express* 18.20 (Sept. 2010), pp. 21449–21460. DOI: 10.1364/OE.18.021449. URL: http://opg.optica.org/oe/abstract.cfm?URI=oe-18-20-21449.

[96] *Datasheet LNF-LNC0.3 14A*. Low Noise Factory. Mar. 2022. URL: https://lownoisefactory.com/wp-content/uploads/2022/03/lnf-lnc0-3_14a.pdf.

[97] *Wideband Amplifier ZVA-183-S+ Datasheet*. Mini-Circuits. Apr. 2022. URL: https://www.minicircuits.com/pdfs/ZVA-183-S+.pdf.

[98] *SM200A/B/C Spectrum Analyzer Product Manual*. Signal Hound. Apr. 2020. URL: https://signalhound.com/sigdownloads/SM200A/SM200-User-Manual.pdf.

[99] Harry Nyquist. "Thermal Agitation of Electric Charge in Conductors." In: *Physical Review* 32.1 (July 1928), pp. 110–113. DOI: 10.1103/PhysRev.32.110.

[100] Herbert B. Callen and Theodore A. Welton. "Irreversibility and Generalized Noise." In: *Physical Review* 83 (1 July 1951), pp. 34–40. DOI: 10.1103/PhysRev.83.34. URL: https://link.aps.org/doi/10.1103/PhysRev.83.34.

[101] Daniel V. Schroeder. *An Introduction to Thermal Physics*. Addison Wesley, 1999. ISBN: 9780201380279.

[102] Daniel J. Parker et al. "Degenerate Parametric Amplification via Three-Wave Mixing Using Kinetic Inductance." In: *Physical Review Applied* 17.3 (Mar. 2022). DOI: 10.1103/physrevapplied.17.034064. URL: https://doi.org/10.1103%2Fphysrevapplied.17.034064.

[103] Manuel A. Castellanos-Beltran et al. "Amplification and squeezing of quantum noise with a tunable Josephson metamaterial." In: *Nature Physics* 4.12 (Oct. 2008), pp. 929–931. DOI: 10.1038/nphys1090. URL: https://doi.org/10.1038%2Fnphys1090.

[104] Bernard Yurke. "Squeezed-state generation using a Josephson parametric amplifier." In: *J. Opt. Soc. Am. B* 4.10 (Oct. 1987), pp. 1551–1557. DOI: 10.1364/JOSAB.4.001551. URL: http://opg.optica.org/josab/abstract.cfm?URI=josab-4-10-1551.

[105] Klaus D. Usadel. "Generalized Diffusion Equation for Superconducting Alloys." In: *Phys. Rev. Lett.* 25 (8 Aug. 1970), pp. 507–509. DOI: 10.1103/PhysRevLett.25.507. URL: https://link.aps.org/doi/10.1103/PhysRevLett.25.507.

[106] Sang Boo Nam. "Theory of Electromagnetic Properties of Strong-Coupling and Impure Superconductors. II." In: *Phys. Rev.* 156 (2 Apr. 1967), pp. 487–493. DOI: 10.1103/PhysRev.156.487. URL: https://link.aps.org/doi/10.1103/PhysRev.156.487.

[107] Songyuan Zhao et al. "Nonlinear Properties of Supercurrent-Carrying Single- and Multi-Layer Thin-Film Superconductors." In: *Journal of Low Temperature Physics* 199.1-2 (Jan. 2020), pp. 34–44. DOI: 10.1007/s10909-019-02306-3. URL: https://doi.org/10.1007%2Fs10909-019-02306-3.

[108] Eduard F. C. Driessen et al. "Strongly Disordered TiN and NbTiN *s*-Wave Superconductors Probed by Microwave Electrodynamics." In: *Phys. Rev. Lett.* 109 (10 Sept. 2012), p. 107003. DOI: 10.1103/PhysRevLett.109.107003. URL: https://link.aps.org/doi/10.1103/PhysRevLett.109.107003.

[109] James G. Kroll et al. "Magnetic-Field-Resilient Superconducting Coplanar-Waveguide Resonators for Hybrid Circuit Quantum Electrodynamics Experiments." In: *Physical Review Applied* 11.6 (June 2019). DOI: 10.1103/physrevapplied.11.064053. URL: https://doi.org/10.1103%2Fphysrevapplied.11.064053.

[110] Reinhold Ludwig and Gene Bogdanov. *RF Circuit Design: Theory and Applications*. Pearson international edition. Prentice-Hall, 2009. ISBN: 9780131471375. URL: https://books.google.com/books?id=GTM2i6ZFpIEC.

[111] Dong K. Shin. *Deep Space Network: Frequency and Channel Assignments*. Jet Propulsion Laboratory. Sept. 2020. URL: https://deepspace.jpl.nasa.gov/dsndocs/810-005/201/201D.pdf.

[112] Danielius Banys et al. *Millimetre Wave Kinetic Inductance Parametric Amplification using Ridge Gap Waveguide*. 2021. DOI: 10.48550/ARXIV.2111.06416. URL: https://arxiv.org/abs/2111.06416.

[113] Anthony R. Kerr et al. "Development of the ALMA Band-3 and Band-6 Sideband-Separating SIS Mixers." In: *IEEE Transactions on Terahertz Science and Technology* 4.2 (2014), pp. 201–212. DOI: 10.1109/TTHZ.2014.2302537.

[114] Yulung Tang et al. "Cryogenic W-band LNA for ALMA band 2+3 with average noise temperature of 24 K." In: *2017 IEEE MTT-S International Microwave Symposium (IMS)*. 2017, pp. 176–179. DOI: 10.1109/MWSYM.2017.8058981.

[115] Alexander Anferov et al. "Millimeter-Wave Four-Wave Mixing via Kinetic Inductance for Quantum Devices." In: *Physical Review Applied* 13.2 (Feb. 2020). DOI: 10.1103/physrevapplied.13.024056. URL: https://doi.org/10.1103%2Fphysrevapplied.13.024056.

[116] *QMC-MX6-10F10*. Quantum Microwave. URL: https://quantummicrowave.com/wp-content/uploads/2017/03/QMC-MX6-10F10-2.pdf.

[117] *90.0 – 94.0 GHz Waveguide Band Pass Filter*. Quantum Microwave. URL: https://quantummicrowave.com/wp-content/uploads/2020/04/QMC-BPF10-9204.pdf.

[118] *W-Band Low Noise Amplifier, 20 dB Gain, 5 dB NF*. SAGE Millimeter Inc. URL: https://sftp.eravant.com/content/datasheets/SBL-7531142050-1010-E1.pdf.

[119] Mikko Varonen et al. "A 75–116-GHz LNA with 23-K noise temperature at 108 GHz." In: *2013 IEEE MTT-S International Microwave Symposium Digest (MTT)*. 2013, pp. 1–3. DOI: 10.1109/MWSYM.2013.6697595.

[120] Thijs de Graauw et al. "The Herschel-Heterodyne Instrument for the Far-Infrared (HIFI)*." In: *A&A* 518 (2010), p. L6. DOI: 10.1051/0004-6361/201014698. URL: https://doi.org/10.1051/0004-6361/201014698.

[121] John C. Mather et al. "Measurement of the Cosmic Microwave Background Spectrum by the COBE FIRAS Instrument." In: *The Astrophysical Physics Journal* 420 (Jan. 1994), p. 439. DOI: 10.1086/173574.

[122] James B. Dent, Damien A. Easson, and Hiroyuki Tashiro. "Cosmological constraints from CMB distortion." In: *Physical Review D* 86 (2012), p. 023514. DOI: 10.1103/PhysRevD.86.023514. arXiv: 1202.6066 [astro-ph.CO].

[123] Paul Murdin. *Encyclopedia of Astronomy & Astrophysics*. 1st ed. Boca Raton, 2000. ISBN: 9781003220435.

[124] Bradford A. Benson et al. "SPT-3G: A Next-Generation Cosmic Microwave Background Polarization Experiment on the South Pole Telescope." In: *Proceedings of SPIE.* 9153 (2014), 91531P. DOI: 10.1117/12.2057305. arXiv: 1407.2973 [astro-ph.IM].

[125] Steven Hailey-Dunsheath et al. "Status of SuperSpec: a broadband, on-chip millimeter-wave spectrometer." In: *Millimeter, Submillimeter, and Far-Infrared Detectors and Instrumentation for Astronomy VII*. Vol. 9153. SPIE Conference Proceedings. Aug. 2014, 91530M, p. 91530M. DOI: 10.1117/12.2057229. arXiv: 1501.02295 [astro-ph.IM].

[126] James A. Grayson et al. "BICEP3 performance overview and planned Keck Array upgrade." In: *Millimeter, Submillimeter, and Far-Infrared Detectors and Instrumentation for Astronomy VIII*. Vol. 9914. SPIE Conference Proceedings. July 2016, 99140S, 99140S. DOI: 10.1117/12.2233894. arXiv: 1607.04668 [astro-ph.IM].

[127] Abigail Crites et al. "Measuring the Epoch of Reionization using [CII] Intensity Mapping with TIME-Pilot." In: *American Astronomical Society Meeting Abstracts #229*. Vol. 229. American Astronomical Society Meeting Abstracts. Jan. 2017, 125.01, p. 125.01. URL: http://adsabs.harvard.edu/abs/2017AAS...22912501C.

[128] Joao Alves et al. "Planck 2015 results." In: *Astronomy & Astrophysics* 594, E1 (Sept. 2016), E1. DOI: 10.1051/0004-6361/201629543.

[129] Alan Kogut et al. "The Primordial Inflation Explorer (PIXIE)." In: *Space Telescopes and Instrumentation 2016: Optical, Infrared, and Millimeter Wave*. Vol. 9904. SPIE Conference Proceedings. July 2016, 99040W, 99040W. DOI: 10.1117/12.2231090.

[130] Paulo de Bernardis et al. "Exploring Cosmic Origins with CORE: The Instrument." In: *ArXiv e-prints* (May 2017). arXiv: 1705.02170 [astro-ph.IM].

[131] PRISM Collaboration. "PRISM (Polarized Radiation Imaging and Spectroscopy Mission): an extended white paper." In: *Journal of Cosmology and Astroparticle Physics* 2, 006 (Feb. 2014), p. 006. DOI: 10.1088/1475-7516/2014/02/006. arXiv: 1310.1554.

[132] Aritoki Suzuki et al. "The LiteBIRD Satellite Mission - Sub-Kelvin Instrument." In: *ArXiv e-prints* (Jan. 2018). arXiv: 1801.06987 [astro-ph.IM].

[133] Tomotake Matsumura et al. "LiteBIRD: mission overview and design tradeoffs." In: *Space Telescopes and Instrumentation 2014: Optical, Infrared, and Millimeter Wave*. Vol. 9143. SPIE Conference Proceedings. Aug. 2014, 91431F, 91431F. DOI: 10.1117/12.2055794.

[134] Jeffrey P. Filippini et al. "SPIDER: a balloon-borne CMB polarimeter for large angular scales." In: *Millimeter, Submillimeter, and Far-Infrared Detectors and Instrumentation for Astronomy V*. Ed. by Wayne S. Holland and Jonas Zmuidzinas. Vol. 7741. International Society for Optics and Photonics. SPIE, 2010, pp. 485–496. DOI: 10.1117/12.857720. URL: https://doi.org/10.1117/12.857720.

[135] The EBEX Collaboration et al. "The EBEX Balloon-borne Experiment — Detectors and Readout." In: *The Astrophysical Journal Supplement Series* 238.8 (2018). URL: https://iopscience.iop.org/article/10.3847/1538-4365/aae436.

[136] Laura M. Fissel et al. "BLAST-TNG: A Next Generation Balloon-borne Large Aperture Submillimeter Polarimeter." In: *American Astronomical Society Meeting Abstracts #229*. Vol. 229. American Astronomical Society Meeting Abstracts. Jan. 2017, 133.06, p. 133.06. URL: http://adsabs.harvard.edu/abs/2017AAS...22913306F.

[137] Charles L. Bennett et al. "Nine-Year Wilkinson Microwave Anisotropy Probe (WMAP) Observations: Final Maps and Results." In: *The Astrophysical Journal Supplement Series* 208.2 (Sept. 2013), p. 20. ISSN: 1538-4365. DOI: 10.1088/0067-0049/208/2/20. URL: http://dx.doi.org/10.1088/0067-0049/208/2/20.

[138] Planck Collaboration et al. "Planck 2015 results. XIII. Cosmological parameters." In: *Astronomy & Astrophysics* 594, A13 (Sept. 2016), A13. DOI: 10.1051/0004-6361/201525830. arXiv: 1502.01589 [astro-ph.CO].

[139] Lindsey Bleem et al. "An Overview of the SPTpol Experiment." In: *Journal of Low Temperature Physics* 167.5-6 (June 2012), pp. 859–864. DOI: 10.1007/s10909-012-0505-y.

[140] Neelima Sehgal et al. "The Atacama Cosmology Telescope: Cosmology from Galaxy Cluster Detected via the Sunyaev Zel'dovich Effect." In: *The Astrophysical Journal* 732.44 (2011). URL: https://iopscience.iop.org/article/10.1088/0004-637X/732/1/44.

[141] Peter A. R. Ade et al. "Improved Constraints on Cosmology and Foregrounds from BICEP2 and Keck Array Cosmic Microwave Background Data with Inclusion of 95 GHz Band." In: *Physical Review Letters* 116 (3 Jan. 2016), p. 031302. DOI: 10.1103/PhysRevLett.116.031302. URL: https://link.aps.org/doi/10.1103/PhysRevLett.116.031302.

[142] Jens Chluba et al. "Spectral Distortions of the CMB as a Probe of Inflation, Recombination, Structure Formation and Particle Physics." In: *Bulletin of the AAS* 51.3 (May 31, 2019). https://baas.aas.org/pub/2020n3i184. URL: https://baas.aas.org/pub/2020n3i184.

[143] Paolo Serra, Olivier Doré, and Guilaine Lagache. "Dissecting the High-z Interstellar Medium through Intensity Mapping Cross-correlations." In: *The Astrophysical Physics Journal* 833.2, 153 (Dec. 2016), p. 153. DOI: 10.3847/1538-4357/833/2/153. arXiv: 1608.00585 [astro-ph.GA].

[144] Alessandro Monfardini et al. *CONCERTO at APEX: installation and technical commissioning*. 2021. DOI: 10.48550/ARXIV.2106.14028. URL: https://arxiv.org/abs/2106.14028.

[145] Chang Feng et al. "Multi-component Decomposition of Cosmic Infrared Background Fluctuations." In: *The Astrophysical Journal* 875.2 (Apr. 2019), p. 86. ISSN: 1538-4357. DOI: 10.3847/1538-4357/ab0d8e. URL: http://dx.doi.org/10.3847/1538-4357/ab0d8e.

[146] Ritoban Basu Thakur et al. *Development of Superconducting On-chip Fourier Transform Spectrometers*. 2021. DOI: 10.48550/ARXIV.2111.06558. URL: https://arxiv.org/abs/2111.06558.

[147] Alexander V. Semenov et al. "Coherent Excited States in Superconductors due to a Microwave Field." In: *Physical Review Letters* 117 (4 July 2016), p. 047002. DOI: 10.1103/PhysRevLett.117.047002. URL: https://link.aps.org/doi/10.1103/PhysRevLett.117.047002.

[148] R. Basu Thakur et al. "Superconducting On-chip Fourier Transform Spectrometer." In: *Journal of Low Temperature Physics* 200.5-6 (June 2020), pp. 342–352. DOI: 10.1007/s10909-020-02490-7. URL: https://doi.org/10.1007%2Fs10909-020-02490-7.

[149] Rishi Khatri and Rashid Sunyaev. "Limits on the fluctuating part of y-type distortion monopole from Planck and SPT results." In: *Journal of Cosmology and Astroparticle Physics* 2015.08 (Aug. 2015). ISSN: 1475-7516. DOI: 10.1088/1475-7516/2015/08/013. URL: https://www.osti.gov/biblio/22525615.

[150] Ann E. Nelson and Jakub Scholtz. "Dark light, dark matter, and the misalignment mechanism." In: *Physical Review D* 84 (10 Nov. 2011), p. 103501. DOI: 10.1103/PhysRevD.84.103501. URL: https://link.aps.org/doi/10.1103/PhysRevD.84.103501.

[151] Bob Holdom. "Two U(1)'s and ϵ charge shifts." In: *Physics Letters B* 166.2 (1986), pp. 196–198. ISSN: 0370-2693. DOI: https://doi.org/10.1016/0370-2693(86)91377-8. URL: https://www.sciencedirect.com/science/article/pii/0370269386913778.

[152] Alessandra Filippi and Marzio De Napoli. "Searching in the dark: the hunt for the dark photon." In: *Reviews in Physics* 5 (2020), p. 100042. ISSN: 2405-4283. DOI: https://doi.org/10.1016/j.revip.2020.100042. URL: https://www.sciencedirect.com/science/article/pii/S2405428320300058.

[153] Paola Arias et al. "WISPy cold dark matter." In: *Journal of Cosmology and Astroparticle Physics* 2012.06 (June 2012), pp. 013–013. DOI: 10.1088/1475-7516/2012/06/013. URL: https://doi.org/10.1088%2F1475-7516%2F2012%2F06%2F013.

[154] Dieter Horns et al. "Searching for WISPy cold dark matter with a dish antenna." In: *Journal of Cosmology and Astroparticle Physics* 2013.04 (Apr. 2013), pp. 016–016. DOI: 10.1088/1475-7516/2013/04/016. URL: https://doi.org/10.1088/1475-7516/2013/04/016.

[155] Stephen J. Asztalos et al. "SQUID-Based Microwave Cavity Search for Dark-Matter Axions." In: *Physical Review Letters* 104.4 (Jan. 2010). DOI: 10.1103/physrevlett.104.041301. URL: https://doi.org/10.1103%2Fphysrevlett.104.041301.

[156] Joerg Jaeckel and Andreas Ringwald. "A cavity experiment to search for hidden sector photons." In: *Physics Letters B* 659.3 (Jan. 2008), pp. 509–514. DOI: 10.1016/j.physletb.2007.11.071. URL: https://doi.org/10.1016%2Fj.physletb.2007.11.071.

[157] Pierre Brun, Laurent Chevalier, and Christophe Flouzat. "Direct Searches for Hidden-Photon Dark Matter with the SHUKET Experiment." In: *Physical Review Letters* 122 (20 May 2019), p. 201801. DOI: 10.1103/PhysRevLett.122.201801. URL: https://link.aps.org/doi/10.1103/PhysRevLett.122.201801.

[158] Jun'ya Suzuki et al. "Experimental search for hidden photon CDM in the eV mass range with a dish antenna." In: *Journal of Cosmology and Astroparticle Physics* 2015.09 (Sept. 2015), pp. 042–042. DOI: 10.1088/1475-7516/2015/09/042. URL: https://doi.org/10.1088%2F1475-7516%2F2015%2F09%2F042.

[159] Nozomu Tomita et al. "Search for hidden-photon cold dark matter using a K-band cryogenic receiver." In: *Journal of Cosmology and Astroparticle Physics* 2020.9, 012 (Sept. 2020), p. 012. DOI: 10.1088/1475-7516/2020/09/012. arXiv: 2006.02828 [hep-ex].

[160] Arnaud Andrianavalomahefa et al. "Limits from the FUNK experiment on the mixing strength of hidden-photon dark matter in the visible and near-ultraviolet wavelength range." In: *Physical Review D* 102 (4 Aug. 2020), p. 042001. URL: https://link.aps.org/doi/10.1103/PhysRevD.102.042001.

[161] Alessandro Mirizzi, Javier Redondo, and Günter Sigl. "Microwave background constraints on mixing of photons with hidden photons." In: *Journal of Cosmology and Astroparticle Physics* 2009.03 (Mar. 2009), pp. 026–026. DOI: 10.1088/1475-7516/2009/03/026. URL: https://doi.org/10.1088%2F1475-7516%2F2009%2F03%2F026.

[162] Haipeng An, Maxim Pospelov, and Josef Pradler. "New stellar constraints on dark photons." In: *Physics Letters B* 725.4-5 (Oct. 2013), pp. 190–195. DOI: 10.1016/j.physletb.2013.07.008. URL: https://doi.org/10.1016%2Fj.physletb.2013.07.008.

[163] Saptarshi Chaudhuri. "Impedance matching to axion dark matter: considerations of the photon-electron interaction." In: *Journal of Cosmology and Astroparticle Physics* 2021.12 (Dec. 2021), p. 033. DOI: 10.1088/1475-7516/2021/12/033. URL: https://doi.org/10.1088%2F1475-7516%2F2021%2F12%2F033.

[164] *WR-159 Waveguide Standard Gain Horn Antenna*. Pasternack Enterprises. Mar. 2022. URL: https://www.pasternack.com/images/ProductPDF/PE9860-SF-10.pdf.

[165] Joshua W. Foster, Nicholas L. Rodd, and Benjamin R. Safdi. "Revealing the dark matter halo with axion direct detection." In: *Physical Review D* 97 (12 June 2018), p. 123006. DOI: 10.1103/PhysRevD.97.123006. URL: https://link.aps.org/doi/10.1103/PhysRevD.97.123006.

[166] Ciaran O'Hare. *cajohare/AxionLimits: AxionLimits*. Version v1.0. July 2020. DOI: 10.5281/zenodo.3932430. URL: https://cajohare.github.io/AxionLimits/.

[167] Kaidong Peng et al. "Floquet-Mode Traveling-Wave Parametric Amplifiers." In: *PRX Quantum* 3 (2 Apr. 2022), p. 020306. URL: https://link.aps.org/doi/10.1103/PRXQuantum.3.020306.